

國立交通大學

電子物理研究所

博士論文

表面吸附分子的轉動態及量子點的電子
性質之研究

Studies on the Rotational States of Adsorbed
Molecules, and the Electronic Properties of
Quantum Dots

研究生：廖英彥

指導教授：褚德三

中華民國九十五年六月

表面吸附分子的轉動態及量子點的電子性質之研究
Studies on the Rotational States of Adsorbed Molecules,
and the Electronic Properties of Quantum Dots

研究生：廖英彥

Student : Ying-Yen Liao

指導教授：褚德三

Advisor : Der-San Chuu

國立交通大學

電子物理研究所

博士論文

A Dissertation

Submitted to Institute of Electrophysics

College of Science

National Chiao Tung University

in Partial Fulfillment of the Requirements

for the Degree of

Doctor of Philosophy

in

Electrophysics

June 2006

Hsinchu, Taiwan, Republic of China

中華民國九十五年六月

表面吸附分子的轉動能態及量子點的電子性質 之研究

研究生: 廖英彥

指導教授: 褚德三

國立交通大學電子物理研究所

摘要

在本論文中，我們研究吸附雙原子分子的轉動能態和量子點的物理性質。在第一部份中，我們考慮高強度雷射場照射在受到角錐位能井局限的吸附極性分子上，藉由改變位能井的禁制角度，我們觀察分子從自由轉動過渡到禁制轉動的行為。同時，我們也進一步探討耦合自由與吸附分子的轉動能態，發現其分子偏向與單一吸附分子的偏向有相當不同的差異性，原因是來自於分子間偶極作用的影響。此外，我們也計算了 von Neumann 熵來定義耦合分子系統的糾纏程度，結果發現糾纏會受到分子間距離、雷射脈衝強度與數目以及局限效應的影響。

在第二部份中，我們探討量子點系統是自旋弛豫與電子傳輸的現象。當量子點被製備在半導體平板內，我們發現由於聲子與自旋軌道交互作用的影響，自旋弛豫會顯現出類似共振腔的行為；另外，為了研究聲子在電子傳輸的效應，我們進一步考慮雙量子點元件處在一個單一聲子的環境中，結果顯示傳輸行為強烈地受到庫倫或是聲子場的影響。最後，我們也研究雙量子點在外加場作用下的電子傳輸現象，由於電子能態與外加場交互作用，我們發現電流大小會受到提升或是壓抑。

Studies on the Rotational States of Adsorbed Molecules, and the Electronic Properties of Quantum Dots

Student : Ying-Yen Liao

Advisor : Der-San Chuu

Institute of Electrophysics
National Chiao Tung University

ABSTRACT

In this dissertation, we study the rotational states of adsorbed diatomic molecules and some physical properties of quantum dots. In part I, an adsorbed dipole molecule confined by a conical well is subject to strong laser fields. The crossover from field-free to hindered rotation motion is observed by varying the hindering angle. Moreover, the rotational states of coupled free and adsorbed molecules with dipolar interaction are further studied. It is shown that the orientation is significantly different from that of an isolated one due to the dipole-dipole interaction. In addition, the von Neumann entropy is calculated to characterize the degree of entanglement. It is also found that the entanglement can be influenced by the inter-molecule distance, the strength and number of laser pulses, and the confinement effect.

In part II, we investigate the spin relaxation and electron transport in quantum dot systems. When a quantum dot is embedded in a semiconductor slab, the spin relaxation rate shows peculiar behaviors due to the confined phonons. Second, to observe the phonon effect on the transport, we have also considered a double-dot device embedded in a single phonon environment. It is shown that the transport behavior is deeply influenced by the Coulomb or phonon field. Finally, the transport of a double-dot device irradiated by an external field is considered. The enhanced or suppressed current is found due to the interplay between the energy states and external field.

誌 謝

感謝指導教授褚德三老師的教誨與悉心指導，使本論文得以順利完成，在此表達我最誠摯的謝意。

在這過程中，也要感謝實驗室學長、同學及學弟的討論與建議，進而使得論文研究更加完備。

此外，感謝我的朋友在這段攻讀博士期間給我許多鼓勵與協助，同時要感謝國立交通大學提供良好的學習環境。

最後，謹以此論文獻給我的父母與家人。你們的支持與包容是我完成博士學位最大的精神支柱。



CONTENTS

LIST OF FIGURES	xiv
1 INTRODUCTION	1
2 INTRODUCTION TO PART I	3
3 AN ADSORBED DIPOLE MOLECULE IN LASER FIELDS	8
3.1 Model of an adsorbed molecule	9
3.2 Connection between theory and experiment	12
3.3 An adsorbed molecule in a strong laser field	14
3.4 Results and discussion	16
4 COUPLED FREE MOLECULES IN LASER FIELDS	25
4.1 Model of two coupled free molecules in a strong laser pulse	26
4.2 Entanglement of two coupled free molecules	28
4.3 Results and discussion	29
5 COUPLED ADSORBED MOLECULES IN LASER FIELDS	46
5.1 Single adsorbed molecule in a strong laser pulse	47
5.2 Two coupled adsorbed molecules in a strong laser pulse	51
6 SUMMARY AND FUTURE WORK	61

7	INTRODUCTION TO PART II	64
8	SPIN RELAXATION IN A GAAS QUANTUM DOT EMBEDDED IN- SIDE A SUSPENDED PHONON CAVITY	69
8.1	Model	71
8.1.1	Single particle in a quantum dot	71
8.1.2	Confined phonon in a semiconductor slab	73
8.1.3	Electron-phonon coupling and scattering rate	75
8.2	Results and discussion	76
9	ELECTRON TRANSPORT THROUGH A DOUBLED QUANTUM DOT SYSTEM WITH SINGLE PHONON MODE	86
9.1	Model	88
9.2	Results and discussion	93
10	ELECTRON TRANSPORT THROUGH A DRIVEN THREE-LEVEL DOU- BLE DOT	101
10.1	Model	102
10.2	Results and discussion	106
11	SUMMARY AND FUTURE WORK	116



LIST OF FIGURES

2.1 Schematic view of molecular adsorption systems. The adsorbed diatomic molecules at the left and the center show different adsorption configurations, i.e. the vertical and horizontal, respectively. From Ref. [2].	7
3.1 Schematic view of the hindered rotor.	20
3.2 Quadrupole moments for the desorption of CO from Cr ₂ O ₃ (0001) as function of quantum number J . Filled circles: experimental data points.	21
3.3 The populations of the states $(l, m = 0)$ for different hindered angles: (a) $\alpha = 60^\circ$, (b) $\alpha = 120^\circ$, (c) $\alpha = 180^\circ$. The insets show the corresponding alignments (solid lines) and the first two main contributions of the factors $\sum_{l \neq l'} \langle \psi_{l',m'} \cos^2 \theta \psi_{l,m} \rangle$ (dotted lines).	22
3.4 The orientations $\langle \cos \theta \rangle$ (solid lines) of a hindered molecule confined by infinite conical-well for different hindered angles: (a) $\alpha = 60^\circ$, (b) $\alpha = 120^\circ$, (c) $\alpha = 175^\circ$. The dashed and dotted lines in (c) correspond to different potential barrier height, i.e. $V_0 = \infty$ and 100, respectively.	23

3.5	The mean orientation $\langle \cos \theta \rangle_{\text{mean}}$ and alignment $\langle \cos^2 \theta \rangle_{\text{mean}}$ in infinite conical-well. The insets show the populations $ c_{l,m} ^2$ (filled bar) and factors $\langle \psi_{l,m} \cos^2 \theta \psi_{l,m} \rangle$ (sparse bar). Insets (a) and (b) correspond to $\alpha = 110^\circ$ and $\alpha = 170^\circ$, respectively.	24
4.1	Upper panels of Fig. 4.1(a) and (b) show the orientations of the two molecules at different distances. Lower panels: The populations of the states $(l_1, m_1; l_2, m_2) = (1, 0; 0, 0)$ (solid lines), $(2, 0; 1, 0)$ (dotted lines), $(1, 0; 1, 0)$ (dashed lines). The insets in (a) and (b) represent the population of state $(3, 0; 1, 0)$	37
4.2	The orientations of the first and second molecules under periodic laser pulses with the periods $T =$ (a) $1\hbar/B$, (b) $\pi\hbar/B$ ps. The upper and lower panels of (a) and (b) correspond to the distances $R = 3 \times 10^{-8}$ and 2×10^{-8} m, respectively.	38
4.3	Time evolution of the entropy after applying single laser pulse for (a) $R = 5 \times 10^{-8}$ m and (b) $R = 1.5 \times 10^{-8}$ m.	39
4.4	Time evolution of the entropy for inter-molecule separation $R = 1.5 \times 10^{-8}$ m. The degree of entanglement can be enhanced if one increases the field strength.	40

4.5	Time evolution of the entropy after applying single laser pulse for different ratios in magnitudes of the positive and negative peak value of the laser pulse. The graphs show the irregular (periodic) behavior for ratio 9 : 1 (1 : 1). The inset : the first ten contributive eigenvalues λ_p at short time ($t = 50$ ps) and long time ($t = 800$ ps).	41
4.6	Populations of the states $(l_1, m_1; l_2, m_2)$ for different ratios. Upper panel : $(1, 0; 0, 0)$ (dashed line), $(1, 0; 1, 0)$ (solid line), $(2, 0; 1, 0)$ (dotted line). Lower panel : $(0, 0; 0, 0)$ (dashed line), $(1, 0; 1, 0)$ (solid line), $(1, 1; 1, 1)$ (dotted line). The inset in the lower panel is the enlarged figure showing the states $(1, 0; 1, 0)$ (solid line), $(1, 1; 1, 1)$ (dotted line), respectively.	42
4.7	Time evolution of the entropy for different separation and dipole moment under single pulse (ratio 9 : 1). The dotted curve shows the case of $R = 1.5 \times 10^{-8}$ m and $\mu = 9.2 D$. The dashed and solid curves correspond to (a) 0.8 R and 1.2 R , or (b) 1.2 μ and 0.8 μ , respectively.	43
4.8	Time evolution of the entropy for fixed ratio 5 : 1 under single pulse (dashed line) and double pulses (solid line). Time separation (t_{app}) between two pulses is set to be 5 times the center of the laser peak. The inset : Dependence of the time-averaged entropy on the pulse shape for inter-molecule separation $R = 1.5 \times 10^{-8}$ m.	44

4.9	The time with respect to different Planck constant \hbar' for fixed field strength $E_0 = 3 \times 10^7$ V/m and inter-molecule separation $R = 1.5 \times 10^{-8}$ m. The time is defined as the first time in entropy that exceeds the time-averaged value (the arrow in the inset). The inset : the time-averaged value (dotted line), and time evolution of the entropy for $\hbar' = 0.01\hbar$ (solid line).	45
5.1	(a) Schematic view of single hindered rotor adsorbed on the surface. (b) The corresponding infinite-conical-well model.	56
5.2	The orientation $\langle \cos \theta \rangle$ as a function of time for different hindering angle α and pulse duration σ' . The insets show the corresponding populations of the states $(l, m = 0)$ for (a) $\alpha = 60^\circ$ and (b) $\alpha = 120^\circ$ respectively. The corresponding laser fields are shown in the upper inset.	57
5.3	The mean orientation $\langle \cos \theta \rangle_{\text{mean}}$ as a function of hindering angle for fixed pulse duration ($\sigma' = \sigma$) and different conical-well potentials $V_0 = 10, 30, 100$. The inset shows the mean orientation $\langle \cos \theta \rangle_{\text{mean}}$ in the case of $V_0 = 10$ and ∞ by applying a pulse of $\sigma' = 5\sigma$. The potential V_0 is in units of the rotational constant B	58

5.4	The entropy (a) and orientations $\langle \cos \theta_1 \rangle$ ($\langle \cos \theta_2 \rangle$) (b) in infinite conical-well for fixed angle $\alpha = 120^\circ$ and inter-distance $R = 1.5 \times 10^{-8}$ m. The inset shows the populations $(c_{l_1, m_1; l_2, m_2}(t) ^2)$ irregularly oscillate with time, corresponding to the quantum number $(l_1, m_1; l_2, m_2) = (1, 0; 0, 0)$ (black solid curve), $(1, 1; 0, 0)$ (red dashed curve), and $(1, 0; 1, 0)$ (green dotted curve) respectively. Although we only focus on several excited states here, the populations of most states similarly remain irregular behavior.	59
5.5	The time-averaged entropy as a function of the hindered angle in infinite conical-well. The insets show the orientations of two molecules for hindered angles $\alpha = 30^\circ$ and $\alpha = 150^\circ$ respectively. The inter-molecule separation is $R = 1.5 \times 10^{-8}$ m.	60
7.1	Schematic views of a lateral (a) and vertical (b) quantum dots. From Ref. [55].	68
8.1	(a) Schematic view of single quantum dot embedded in the semiconductor slab with a width of a . (b) The side view shows a quantum dot is located at $z = 0$	80
8.2	Energy spectrum for GaAs quantum dot versus the applied magnetic field for the lateral length $l_0 = 30$ nm. The spin-orbit couplings λ_R and λ_D are set equal to 5×10^{-13} and 16×10^{-12} eV m, respectively.	81

8.3	<p>(a) Spin relaxation rate as a function of magnetic field for the lateral length $l_0 = 30$ nm, the width $a = 130$ nm, and temperature $T=100$ mK. The spin-orbit couplings λ_R and λ_D are set equal to 5×10^{-13} and 16×10^{-12} eV m, respectively. The insets further show the enlarged regions of arrow 1 (upper inset) and arrow 2 (lower inset).</p> <p>(b) Three phonon group velocities vs the magnetic field. (c) The values q_{\parallel} and q_t vs the magnetic field.</p>	82
8.4	<p>Spin relaxation rate for the lateral length $l_0 = 60$ nm, width $a = 130$ nm, and temperature $T=100$ mK. The spin-orbit couplings λ_R and λ_D are set equal to 5×10^{-13} and 16×10^{-12} eV m, respectively. Two enhanced and suppressed rates (arrow) occur. The inset shows the energy spacing ΔE vs the magnetic field B for different lateral lengths: $l_0 = 30$ nm (dashed line) and $l_0 = 60$ nm (solid line). Two horizontal lines in the inset indicate the corresponding energies for the van Hove singularity (dotted line) and the suppression of the rate (dashed-dotted line).</p>	83
8.5	<p>Spin relaxation rates for different temperatures: $T=10$ mK (black line) and $T=1$ K (red line). The inset shows the rates in the low field regime.</p>	84

8.6	Dependence of the specific energy spacings ΔE for the enhanced (black mark) and suppressed (red mark) rates on the width a . The lateral length of the quantum dot is 30 nm. The Rashba constant is $\lambda_R = 5 \times 10^{-12}$ eVm and the Dresselhaus constant is $\lambda_D = 16 \times 10^{-12}$ eVm.	85
9.1	Schematic view of double quantum dot embedded in a single phonon environment. Two dots are connected with the leads respectively. The separation between two quantum dots is d and the interdot tunneling is forbidden with split gate technology.	97
9.2	Short separation regime ($\Delta \approx U$): Linear conductance of Dot 1 (plotted in units of e^2/h) as a function of Fermi energy. The solid (dotted) curve shows the conductance if an (no) excess electron stays in the Dot 2, corresponding to the enhancement of resonant level (inset). The strength U is set to $5 \omega_0$	98
9.3	Long separation regime ($\Delta \approx -2 \lambda_1 ^2 / \omega_0$): Linear conductance of dot 1 (plotted in units of e^2/h) as a function of Fermi energy. The solid (dotted) curve shows the conductance if an (no) excess electron stays in the Dot 2, corresponding to the reduction of resonant level (inset). The coupling λ_1 is set to $0.5 \omega_0$	99

9.4	Fermi energy at the resonant peak as a function of phase factor for long separation regime. The solid (dotted) curve shows the conductance if an (no) excess electron stays in the Dot 2.	100
10.1	Schematic view of a three-level system which consists of the ground state in the left dot, the ground state and first excited state in the right dot in a double quantum dot device. An external field irradiates on the device and leads to the transition between two states in the right dot.	110
10.2	Current as a function of energy difference $\Delta\varepsilon$ between two ground states for different Rabi frequencies. The inset shows the currents I_R (dashed curve) and I_E (dotted curve) for $\gamma = 5\Gamma$	111
10.3	Dependence of the current on Rabi frequency for the tunneling coupling $T_c = \Gamma$, corresponding to the populations n_R and n_E (upper inset). The red dotted line marks the maximum current for two-level system. The lower inset shows the currents for different tunneling couplings. The conditions are fixed to be $\Delta\varepsilon = 0$ and $\Delta\omega = 0$	112

10.4 Current as a function of energy difference $\Delta\varepsilon$ for fixed non-resonant field ($\Delta\omega = 5 \Gamma$) and Rabi frequency ($\gamma = 5 \Gamma$). The total current I (black curve) is composed of two channels in the right dot: the electron tunneling out through the ground level I_R (red dashed curve) and first excited level I_E (blue dotted curve). 113

10.5 Current as a function of frequency difference $\Delta\omega (= \omega - \Delta R)$ for different Rabi frequencies and for fixed $\Delta\varepsilon = 0$. The inset shows the populations n_R and n_E for Rabi frequencies $\gamma = 2\Gamma$ and $\gamma = 10\Gamma$. 114

10.6 Current as a function of frequency difference $\Delta\omega (= \omega - \Delta R)$ for different Rabi frequencies and for fixed $\Delta\varepsilon = 5\Gamma$. The inset shows the populations n_R and n_E for Rabi frequencies $\gamma = 2\Gamma$ and $\gamma = 10\Gamma$ 115



CHAPTER 1

INTRODUCTION

Nanoscience and nanotechnology have attracted a great deal of attention ranging from atoms, molecules to quantum dots. The purpose lies in the prospect of understanding matter and its transformations at the most rudimental level. Further, possible novel devices are hopefully developed to control the quantum states in the ultimate limit. It is known that single atom and molecule are the building blocks of matter. An important feature is that some intrinsic phenomena cannot simply be probed from an ensemble of atoms or molecules. In addition, the effects of the environments are deeply affect the physical properties. For example, consider one molecule adsorbed on the solid surface, the energy levels are different from those of free rotors. The physical properties are sensitive to the adsorption site local symmetry, adsorbed molecule configuration, and local potential. With the advance of laser and scanning probe technologies, it further becomes possible to manipulate and control it at the spatial limit.

In analogy to atomic properties, a quantum dot is a fabricated nanostructure in which electrons have been confined in all three dimensions, typically with sizes ranging from nanometers to a few microns. Quantum dots exhibit discrete, size-dependent electric and optical properties. Due to the discrete nature of their

energy levels, quantum dots are therefore regarded as artificial atoms. Moreover, the electrons confined in the two coupled quantum dots can form an artificial molecule. The coupling between different dots can be tuned by changing the gate voltages or interdot distances. Unlike the natural atoms, however, the numbers of excess electron embedded in these quantum dots are tunable. Besides, the artificial atom can be coupled to the electron reservoirs. One can probe the electronic states and then measure the transport properties of a quantum dot. Of particular importance is the Coulomb blockade effect leading to single-electron transport. This is because the Coulomb repulsion between the electrons on the dot results in a considerable energy cost for adding an extra electron charge. When the charging energy of a small quantum dot is needed, electron in the leads cannot transfer into the dot until increasing the voltage provides this energy.

Since the interplay between molecules, environments, and external influences reveals the fruitful physics, part I of this dissertation is devoted to the studies on the rotational states of adsorbed diatomic molecules in laser fields. We will discuss the related properties of single adsorbed molecule and then extend our study to multi-rotor system. In part II, we will focus on the study of quantum dot systems. Since the carrier-phonon interaction is one of the inherent effects in solid-state structures, we will discuss the lattice relaxation process in a single quantum dot. In addition, the transport properties of the coupled dot systems are further considered in different cases.

CHAPTER 2

INTRODUCTION TO PART I

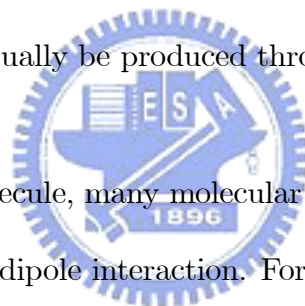
Since Langmuir [1] first conceived that localized adsorption occurs on surfaces, studies of the adsorption of atoms and molecules attract much attention. The historic studies and concept of localized chemical bonding on surface sites firmly set one principal milestone for surface science. Among massive researches, investigation on the rotational properties of adsorbed molecules is a central subject. Figure 2.1 illustrates schematically a picture of crystal surface in which hindrance and/or modulation of the molecular motion may occur [2]. The adsorbed molecules show different types of equilibrium adsorption configurations. As can be seen from Fig. 2.1, the diatomic molecules may be adsorbed on the surface vertically or horizontally. Due to the molecule-surface interaction, the substrate can influence the rotation of an adsorbed molecule (rotor).

The molecule-surface interaction is generally a complex problem which involves the molecule-surface separation, the lateral motion along the surface, the molecular rotation, the molecular vibration, and the electronic excitation. Due to the differences in energy scale, one can separate the rotational degree of freedom from others. Although it is greatly simplified, analytical expressions for the realistic surface hindering potentials are still unavailable. In order to clearly describe

the interaction between the adsorbed molecule and the surface, various models were proposed to simulate the hindered rotational motions. One example is the infinite conical-well model proposed by Gadzuk et al. [2, 3]. The important feature of this model is that the adsorbed molecule is only allowed to rotate within the well region. This model successfully provided a good insight into the rotations of hindering molecules. However, its weakness is that, compared to the experimental data, it is difficult to deduce more information about the molecule-surface interaction strength from an infinite conical-well model. Therefore, a more realistic finite hindering potential was considered by Shih et al. [4, 5]. It was found that the rotational energy levels exhibit oscillatory behavior by varying the hindering angles. This behavior is different from that of an infinite conical-well model. Besides, the Stark shifts of the rotational states were also investigated [6, 7]. The theoretical results derived from their model are in good agreements with the experiments [8, 9, 10, 11].

With the rapid developments of laser technologies, mid toward far IR laser field, which have potential applications ranging from nanoscale design, surface processing, stereodynamics to chemical reactivity, are achievable to manipulate the motions of molecules [12], i.e., molecular alignments and orientations. A pioneering work studied by Friedrich and Herschbach [13] is that the molecular alignment is responsible for the anisotropic polarizability induced by the non-resonant laser pulses. When the duration of laser pulse is longer than the rotational period,

the pendular states can be created adiabatically, and the molecular axis is aligned parallel to the direction of field polarization [14, 15, 16]. As the laser pulse is switched off, the molecule will go back to its initial condition and no longer be observed again. If the duration of laser pulse is shorter than the rotational period, the alignment occurs periodically in time (the non-adiabatic regime) [17, 18]. For molecular orientations, Henriksen [19] derived an analytical expression for the wavepacket based on the Magnus expansion. According to the model, an ultra-short laser pulse is able to generate a field-free orientation [20], i.e. it can impart a kick, like impulsive excitation, to the molecule [21]. The dipole molecule will tend to orient in the direction of laser polarization. To achieve an efficient orientation, a tailored laser pulse can actually be produced through optimal control [22, 23].



In addition to single molecule, many molecular systems show peculiar behavior in the presence of dipole-dipole interaction. For example, Rogalsky et al. [24] presented neutron scattering linewidths of certain Hofmann clathrates. A line broadening mechanism based on rotor-rotor coupling was proposed for the explanation of the widths [25]. Furthermore, a novel physical realization of a quantum computer via the electric dipole-dipole interaction was proposed by DeMille [26]. Shima and Nakayama [27] calculated the energy spectra and dielectric susceptibilities in coupled-rotor systems. Nonadiabatic orientations of coupled quantum rotors with dipolar interaction were also studied [28]. Recently, interacting molecules mounted on the surfaces were also studied with the help of nanotechnology

[29, 30, 31].

In this part we investigate the rotational motions of adsorbed dipole molecules under strong laser fields. The surface potential is modeled as a conical well for hindered rotors, and a dipole-field interaction is then included into the system. The crossover from field-free to hindered rotation motions is studied by varying some related parameters. Moreover, we further consider the dipole-dipole interaction in double-molecule system. The orientations and entanglement of coupled (free and adsorbed) molecules are also discussed.

This part is organized as follows. In chapter 3, we study the rotational states of a polar molecule vertically adsorbed on the surface and subjected to a strong laser field. The molecular alignments and orientations are studied by varying the degree of hindered potential well. We further investigate the orientations of two coupled, free polar molecules irradiated by strong laser pulses in chapter 4. The degree of entanglement, characterized by the von Neumann entropy, is also discussed. In chapter 5, we study the orientations of coupled adsorbed polar molecules in a strong laser field. Entanglement induced by the dipolar interaction is also calculated and analyzed for different hindering angles of conical wells. Finally, we conclude our results and present future works in chapter 6.

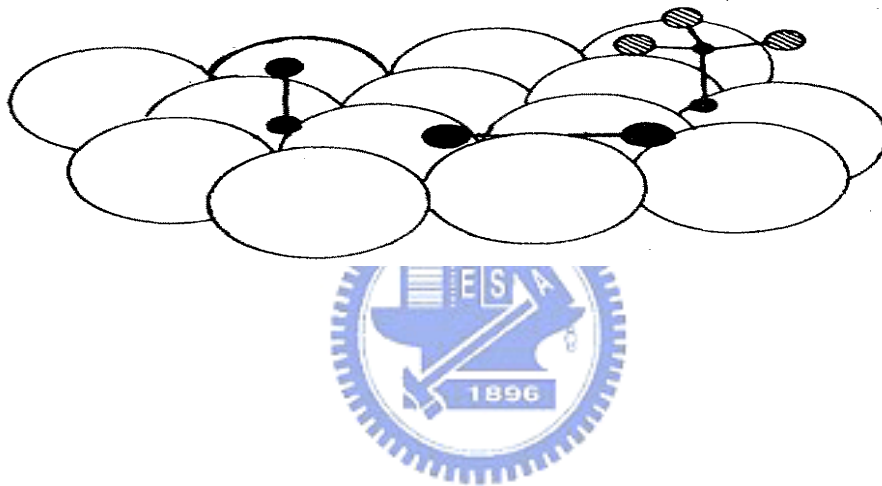


Figure 2.1: Schematic view of molecular adsorption systems. The adsorbed diatomic molecules at the left and the center show different adsorption configurations, i.e. the vertical and horizontal, respectively. From Ref. [2].

CHAPTER 3

AN ADSORBED DIPOLE MOLECULE IN LASER FIELDS

With the developments laser technology, alignments and orientations of molecules are important in the investigations of stereodynamics, surface catalysis, molecular focusing, and nanoscale design [12]. The alignment scheme has been demonstrated both in adiabatic and nonadiabatic regimes. A strong laser pulse can adiabatically create pendular states, and the molecular axis is aligned in parallel to the direction of field polarization. The molecule goes back to its initial condition after the laser pulse is switched off, and the alignment can no longer be observed again [13, 16]. To achieve adiabatic alignment, the duration of laser pulse must be longer than the rotational period. However, an ultrashort laser pulse with several cycles is also observed to induce a field-free alignment providing the duration of laser pulse is smaller than the rotational period. In this limit, the alignment occurs periodically in time as long as the coherence of the process is preserved [17, 18]. On the other hand, a femtosecond laser pulse is found to be able to generate field-free orientations [20]. The dipole molecule, kicked by an impulsive pulse, will tend to orient in the direction of laser polarization.

Recently, the rotational motion of a molecule interacting with a solid surface has attracted increasing interest. It is known that molecules can be desorbed by applying UV laser beam along the surface direction, and the quadrupole is a measure of the rotational alignment [9, 10, 11]. To understand molecular-surface interaction, Gadzuk and his co-workers [2, 3] proposed an infinite-conical-well model, in which the adsorbed molecule is only allowed to rotate within the well region. Shih et al. further proposed a finite-conical-well model to generalize the study of a finite hindrance [4, 5]. Their results showed that the rotational states of an adsorbed dipole molecule in an external electric field exhibit interesting behaviors, and theoretical calculation of the quadrupole moment based on finite-conical-well model is in agreement with the experimental data [7].

In order to explore the dynamical behavior of a molecule adsorbed on the surface, we investigate the rotational motions of an adsorbed diatomic molecule under an ultrashort laser pulse in this chapter. Different well-dependent signatures between the alignments and orientations of the hindered molecule are discussed. Besides, the crossover from field-free to hindered rotation is also studied.

3.1 Model of an adsorbed molecule

A diatomic molecule with a dipole moment μ is vertically adsorbed on the surface. The Hamiltonian of such system is

$$H = \frac{\hbar^2}{2I} L^2 + V_{hin}(\theta, \phi), \quad (3.1)$$

where I is the molecular moment of inertia with respect to its center of rotation, L^2 is the angular momentum operator, and $V_{hin}(\theta, \phi)$ is the surface potential energy to which the molecule is subjected. For convenience, we express the energy in the unit of the molecular rotational constant $B = \hbar^2/2I$. Straightforwardly, the Schrödinger equation for the molecular rotation in spherical coordinates can be expressed as

$$\left[\frac{1}{\sin \theta} \frac{\partial}{\partial \theta} (\sin \theta \frac{\partial}{\partial \theta}) + \frac{1}{\sin^2 \theta} \frac{\partial^2}{\partial \phi^2} + \epsilon_{l,m} - V_{hin}(\theta, \phi) \right] \psi_{l,m}(\theta, \phi) = 0, \quad (3.2)$$

where $\epsilon_{l,m}$ is the rotational energy and $\psi_{l,m}$ is the corresponding eigenfunction. In general, the dependence of the potential energy $V_{hin}(\theta, \phi)$ on θ and ϕ is complicated. Since calculations indicate that the dependence on ϕ is weaker than that on θ , we reasonably assume that $V(\theta, \phi)$ is independent of ϕ [32, 33, 34]. To simulate the potential energy, the finite conical-well model [4, 5] is proposed (Fig. 3.1)

$$V_{hin}(\theta) = \begin{cases} 0, & 0 \leq \theta \leq \alpha, \\ V_0, & \alpha < \theta \leq \pi, \end{cases}, \quad (3.3)$$

where V_0 represents the barrier height. The eigenfunctions for this system can be analytically written as

$$\psi_{l,m}(\theta, \phi) = \Theta_{l,m}(\cos \theta) \frac{\exp(im\phi)}{\sqrt{2\pi}}, \quad (3.4)$$

where

$$\Theta_{l,m}(\xi) = \begin{cases} C_{I,l,m} \mathcal{P}_{(+1)}(\nu_{l,m}, m, \xi), & \cos \alpha < \xi \leq 1, \\ C_{II,l,m} \mathcal{P}_{(-1)}(\nu'_{l,m}, m, \xi), & -1 \leq \xi < \cos \alpha, \end{cases} \quad (3.5)$$

with $\xi = \cos \theta$ and the quantum numbers (l, m) . Here $C_{I,l,m}$ and $C_{II,l,m}$ are the normalizational constants. The functions $\mathcal{P}_{(\pm 1)}$ in above equations are defined as

$$\mathcal{P}_{(\pm 1)}(\nu_{l,m}, m, \xi) = (1 - \xi^2)^{|m|/2} F\left(|m| - \nu_{l,m}, 1 + |m| + \nu_{l,m}, 1 + |m|; \frac{1 \mp \xi}{2}\right), \quad (3.6)$$

where $F(a, b, c; z)$ is the hypergeometric function [35]. In above equations, the molecular rotational energy is expressed as

$$\epsilon_{l,m} = \nu_{l,m}(\nu_{l,m} + 1), \quad (3.7)$$

and $\nu'_{l,m}$ is defined as

$$\nu'_{l,m}(\nu'_{l,m} + 1) = \nu_{l,m}(\nu_{l,m} + 1) - V_0. \quad (3.8)$$

In order to determine $\nu_{l,m}$, one has to match the boundary conditions at $\xi = \cos \alpha$.

As the potential well is infinite ($V_0 \rightarrow \infty$), Eq. (3.5) reduces to

$$\Theta_{l,m}(\xi) = \begin{cases} C_{I,l,m} \mathcal{P}_{(+1)}(\nu_{l,m}, m, \xi), & \cos \alpha < \xi \leq 1, \\ 0, & -1 \leq \xi < \cos \alpha. \end{cases} \quad (3.9)$$

The corresponding rotational energy $\epsilon_{l,m}$ is $\nu_{l,m}(\nu_{l,m} + 1)$ determined by the boundary condition,

$$\mathcal{P}_{(+1)}(\nu_{l,m}, m, \xi = \cos \alpha) = 0. \quad (3.10)$$

Note that the Eq. (3.9) and (3.10) are exactly the same as the results obtained in Refs. [2, 3].

3.2 Connection between theory and experiment


Certainly, using a simplified analytical potential is not state-of-the-art. Molecule surface interaction potentials can nowadays be mapped out in great detail by ab initio electronic structure methods. However, as can be seen in the works [4, 5, 6, 7], the simplified model shows interesting results. Furthermore, qualitative concepts and mechanisms can also be derived from the investigations. For example, we can justify the model by the performance of calculations on the rotational alignment of the desorbing molecules.

When a molecule desorbs from a solid surface, [9, 10, 11, 36, 37, 38, 39] the quadrupole moment $A_0^2(J)$ is a measure of the rotational alignment and is defined as $A_0^2(J) = \langle J | (3J_z^2 - J^2) / J^2 | J \rangle$ [40]. In the classical limit, the value of $A_0^2(J)$ represents the ensemble average of $(3 \cos^2 \chi - 1)$ where χ is the angle between the angular momentum vector J of the molecule and the surface normal. The value of $A_0^2(J)$ ranges from +2 to -1, where positive values present helicopter-like motion (J vector prefers to parallel to the surface normal), negative values correspond cartwheel-like motion (J vector prefers to perpendicular to the surface normal).

To compare with the possible observed data, we calculate the quadrupole moment $A_0^2(J)$ by the results obtained in our model of finite conical well. According to the sudden unhindrance approximation, the quadrupole moment of the alignment distribution can be evaluated by the following equation:

$$A_0^2(J) = \frac{\sum_{m,L,m'} \exp(-\epsilon_{L,m'}/k_B T) \left\langle Y_{J,m} \left| \frac{3J_z^2 - J^2}{J^2} \right| Y_{J,m} \right\rangle |\langle Y_{J,m} | \psi_{L,m'} \rangle|^2}{\sum_{m,L,m'} \exp(-\epsilon_{L,m'}/k_B T) |\langle Y_{J,m} | \psi_{L,m'} \rangle|^2}. \quad (3.11)$$

Figure 3.2 shows our calculated results compared with the experimental results of the rotational alignment in the photodesorption of CO from Cr₂O₃(0001) [9, 10, 11]. The hindrance parameters we used here are $V_0 = 2000$ and $\alpha = 120^\circ$. It was observed experimentally the quadrupole moment of desorbing CO changes its sign from positive to negative with increasing rotational quantum number J . Theoretically we could reproduce a positive quadrupole moment for small quantum number J and thus corresponds to the helicopter-like desorbing, while a negative quadrupole moment of desorbing CO can be obtained and thus corresponds to the cartwheel-like desorbing for larger quantum number J . This result agrees qualitatively with the experimental observations as can be noted from Fig. 3.2.



To see more profoundly that our calculated results can yield positive values of quadrupole momentum for small angular momentum and negative values for large J states, we examine the expectation value $\langle Y_{J,m} | (3J_z^2 - J^2) / J^2 | Y_{J,m} \rangle$ in Eq. (3.11). For a specific quantum number J , this expectation value is positive for high $|m|$ values and is negative for low $|m|$ values. In the summation of Eq. (3.11), only the low-lying hindered-rotational states $\psi_{L,m'}$ dominate due to the thermal factor. We calculated the overlapping factors $|\langle Y_{J,m} | \psi_{L,m'} \rangle|^2$ between the free-rotational states $Y_{J,m}$ and the low-lying hindered-rotational states $\psi_{L,m'}$. Our results showed that, when J is small, the calculated values of $|\langle Y_{J,m} | \psi_{L,m'} \rangle|^2$ for a specific L is larger for $\psi_{L,m'}$ states with larger $|m|$ which correspond to more horizontally-distributed wavefunctions. This makes the hindered molecule

prefer to the helicopter-like desorption and yield a positive quadrupole moment. On the contrary, when J is larger, the low-lying $\psi_{L,m'}$ states correspond smaller $|m|$ and then negative expectation values $\langle Y_{J,m} | (3J_z^2 - J^2) / J^2 | Y_{J,m} \rangle$. Our results also showed that, when J is larger, the calculated values of $|\langle Y_{J,m} | \psi_{L,m'} \rangle|^2$ for a specific L is larger for $\psi_{L,m'}$ states with smaller $|m|$ which correspond to more vertically-distributed wavefunctions. This makes the hindered molecule prefer to the cartwheel-like desorption in larger J states and yield a negative quadrupole moment.

3.3 An adsorbed molecule in a strong laser field

Consider now a laser pulse polarizing in z-direction interacts with the hindered molecule. The model Hamiltonian can be written as

$$H = BL^2 + V_{hin}(\theta) + H_I, \quad (3.12)$$

where L^2 and B are the angular momentum operator and rotational constant. For the vertical absorbed configuration, the surface potential which was proposed by Gadzuk [2, 3] can be written as

$$V_{hin}(\theta) = \begin{cases} 0, & 0 \leq \theta \leq \alpha \\ \infty, & \alpha < \theta \leq \pi \end{cases}, \quad (3.13)$$

where α is the hindered angle of the conical well. In Eq. (3.12), H_I describes the interaction between the dipole moment (permanent and induced) and laser field:

$$H_I = -\vec{\mu} \cdot \vec{\varepsilon}(t), \quad (3.14)$$

where $\vec{\mu}$ is the dipole moment and $\vec{\varepsilon}$ is the electric field vector of the linearly polarized laser. In the presence of an electric field, the dipole moment can be expressed as [41, 42]

$$\vec{\mu} = \vec{\mu}_0 + \frac{1}{2}\alpha\vec{\varepsilon} + \frac{1}{6}\beta\vec{\varepsilon}^2 + \frac{1}{24}\gamma\vec{\varepsilon}^3 + \dots, \quad (3.15)$$

where μ_0 is the permanent dipole moment, α is the polarizability tensor, and β and γ are the first and second hyperpolarizability tensors. We neglect the higher order terms here, and subsequently the laser-molecule interaction is given by

$$H_I = -\mu_0 E(t) \cos \theta - \frac{1}{2} E^2(t) ((\alpha_{\parallel} - \alpha_{\perp}) \cos^2 \theta + \alpha_{\perp}), \quad (3.16)$$

where the components of the polarizability α_{\parallel} and α_{\perp} are parallel and perpendicular to the molecular axis, respectively. The laser field in our consideration is a Gaussian shape centered at the time t_0 :

$$E(t) = E_0 e^{-\frac{(t-t_0)^2}{\sigma^2}} \cos(\omega t), \quad (3.17)$$

where E_0 is the field strength, σ is the pulse duration, and ω is the laser frequency.

To solve time-dependent Schrödinger equation, the wavefunction is expressed in terms of a series of eigenfunctions

$$\Psi(t) = \sum c_{l,m}(t) \psi_{l,m}(\theta, \phi), \quad (3.18)$$

where $c_{l,m}(t)$ is time-dependent coefficients corresponding to the quantum numbers (l, m) . As can be seen in the above section, the wavefunction for infinite

conical-well model is given by

$$\psi_{l,m}(\theta, \phi) = \begin{cases} A_{l,m} P_{\nu_{l,m}}^{|m|}(\cos \theta) \frac{\exp(im\phi)}{\sqrt{2\pi}}, & 0 \leq \theta \leq \alpha \\ 0, & \alpha < \theta \leq \pi \end{cases}, \quad (3.19)$$

where $A_{l,m}$ is the normalization constant and $P_{\nu_{l,m}}^{|m|}$ is associated Legendre function of arbitrary order. After determining the coefficients $c_{l,m}(t)$, the orientation $\langle \cos \theta \rangle$ and alignment $\langle \cos^2 \theta \rangle$ can be carried out immediately.

We choose ICl as our model molecule, whose dipole moment $\mu = 1.24$ Debye, rotational constant $B = 0.114 \text{ cm}^{-1}$, polarizability components $\alpha_{\parallel} \approx 18 \text{ \AA}^3$ and $\alpha_{\perp} \approx 9 \text{ \AA}^3$. The peak intensity and frequency of laser pulse is about $5 \times 10^{11} \text{ W/cm}^2$ and 210 cm^{-1} , respectively. For simplicity (zero-temperature case), the rotor is assumed in ground state initially, i.e. $c_{0,0}(t=0) = 1$. Besides, in order to keep the simulations promising, the highest quantum number for numerical calculations is $l = 15$, such that the results are convergent and the precision is to the order of 10^{-7} .

3.4 Results and discussion

The solid lines in the insets of Fig. 3.3 show the dependence of the alignment on hindered angle α . For $\alpha = 60^\circ$, sinusoidal-like behavior is presented, and the alignment ranges from 0.63 to 0.91. As the hindered angle increases, the curves become more and more complicated and gradually approach the free rotor limit as shown in the insets of Fig. 3.3(b) ($\alpha = 120^\circ$) and 3.3(c) ($\alpha = 180^\circ$). This

can be understood well by studying the populations $|c_{l,m}|^2$ of low-lying states. In the regime of small hindered angle, there is little chance for electron to populate in higher excited states since the shrinking of the conical-well angle causes the increasing of energy spacings.

One also notes that the populations of a hindered molecule for $\alpha = 60^\circ$ and 120° , shown in Fig. 3.4(a) and (b), mainly compose of $l = 0, 1$ and 2 states, while the population of a free rotor is composed of $l = 0, 2, 4$ states. The underlying physics comes from the reason that $\langle \psi_{l',m'} | \cos^2 \theta | \psi_{l,m} \rangle$ is non-zero for all l and l' values in the case of hindered rotation. But it is zero in free rotor limit except for $l = l'$ or $l = l' \pm 2$. The dotted lines in the insets represent the first two main contributions of the factors $\sum_{l \neq l'} \langle \psi_{l',m'} | \cos^2 \theta | \psi_{l,m} \rangle$ summed from low-lying states, i.e. the sum of the largest two values of the off-diagonal term $\langle \psi_{l',m'} | \cos^2 \theta | \psi_{l,m} \rangle$. As can be seen, the populations for small hindered angle are mainly distributed on lower states since the main oscillation feature (e.g. the frequency) of the curve (dotted lines) is quite similar to that from whole contributions (solid lines).

Let us now turn our attention to the case of orientation. After applying a short pulse laser, the orientation $\langle \cos \theta \rangle$ of a hindered molecule ($\alpha = 60^\circ$) oscillates sinusoidally with time as shown in Fig. 3.4(a). The value of $\langle \cos \theta \rangle$ is always positive because the rotational wavefunction is compressed heavily. As the hindered angle α becomes larger, the oscillation frequency also decreases as shown in Fig. 3.4(b). These signatures are quite close to that of the alignment. We

then conclude that even at larger hindered angle ($\alpha = 120^0$) the role of hindered potential still overwhelms the laser pulse, otherwise, the value of $\langle \cos \theta \rangle$ should not always be positive.

Fig. 3.4(c) represents results of orientations in infinite ($V_0 = \infty$) or finite ($V_0 = 100$) conical-well potential for $\alpha = 175^0$. Dashed and dotted lines correspond to $V_0 = \infty$ and 100, respectively. For the case of finite conical-well potential, the wavefunction is expressed in terms of a series of the basis wavefunctions obtained in Refs. [4, 5, 7]. As can be seen, the effect of laser pulse is obvious because negative value appears. Comparing the results with the free orientation [20], the angular distributions for finite well are more isotropic since the wave functions can penetrate into the conical-barrier.

Further analysis shows that components of orientation $\langle \cos \theta \rangle$ or alignment $\langle \cos^2 \theta \rangle$ can be divided into two parts: diagonal and nondiagonal terms. The nondiagonal term represents the variations of these curves such as those in the insets of Fig. 3.3. These variations with time are determined by the phase difference coming from various energy levels. To see the contributions from diagonal terms, we evaluate the time-averaged orientation and alignment. In this case, the nondiagonal values will be averaged out, and only contributions from diagonal terms exit. Fig. 3.5 shows the mean orientation and alignment as a function of hindered angle. As α increases, the mean orientation decreases monotonically from 1 to 0. This is because the mean orientation is determined by $|c_{l,m}|^2$ and

$\langle \psi_{l,m} | \cos \theta | \psi_{l,m} \rangle$. For a larger angle α , the populations $|c_{l,m}|^2$ mainly compose of $l = 0, 2, 4$ states. But the value $\langle \psi_{l,m} | \cos \theta | \psi_{l,m} \rangle$ is governed by the selection rule: $l = l' + 1$. Thus the net effect is the shrinking of the mean orientation in large angle limit.

Contrary to orientation, the mean alignment shows a quite different feature. The value of $\langle \cos^2 \theta \rangle$ first decreases as α increases. However, it reaches a minimum point about for $\alpha = 140^\circ$. From the insets of Fig. 3.5, we know that the values of $(\langle \psi_{l,m} | \cos^2 \theta | \psi_{l,m} \rangle)$ do not depend significantly on α . Therefore, the decrease of $\langle \cos^2 \theta \rangle$ comes from the decreasing tendency of the population $|c_{l=1,m}|^2$, while its increasing behavior is caused by other two populations $|c_{l=0,m}|^2$ and $|c_{l=2,m}|^2$. Competition between these two effects results in a minimum point.



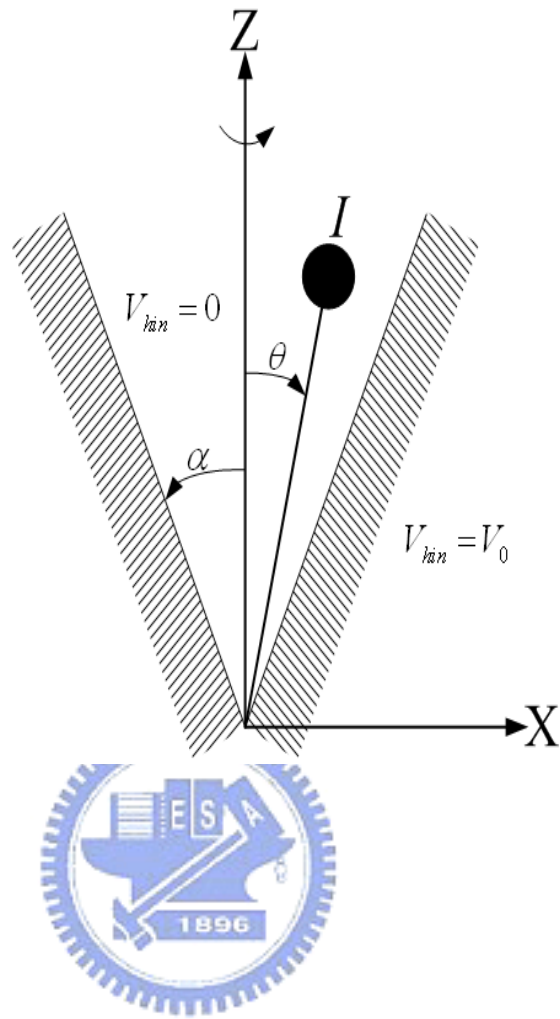


Figure 3.1: Schematic view of the hindered rotor.

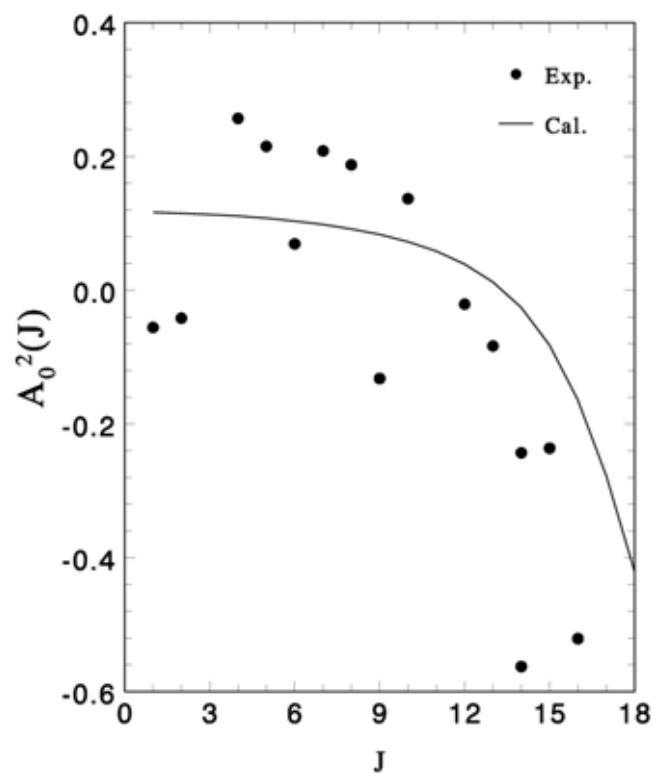


Figure 3.2: Quadrupole moments for the desorption of CO from $\text{Cr}_2\text{O}_3(0001)$ as function of quantum number J . Filled circles: experimental data points.

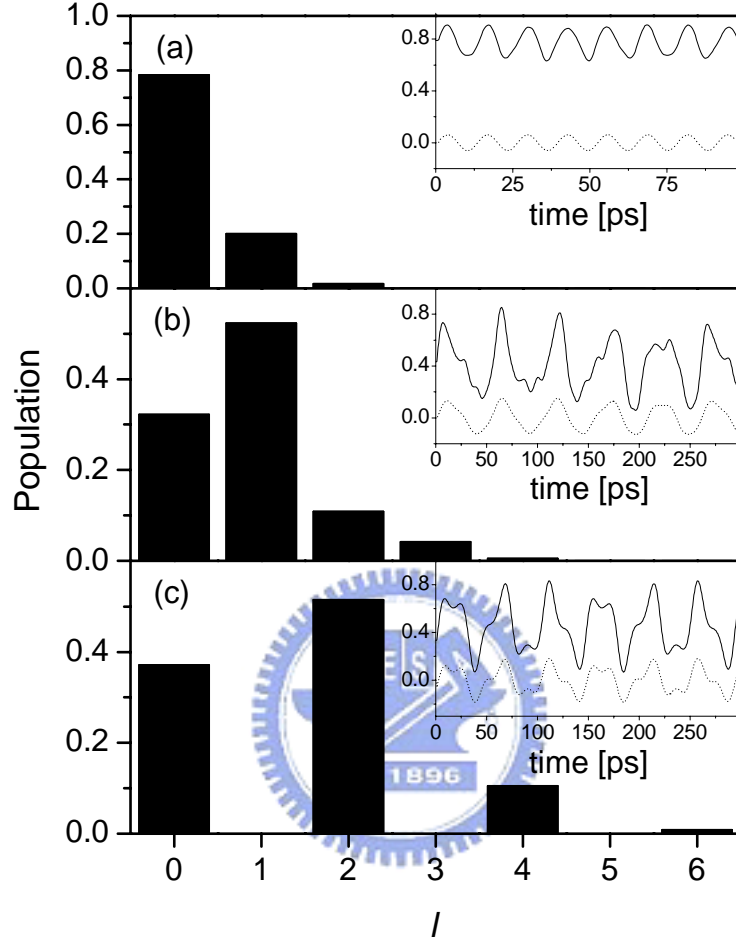


Figure 3.3: The populations of the states $(l, m = 0)$ for different hindered angles: (a) $\alpha = 60^\circ$, (b) $\alpha = 120^\circ$, (c) $\alpha = 180^\circ$. The insets show the corresponding alignments (solid lines) and the first two main contributions of the factors

$$\sum_{l \neq l'} \langle \psi_{l',m'} | \cos^2 \theta | \psi_{l,m} \rangle \text{ (dotted lines).}$$

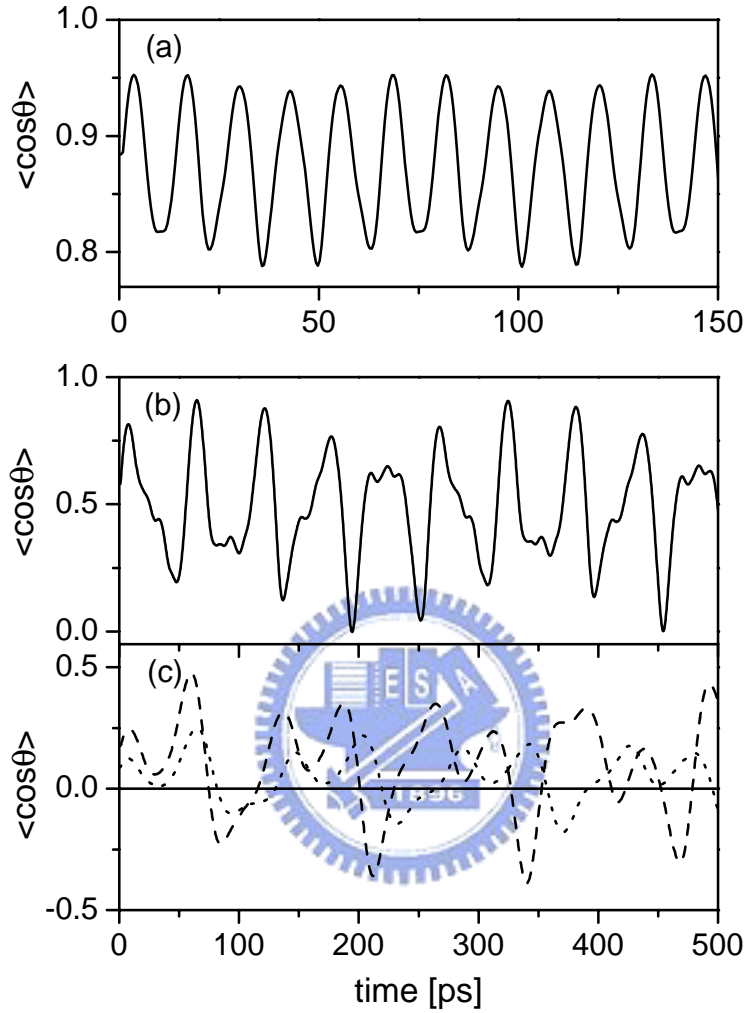


Figure 3.4: The orientations $\langle \cos \theta \rangle$ (solid lines) of a hindered molecule confined by infinite conical-well for different hindered angles: (a) $\alpha = 60^\circ$, (b) $\alpha = 120^\circ$, (c) $\alpha = 175^\circ$. The dashed and dotted lines in (c) correspond to different potential barrier height, i.e. $V_0 = \infty$ and 100, respectively.

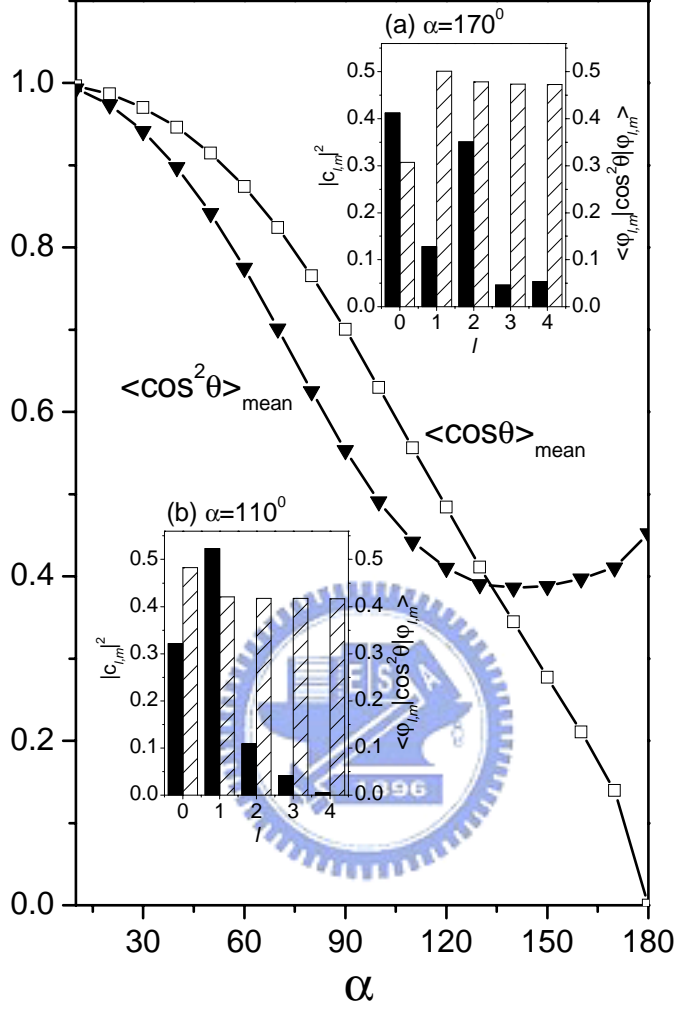


Figure 3.5: The mean orientation $\langle \cos \theta \rangle_{\text{mean}}$ and alignment $\langle \cos^2 \theta \rangle_{\text{mean}}$ in infinite conical-well. The insets show the populations $|c_{l,m}|^2$ (filled bar) and factors $\langle \psi_{l,m} | \cos^2 \theta | \psi_{l,m} \rangle$ (sparse bar). Insets (a) and (b) correspond to $\alpha = 110^\circ$ and $\alpha = 170^\circ$, respectively.

CHAPTER 4

COUPLED FREE MOLECULES IN LASER FIELDS

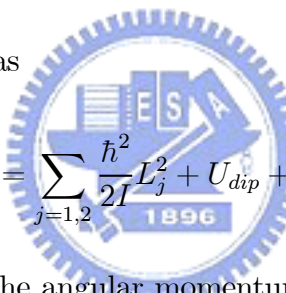
Recently, coupled-rotor- model attracts much interest because some physical properties such as dielectric response may display peculiar behaviors in the presence of dipole-dipole interaction. In some materials, molecules are found to show a free rotation. For example, NH_3 groups behave like one-dimensional quantum rotors in certain Hofmann clathrates [25]. In particular, a line broadening mechanism is proposed based on rotor-rotor coupling. With the advances of nanotechnology, one can investigate the quantum rotors which are mounted on the surfaces [29, 30, 31]. From the laser spectroscopy, two individual fluorescent molecules separated by several nanometers on the surface of an organic crystal can be resolved. The coherent interactions between the dipole moments associated with their optical transitions are found in the quantum optical measurements. The strong dipole-dipole coupling produces entangled subradiant and superradiant states in the two molecules system under laser radiation [30].

Many efforts have been devoted to generate entanglement in quantum-optic and atomic systems. Although some studies have been investigated on quantum rotors, these works are limited in the model of kicked tops [43, 44]. In this chapter, we consider a more realistic system. A method is proposed to create entanglement

between two coupled identical polar molecules separated in a distance of tens of nanometers. Both molecules are assumed to be irradiated simultaneously by the laser pulses. It is found that the entanglement induced by the dipole interaction can be affected by controlling the inter-molecule distance, the field strength, and the number of laser pulses. Moreover, the crossover from quantum to classical limit is also discussed by varying the Planck constant.

4.1 Model of two coupled free molecules in a strong laser pulse

Consider now two diatomic polar molecules (e.g. NaI) separated in a distance of R . The molecule system is irradiated by half-cycle pulses. The total Hamiltonian can be written as



$$H = \sum_{j=1,2} \frac{\hbar^2}{2I} L_j^2 + U_{dip} + H_I, \quad (4.1)$$

where L_j^2 and $\frac{\hbar^2}{2I}$ ($= B$) are the angular momentum operator and rotational constant, respectively. U_{dip} is the dipole interaction between two molecules:

$$U_{dip} = \frac{[\vec{\mu}_1 \cdot \vec{\mu}_2 - 3(\vec{\mu}_1 \cdot \hat{e}_R)(\vec{\mu}_2 \cdot \hat{e}_R)]}{R^3}, \quad (4.2)$$

where $\vec{\mu}_1$ and $\vec{\mu}_2$ are the dipole moments. The dipole moments of two molecules are assumed, for simplicity, to be identical, i.e. $\mu_1 = \mu_2 = \mu_0$. The field-molecule coupling H_I can thus be expressed as

$$H_I = - \sum_{i=1,2} \mu_0 E(t, v) \cos \theta_i, \quad (4.3)$$

where θ_1 and θ_2 are angles between dipole moments and laser field. The laser field is given by $E(t, v) = E_0 f(t) \cos(2\pi vt)$, where E_0 is the field strength and v is the frequency. The envelope function $f(t)$ is assumed to be Gaussian shape centered at the time $t = t_0$ with duration σ , i.e. $f(t) = e^{-(t-t_0)^2/\sigma^2}$. Traditionally, a half-cycle pulse is a strongly asymmetric monocycle pulse that consists of two parts: a very short, strong pulse and a much long and weak tail of opposite electrical field. The pulses $E(t, v)$ used in the present work are actually not the exact half-cycle pulses as defined in Ref. [45]. However, practical calculation shows that there is almost no influence on our final result if a long and weak tail is introduced in the pulses $E(t, v) = E_0 f(t) \cos(2\pi vt)$. Thus, it is reasonable to model a half-cycle pulse by using the function $E(t, v)$ in our calculation. In addition, the field duration is considered to be much shorter than the molecular rotational period in our work. Based on these conditions, an impulsive model can be employed in this case [20, 21]. The time-dependent Schrödinger equation can be solved by expanding the wave function Ψ in terms of a series of field-free spherical harmonic functions $Y_{l,m}(\theta, \phi)$ as

$$|\Psi\rangle = \sum_{l_1, m_1; l_2, m_2} c_{l_1, m_1; l_2, m_2}(t) |Y_{l_1, m_1}(\theta_1, \phi_1)\rangle |Y_{l_2, m_2}(\theta_2, \phi_2)\rangle, \quad (4.4)$$

where (θ_1, ϕ_1) and (θ_2, ϕ_2) are the coordinates of the first and second molecule respectively. The time-dependent coefficients $c_{l_1, m_1; l_2, m_2}(t)$ correspond to the quantum numbers $(l_1, m_1; l_2, m_2)$ and can be determined by solving Schrödinger equations numerically. In equation (4.4), the inter-molecule separation R is assumed to

be fixed for simplicity, so that the total wavefunction has no spatial dependence. Although the variation of R might be inevitable due to the influence of laser fields or inter-molecule vibrations, however, recent experiments exhibited that the spatial resolution in tens of nanometers for two individual molecules hindered on a surface is practically possible [29, 30, 31]. In principle, the free orientation model can be easily generalized to the hindered ones by replacing the spherical harmonic functions with hindered wavefunctions.

4.2 Entanglement of two coupled free molecules

Let us now focus on the entanglement generated in our system. The coupled molecules can be expressed as a pure bipartite system. The reduced density operator for the first molecule is defined as



$$\rho_{\text{mol1}} = \text{Tr}_{\text{mol2}} |\Psi\rangle\langle\Psi|. \quad (4.5)$$

To study the degree of entanglement, the bases of molecule 1 is transformed to make the reduced density matrix ρ_{mol1} to be diagonal. The entangled state can be represented by a biorthogonal expression with positive real coefficients λ_{lm} which can be obtained by diagonalization of density matrix ρ_{mol1} . The degree of entanglement for the coupled molecules can then be measured by von Neumann entropy [46, 47]

$$\text{Entropy} = - \sum_{l,m} \lambda_{l,m} \log_n \lambda_{l,m}. \quad (4.6)$$

In our work, NaI molecule in the ground state with dipole moment 9.2 debyes and rotational constant 0.12 cm^{-1} is used. The field strength is $3 \times 10^7 \text{ V/m}$ and the laser frequency is about $9 \times 10^{11} \text{ s}^{-1}$. The duration and center of the pulse are set equal to 279 fs and 1200 fs. The main feature is that the ratio in magnitude of the positive and negative peak value of the laser pulse is 5 : 1. Unless specified, the parameters of the pulse are fixed throughout the chapter. The crossover from non-entangled case to entangled one is studied based on the initial condition: $c_{0,0;0,0}(t = 0) = 1$.

4.3 Results and discussion

After the coefficients $c_{l_1, m_1; l_2, m_2}(t)$ are determined, the orientations $\langle \cos \theta_1 \rangle$ and $\langle \cos \theta_2 \rangle$ can be evaluated immediately. Fig. 4.1 shows the orientations of the first and second molecules after a single laser pulse is applied on both molecules. For $R = 3 \times 10^{-8} \text{ m}$, the behavior of the first molecule is quite close to that of a free rotor [20]. This is not surprising because the dipole interaction is weak for this molecule separation. However, as two molecules get close enough (Fig. 4.1(b)), both molecules orient disorderly, and the periodic behavior disappears. This is because the dipole interaction is increased as the distance between the molecules is decreased, and the energy exchange between two molecules becomes more frequently. The regular orientation caused by the laser pulse is inhibited by the mutual interaction.

The populations of some low-energy levels are shown in the lower panels of Fig. 4.1(a) and (b). The solid, dashed, and dotted lines represent the populations of the states $(1,0;0,0)$, $(1,0;1,0)$, and $(2,0;1,0)$, respectively. These states show different degrees of periodic behavior at different distances. However, the populations of some higher excited states, for example the $(3,0;1,0)$ state in the inset of Fig. 4.1(b), display different degrees of irregularity. This manifests a fact that the nonlinear effect, caused by the reduction of R , does not affect the regularity of the low-lying states, and the origin of the irregularity is caused by the higher excited states.

Consider now the molecules are irradiated by a series of laser pulses periodically. As shown in Fig. 4.2(a), if the period of the applied periodically laser pulse T is equal to \hbar/B , then both molecules behave disorderly no matter how the distance R is varied. The chaotic behavior of the molecules can be ascribed to the well-known "kicked-rotor" problem. However, a series of regular-like orientations marked by dotted and dashed lines are present in Fig. 4.2(b) if T is equal to $\pi\hbar/B$. For a free rotor under a single kick, this interesting phenomenon comes from the situation as the magnitude of the orientation returns to its initial condition ($\langle \cos \theta \rangle = 0$) after a certain period T [20]. Therefore, for two molecules in weak interaction limit ($R = 3 \times 10^{-8}$ m), the wavepacket-like orientation is similar to that of a single free rotor under the same laser period. The difference is the suppression of the amplitudes at long time (dashed lines). It means that

the dipole force can generate some accidental phases to perturb the regularity of the coupled system. The lower panel of Fig 4.2(b) exhibits that the suppression of the regularity is quicker if the dipole force is stronger.

Fig. 4.3 shows the time-dependent entropy after one pulse passes through this system. For inter-distance $R = 5 \times 10^{-8}$ m, the entropy increases slowly from zero. For $R = 1.5 \times 10^{-8}$ m, on the contrary, the entropy grows rapidly with the increasing of time because the dipole force is stronger. Notes that the entropy only varies within a finite range at long time regime. This indicates that the systems reaches a dynamic equilibrium state even though the dipole force is still present.

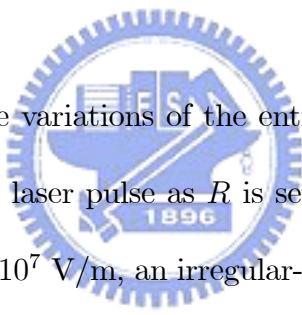


Fig. 4.4(a) illustrates the variations of the entropy with respect to different field strengths of the applied laser pulse as R is set equal to 1.5×10^{-8} m. For the field strength $E_0 = 1.5 \times 10^7$ V/m, an irregular-like behavior of the entropy is obtained, and its value is not large enough for quantum information processing. However, Fig. 4.4(b) shows that the degree of entanglement can be enhanced if one increases the field strength. This can be understood well by studying the relationship between the dipolar interaction and the field strength. If the effect of dipole interaction overwhelms the laser field, most of the populations are distributed on the low-lying states. In this case, the entropy from Schmidt decomposition is certainly small as shown in Fig. 4.4(a). On the other hand, if the field strength plays a dominant role, the distribution of molecular states covers a wider range

and the entropy is enhanced in this limit.

Next we detune the frequencies of the laser fields to study the behavior of entanglement. Figure 4.5 illustrates the time evolution of the entropy with different ratios in magnitude of the positive and negative peak value of the laser pulse as R is set equal to 1.5×10^{-8} m. The laser frequency is tuned to change the ratio as shown in the inset by fixing other parameters. For the case of ratio 9 : 1, an irregular-like behavior is obtained with time-averaged value 0.51. If the ratio is set equal to 1 : 1, the entanglement shows a nearly periodic behavior with small averaged entropy. This result is very similar to the limiting case without laser, and indicates that the entanglement depends sensitively on the ratio of the laser pulse, i.e. the excitation is suppressed under the condition of 1 : 1 ratio. Meanwhile, the dipole force only establishes periodic-like entropy.

Let us consider the first ten most contributive coefficients $\lambda_{l,m}$. The $\lambda_{l,m}$ are re-arranged and denoted as λ_p with $p = 1, 2, 3, \dots$. For example, λ_1 is the most contributive coefficient. The insets of Fig. 4.5 show the ten coefficients (λ_p) at short and long time regimes. In the case of the ratio 9 : 1, the eigenvalue λ_1 dominates the contributions at short time regime ($t = 50$ ps). However, the contributions are distributed more averagely between different levels as $t = 800$ ps regime. This means the system is in some sort of dynamic equilibrium in long time limit, and entropy saturates to certain value. On the contrary, λ_1 always dominates the contributions for either short or long time regime in the case of the

ratio 1 : 1 as shown in the lower inset of Fig. 4.5. From statistical point of view, this somehow explains the suppressed and regular behaviors of the entanglement (entropy).

Figure 4.6 shows the time evolutions of the populations of the eigenstates for different ratio of pulse shapes. For 1 : 1 ratio, the pulse hardly excites the rotors from the initial energy level $(0, 0; 0, 0)$. Therefore, $(0, 0; 0, 0)$ is still the mostly populated level (the population value is nearly close to 1) as shown in the lower panel of Fig. 4.6 while the pulse passes through. Similar to the ground state, the populations of the higher levels (the inset of Fig. 4.6) also show the periodic behavior. The periodic behavior is ascribed to the dipole interaction. Since the small fluctuation of the population is dominated by the dipole interaction in the case of symmetrical pulses. The magnitudes of the periodic fluctuations in higher level populations are rather small with the periodic evolution of the entropy. On the other hand, for 9 : 1 ratio the populations of the higher states show different degrees of irregularity as shown in the upper panel of Fig. 4.6. This is because a single asymmetrical pulse can generate high populations in the excited states [20], i.e. a larger angle orientation. The larger angle orientation can cause a largely fluctuated dipole interaction between the molecules. For this situation, energy transfer by means of (mediated) dipole interaction generates the irregular evolutions of the higher excited states which result in a randomly time-varying entropy.

We further study the entropy for different separation and dipole moment in Fig. 4.7. The ratio is set equal to 9 : 1. If the separation is smaller ($0.8 R$), the entropy grows faster. On the contrary, the entropy evolves slower for the case of larger separation. This means that the system needs much more time to approach the dynamic equilibrium. We also study the time evolution of entropy by changing the dipole moment. Our result shows that a similar behavior of the entropy exhibits, i.e. the strength of dipole interaction governs the behavior of evolution.

By adjusting the laser parameters, one can vary the degree of the entanglement. Figure 4.8 illustrates the time evolution of the entropy under single pulse or double pulses with ratio 5 : 1. As can be seen, an irregular behavior of the entropy is obtained, but their averaged values are different. For single kick, the populations are first dominated by this laser pulse. Then, the dipole interaction plays a key role to raise the entanglement in the system. In the case of double pulses the finite populations is created by first pulse. As the second laser pulse passes through, the populations will be redistributed to a wider range. Since the populations are distributed more averagely in this case, the entropy is certainly larger as shown by the solid line in Fig. 4.8. One can notes that the enhancement of entropy is achieved by applying the second laser pulse. Consider the case that time separation between these two pulses is set to be 5 times the center of the laser peak. Here we emphasize that the time separation is not fixed and can be

tuned to obtain different degree of entropy. Another way to control the degree of entanglement in this system is to change the positive and negative ratios of the laser pulse. Inset of Fig. 4.8 shows the time-averaged entropy with respect to different ratios. We find that the entropy is more enhanced as the ratio is larger. This means that the highly asymmetric laser pulse can generate larger entropy under the same field strength.

To study the crossover behavior from quantum to classical limit in this system, one can tune the fundamental Planck constant \hbar' . Figure 4.9 shows the time for entropy first exceeds the time-averaged value (arrow in the inset) versus the different factor of Planck constant \hbar' . As shown, the time grows rapidly with the decreasing of the Planck constant \hbar' . The inset in Fig. 4.9 shows a slowly increasing of entropy with the evolution of time for $\hbar' = 0.01\hbar$. Comparing this with the result for $\hbar' = \hbar$, the ratio of the two times is roughly 100 : 1. This means that the entropy evolves slowly, and the system needs a longer time to approach dynamical equilibrium for a small \hbar' . As expected, the time for classical limit ($\hbar' \rightarrow 0$) goes to infinity, satisfying that no entanglement exists between classical objects.

For a more realistic molecular system, one can extend our model to hindered-rotor system. The hindered rotor means that the polar diatomic molecule is adsorbed on the surface with the confinement of surface potential. In other words, one reasonably considers that two coupled polar molecules are adsorbed on the

surface with the dipole interaction. Comparing hindered rotor with free one, the rotation of a hindered rotor is similar to that for the free one, but the degree of orientation is different. This is because that the surface potential confines the rotation. Although this confinement may affect the property of the system, according to our work in chapter 3, a free rotor and hindered rotor actually show the same physics. In particular, a hindered rotor can be transformed into a free one by changing the parameters of surface potential.



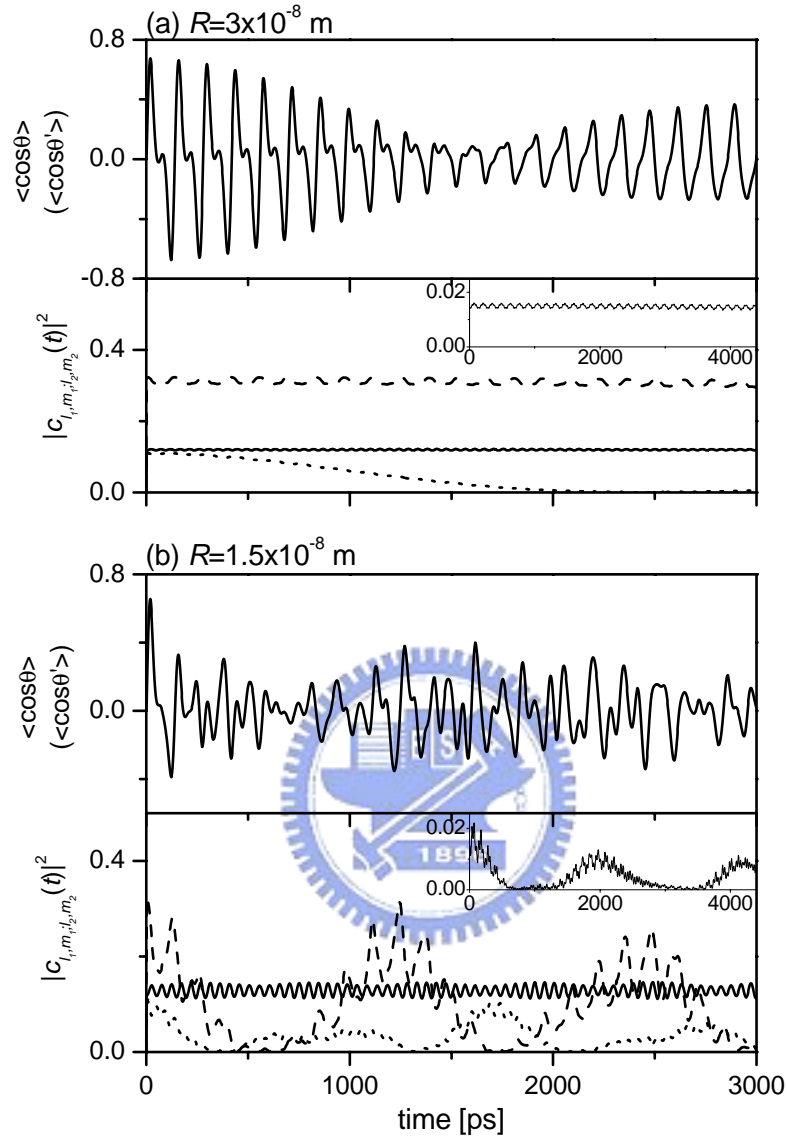


Figure 4.1: Upper panels of Fig. 4.1(a) and (b) show the orientations of the two molecules at different distances. Lower panels: The populations of the states $(l_1, m_1; l_2, m_2) = (1, 0; 0, 0)$ (solid lines), $(2, 0; 1, 0)$ (dotted lines), $(1, 0; 1, 0)$ (dashed lines). The insets in (a) and (b) represent the population of state $(3, 0; 1, 0)$.

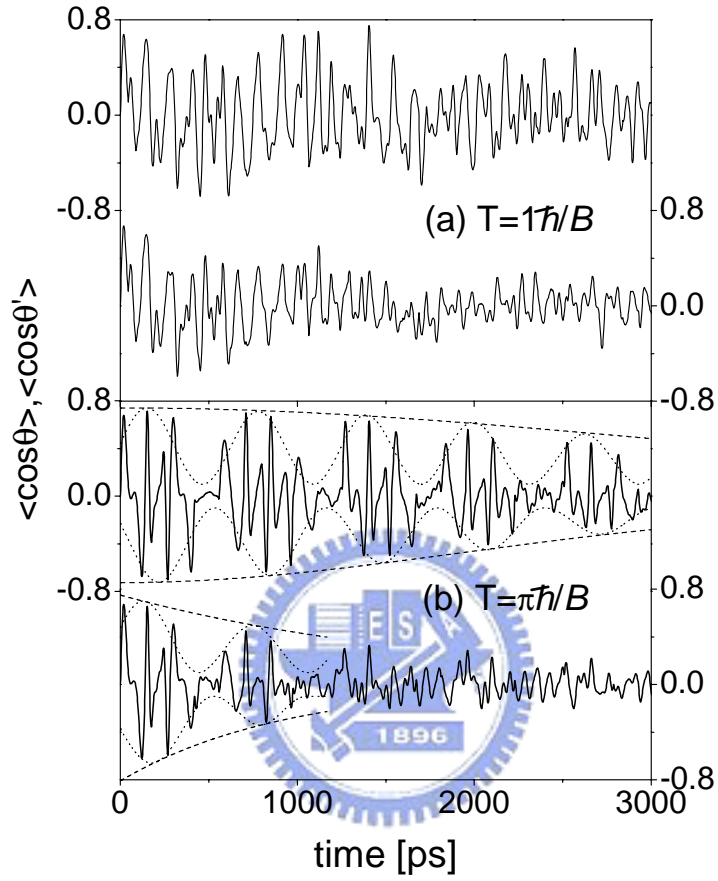


Figure 4.2: The orientations of the first and second molecules under periodic laser pulses with the periods $T =$ (a) $1\hbar/B$, (b) $\pi\hbar/B$ ps. The upper and lower panels of (a) and (b) correspond to the distances $R = 3 \times 10^{-8}$ and 2×10^{-8} m, respectively.

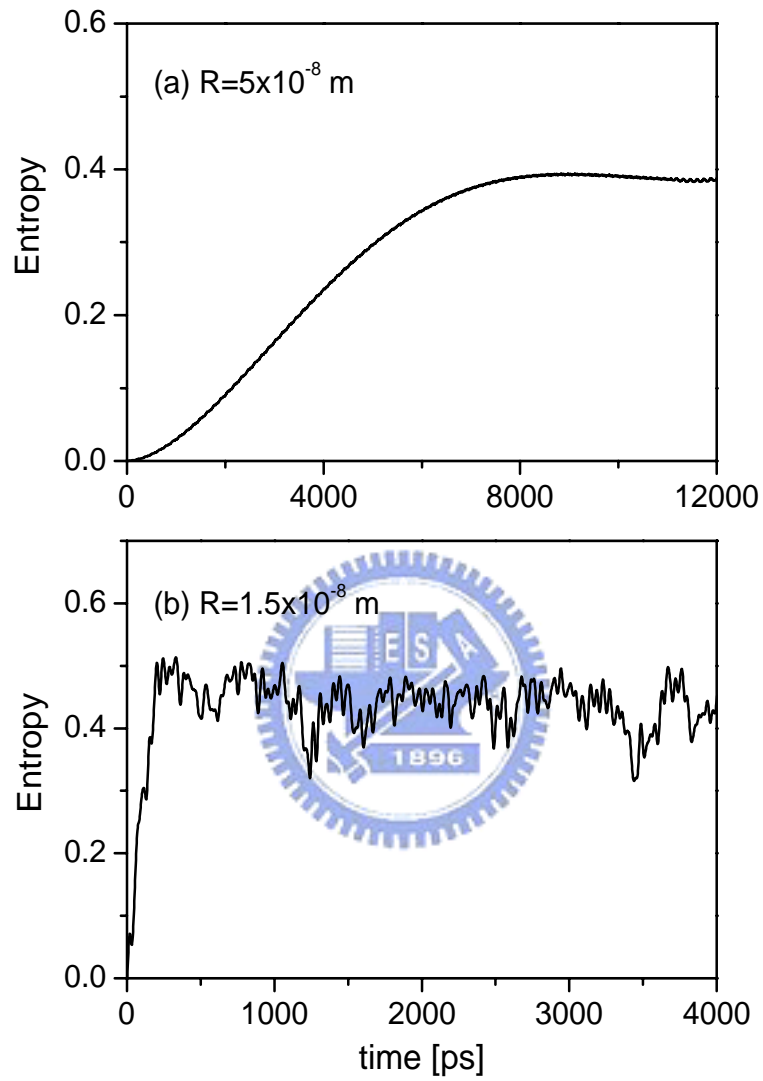


Figure 4.3: Time evolution of the entropy after applying single laser pulse for (a)

$R = 5 \times 10^{-8} \text{ m}$ and (b) $R = 1.5 \times 10^{-8} \text{ m}$.

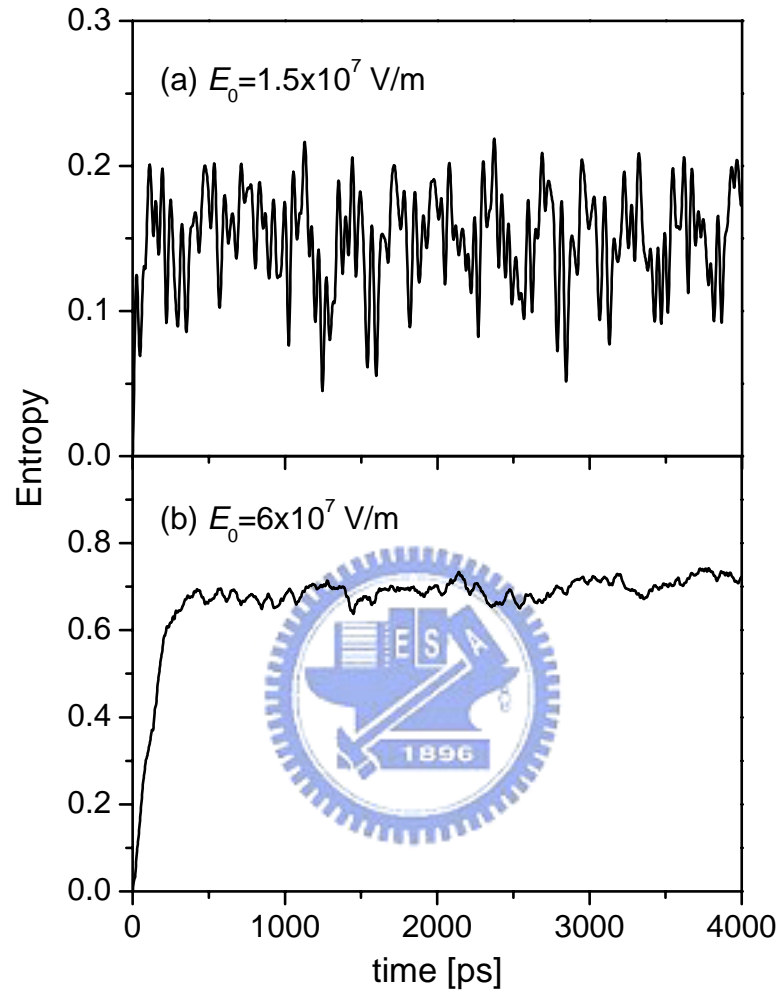


Figure 4.4: Time evolution of the entropy for inter-molecule separation $R = 1.5 \times 10^{-8}$ m. The degree of entanglement can be enhanced if one increases the field strength.

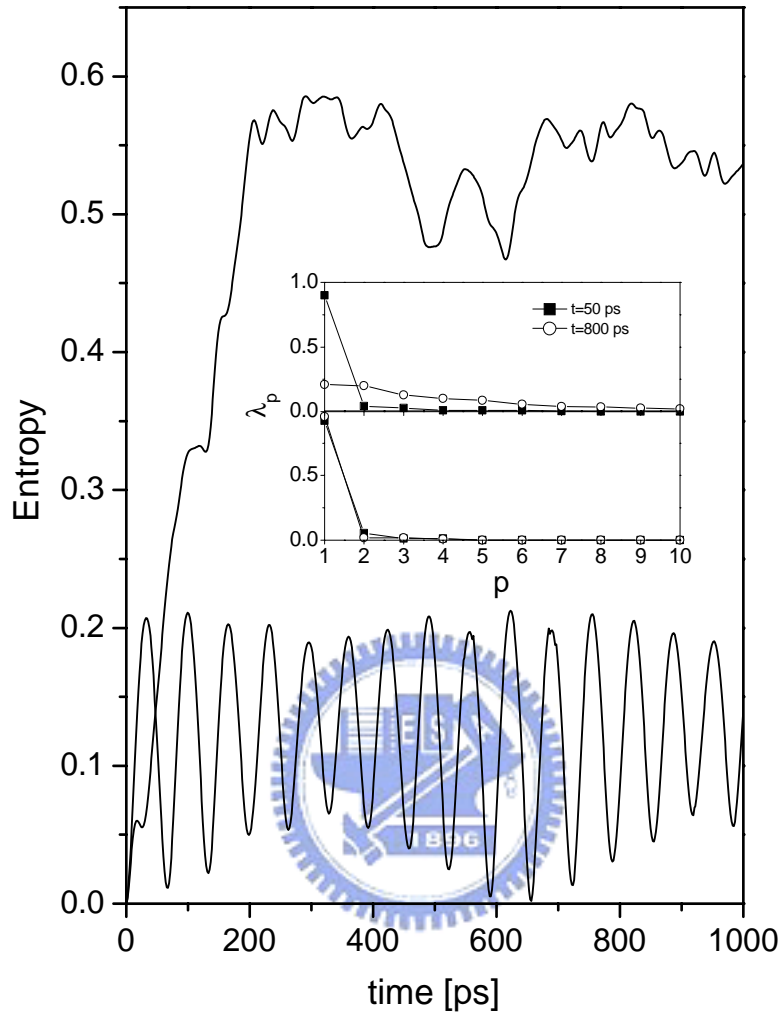


Figure 4.5: Time evolution of the entropy after applying single laser pulse for different ratios in magnitudes of the positive and negative peak value of the laser pulse. The graphs show the irregular (periodic) behavior for ratio 9 : 1 (1 : 1). The inset : the first ten contributive eigenvalues λ_p at short time ($t = 50$ ps) and long time ($t = 800$ ps).

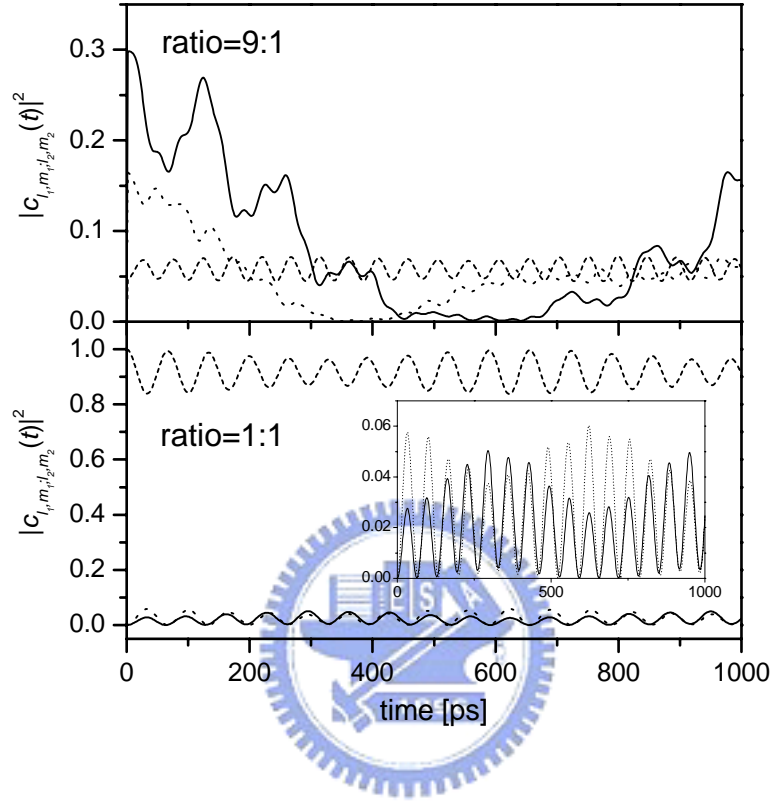


Figure 4.6: Populations of the states $(l_1, m_1; l_2, m_2)$ for different ratios. Upper panel : $(1, 0; 0, 0)$ (dashed line), $(1, 0; 1, 0)$ (solid line), $(2, 0; 1, 0)$ (dotted line). Lower panel : $(0, 0; 0, 0)$ (dashed line), $(1, 0; 1, 0)$ (solid line), $(1, 1; 1, 1)$ (dotted line). The inset in the lower panel is the enlarged figure showing the states $(1, 0; 1, 0)$ (solid line), $(1, 1; 1, 1)$ (dotted line), respectively.

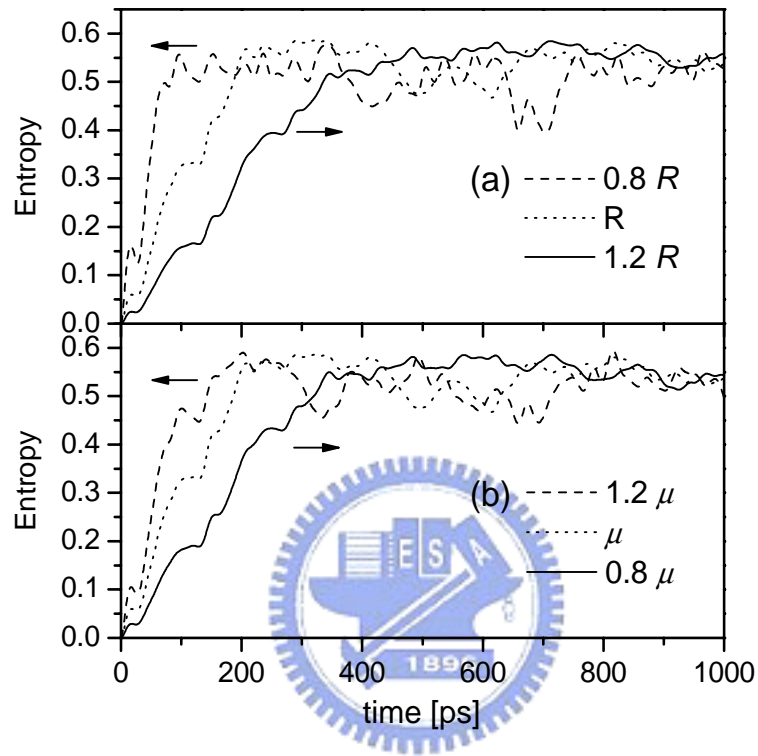


Figure 4.7: Time evolution of the entropy for different separation and dipole moment under single pulse (ratio 9 : 1). The dotted curve shows the case of $R = 1.5 \times 10^{-8}$ m and $\mu = 9.2 D$. The dashed and solid curves correspond to (a) $0.8 R$ and $1.2 R$, or (b) 1.2μ and 0.8μ , respectively.

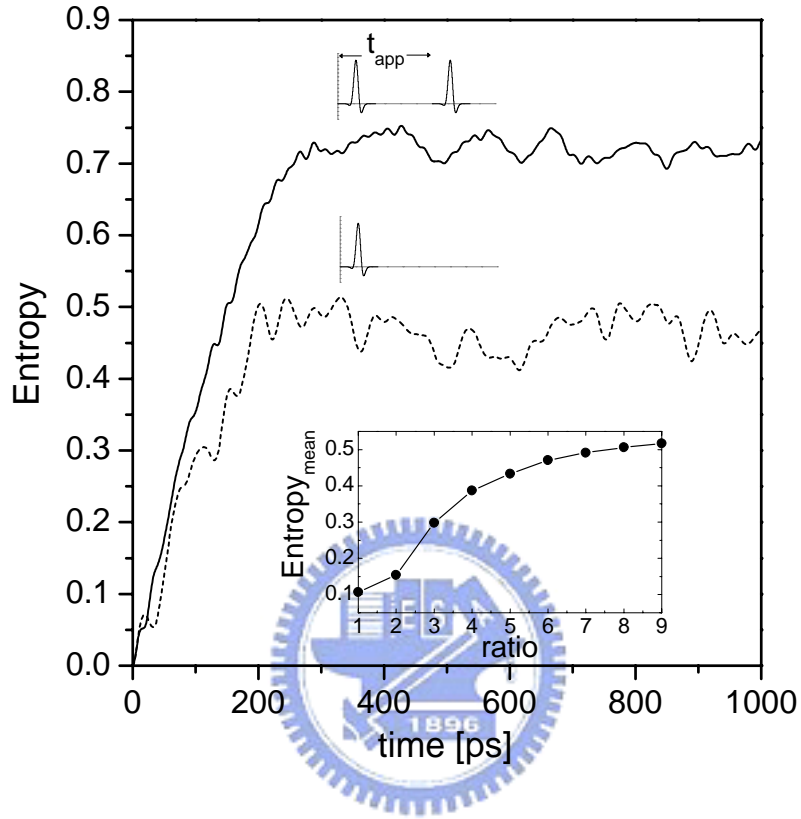


Figure 4.8: Time evolution of the entropy for fixed ratio 5 : 1 under single pulse (dashed line) and double pulses (solid line). Time separation (t_{app}) between two pulses is set to be 5 times the center of the laser peak. The inset : Dependence of the time-averaged entropy on the pulse shape for inter-molecule separation $R = 1.5 \times 10^{-8}$ m.

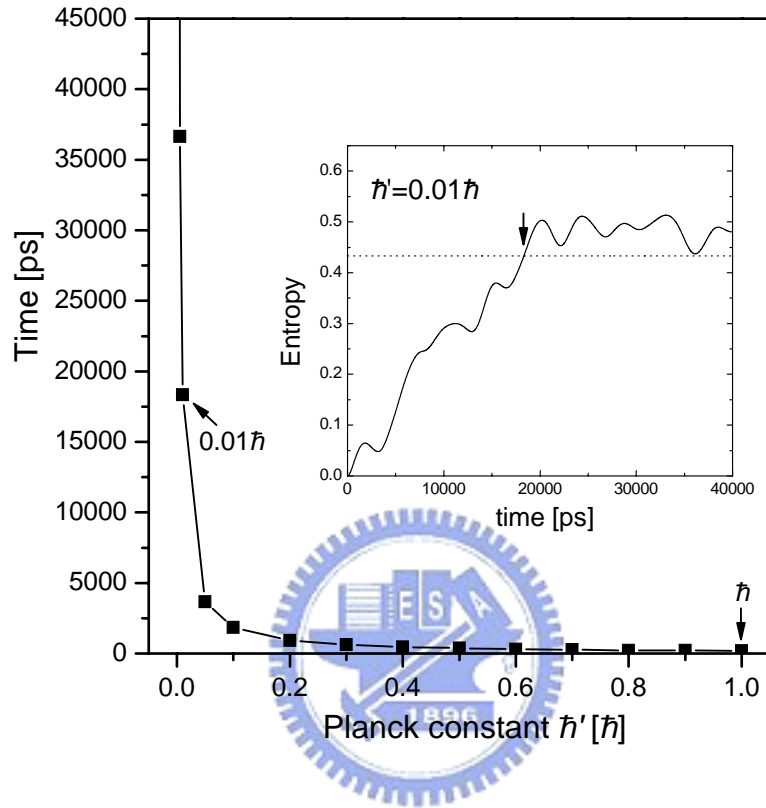


Figure 4.9: The time with respect to different Planck constant \hbar' for fixed field strength $E_0 = 3 \times 10^7$ V/m and inter-molecule separation $R = 1.5 \times 10^{-8}$ m. The time is defined as the first time in entropy that exceeds the time-averaged value (the arrow in the inset). The inset : the time-averaged value (dotted line), and time evolution of the entropy for $\hbar' = 0.01\hbar$ (solid line).

CHAPTER 5

COUPLED ADSORBED MOLECULES IN LASER FIELDS

In the complex surface systems, adsorbed molecules may not be isolated. Several studies have shown that interesting behavior can occur due to the existence of dipole-dipole interaction [24, 25, 26, 27, 28]. In addition, since the investigations on entangled behavior of two coupled rotors are limited in the model of kicked tops [43, 44], this inspires us to study the dynamical entanglement of adsorbed molecules. According to our study in chapter 3, it is found that the orientations of free coupled rotors somehow reflect the entropy of the system and thus relate to the measurement of entanglement. Since the entanglement measurement is one of the fundamental important issues in quantum information research, the study of the entanglement and its measurement becomes an interesting problem. Moreover, from the experimental point of view, it is still not clear how to keep two free rotors with fixed distance. Therefore, this makes it more interesting to consider a more realistic system and discuss the corresponding entanglement dynamics.

In this chapter, we investigate the rotational motions of a polar diatomic molecule confined by a hindering conical-well. After applying a single strong laser

pulse, the hindered rotor shows periodic behavior. Different signatures between the finite-conical-well and infinite-conical-well model on orientations are pointed out. Besides, the amplitudes of the oscillations are varied by applying different widths of the pulse. Furthermore, we also consider two coupled identical polar molecules adsorbed on the surface with the dipole-dipole interaction and a simultaneously ultra-short laser pulse shined upon them. It is found that both the entanglement (the von Neumann entropy) and orientation show interesting behaviors.

5.1 Single adsorbed molecule in a strong laser pulse

Consider now a dipolar molecule (e.g. NaI) adsorbed on the surface. The rotation of the molecule is confined by the surface potential as shown in Fig. 5.1. An off-resonant laser field polarized in z -direction interacts with the hindered rotor. Because the laser frequency is much lower than the frequencies of the lowest vibrational and electronic transition, only the rotational excitations can occur in our model. The excitations can be viewed as two photon transitions between two different rotational states through a high intermediate virtual state [18]. The Hamiltonian without the field-molecule interaction can be written as

$$H_0 = BJ^2 + V_{hin}(\theta, \phi), \quad (5.1)$$

where B and J^2 are rotational constant and angular momentum. V_{hin} denotes the surface potential and confines the rotation of adsorbed molecule. For simplicity,

the infinite-conical-well model $V_{hin}(\theta, \phi)$ is considered here. According to the previous studies, its dependence on ϕ is weaker than that on θ [32, 33, 34]. We reasonably assume that the surface potential is independent of ϕ . Therefore, in the vertical adsorbed configuration, the surface potential can be written as [3]

$$V_{hin}(\theta) = \begin{cases} 0, & 0 \leq \theta \leq \alpha \\ \infty, & \alpha < \theta \leq \pi \end{cases}, \quad (5.2)$$

where α is the hindering angle of the conical well.

The Hamiltonian concerning the field-molecule interaction can be written as

$$H_d = -\mu E(t) \cos \theta, \quad (5.3)$$

$$H_{ind} = -\frac{1}{2} E^2(t) ((\alpha_{\parallel} - \alpha_{\perp}) \cos^2 \theta + \alpha_{\perp}). \quad (5.4)$$

The first term H_d describes a permanent dipole moment μ coupling with an external field, and θ is the angle between the molecular axis and the field. In this work we choose a Gaussian pulse for our calculation, i.e. $E(t) = E_0 e^{-(t-t_0)^2/\sigma^2} \cos(2\pi\nu t)$, where E_0 is the field strength and ν is the laser frequency. The pulse is centered at the time t_0 , and σ is the pulse duration. The second term H_{ind} is a higher order interaction, in which the external field couples with the induced molecular polarization. The component of the polarizability α_{\parallel} (α_{\perp}) is parallel (perpendicular) to the molecular axis. According to our parameters, the field-dipole-moment interaction H_d is much greater than that of the field-induced-dipole-moment interaction H_{ind} in our model. This is because the strength of electric field used here is insufficient to enhance the higher order term. Actually the interaction

H_{ind} can play an important role in the case of high strength of electric field [18].

Therefore, the term (H_{ind}) can be neglected reasonably based on our parameters.

Before solving the time-dependent Schrödinger equation ($H_0 + H_d$), the eigenfunctions of the system ($H_0 = BJ^2 + V_{hin}(\theta)$) must be introduced first. Following Ref. [3], the eigenfunctions can be written as

$$\psi_{lm}(\theta, \phi) = \begin{cases} A_{l,m} P_{\nu_{l,m}}^{[m]}(\cos \theta) \frac{\exp(im\phi)}{\sqrt{2\pi}}, & 0 \leq \theta \leq \alpha \\ 0, & \alpha < \theta \leq \pi \end{cases}, \quad (5.5)$$

where $A_{l,m}$ is the normalization constant and $P_{\nu_{l,m}}^{[m]}$ is the associated Legendre Function of arbitrary order with the corresponding quantum number (l, m). In above equations, the molecular rotational energy can be expressed as

$$\epsilon_{l,m} = \nu_{l,m}(\nu_{l,m} + 1)B. \quad (5.6)$$

In order to determine $\nu_{l,m}$, one has to match the boundary condition

$$P_{\nu_{l,m}}^{[m]}(\cos \alpha) = 0. \quad (5.7)$$

To solve time-dependent Schrödinger equation, the wavefunction is expressed in terms of a series of eigenfunctions:

$$\Psi(t) = \sum_l c_{l,m}(t) \psi_{l,m}(\theta, \phi), \quad (5.8)$$

where $c_{l,m}(t)$ is time-dependent coefficient. The coefficient $c_{l,m}(t)$ can be obtained from the different equations

$$i\hbar \dot{c}_{l,m}(t) = c_{l,m}(t) \epsilon_{l,m} + \sum_{l'} c_{l',m}(t) \langle \psi_{l,m} | H_d | \psi_{l',m} \rangle. \quad (5.9)$$

After determining the coefficients $c_{l,m}(t)$, the orientation $\langle \cos \theta \rangle$ can be carried out immediately. We choose NaI as our model molecule, whose dipole moment $\mu = 9.2$ Debye and rotational constant $B = 0.12 \text{ cm}^{-1}$. For simplicity (zero-temperature case), the rotor is assumed in ground state initially, i.e. $c_{0,0}(t=0) = 1$. The field strength is $3 \times 10^7 \text{ V/m}$ and the laser frequency is about $9 \times 10^{11} \text{ s}^{-1}$. The duration and center of the pulse are set equal to 279 fs and 1200 fs. The main feature is that the ratio in magnitude of the positive and negative peak value of this pulse is 5:1. Unless specified, the parameters of laser field are fixed throughout the paper.

Figure 5.2 illustrates the orientation $\langle \cos \theta \rangle$ as a function of time for different hindering angles and pulse durations. In both cases, the orientations display periodic-like behavior. For the pulse duration ($\sigma' = \sigma$), the orientation of small hindering angle ($\alpha = 60^\circ$) shows a relative large value but with small oscillatory amplitude, while for $\alpha = 120^\circ$ a large oscillatory amplitude with multi-frequency (insets of Fig. 5.2) is obtained. Obviously, such a difference comes from the quantum confinement effect. We further apply the laser pulses with different widths by tuning the duration and center. If the pulse duration increases, the amplitudes of the oscillations decrease and the orientations approach the initial value as shown in the insets. The reason is that the mean orientation is suppressed by the alternations of the electromagnetic field, i.e. the cancellation of negative and positive orientations.

To see more clearly the effect of hindering potential, let us now consider the

finite potential model

$$V_{hin}(\theta) = \begin{cases} 0, & 0 \leq \theta \leq \alpha \\ V_0, & \alpha < \theta \leq \pi \end{cases}, \quad (5.10)$$

where V_0 is the height of well. Following Refs. [4, 5], the rotational energy and eigenfunctions can be determined by matching appropriate boundary condition.

Figure 5.3 shows the time-averaged orientation as a function of time for different hindering potentials. For infinite potential ($V_0 = \infty$), the time-averaged orientation decreases monotonically from 1 to 0 as the hindering angle is increased. However, if the well is finite, the time-averaged orientation has a maximum point at certain angle. This means if the open angle α decreases further, the contribution from the penetrated wavefunction overwhelms the impenetrable one, rendering the decreasing of the time-averaged orientation. We also compare the case of $\sigma' = \sigma$ with that of $\sigma' = 5\sigma$ (inset of Fig. 5.3). It is found that, for larger duration $\sigma' = 5\sigma$, although the oscillatory amplitude is smaller (Fig. 5.2), the value of time-averaged orientation is larger comparing to the case of $\sigma' = \sigma$.

5.2 Two coupled adsorbed molecules in a strong laser pulse

As we mentioned above, the spatial resolution of two individual molecules hindered on a surface in tens of nanometers is now possible [29, 30, 31]. We further consider that two identical dipolar molecules (separated by a distance of R , R is in an order of magnitude of 10^{-8} m) confined by the hindering wells. The molecules are assumed to interact with each other via dipole-dipole interaction

only. A polarized laser pulse is applied to interact with both molecules. The Hamiltonian of the coupled system can be written as

$$H_c = \sum_{j=1,2} H_{0,j} + U_{dip} + H_I, \quad (5.11)$$

where $H_{0,j}$ is the Hamiltonian of single hindered rotor without the laser-dipole interaction. The dipole interaction between two dipole moments μ_1 and μ_2 is

$$\begin{aligned} U_{dip} &= [\vec{\mu}_1 \cdot \vec{\mu}_2 - 3(\vec{\mu}_1 \cdot \hat{e}_R)(\vec{\mu}_2 \cdot \hat{e}_R)]/R^3 \\ &= \mu_1 \mu_2 (\sin \theta_1 \cos \phi_1 \sin \theta_2 \cos \phi_2 + \cos \theta_1 \cos \theta_2 \\ &\quad - 2 \sin \theta_1 \sin \phi_1 \sin \theta_2 \sin \phi_2)/R^3 \end{aligned} \quad (5.12)$$

where $\hat{e}_R (= \vec{R}/R)$ is assumed to be in the y -direction, and (θ_1, ϕ_1) and (θ_2, ϕ_2) are the coordinates of first and second molecule respectively. For simplicity, we assume the dipole moments of two molecules are identical, i.e., $\mu_1 = \mu_2 = \mu_0$. One might argue that the higher order terms may also contribute to the results. According to previous study [27], the next higher order term is about the order of r^3/R^4 with bond length r . If one compares the dipole-dipole interaction, ($O(r^2/R^3)$), with the next higher order effect (the bond length $r = 2.7 \text{ \AA}$ [48] and separation $R = 15 \text{ nm}$), it is found that the contribution from the next higher-order term is only 2 percent of the dipole-dipole interaction. Therefore, it is reasonable to include only the dipole interaction in our model. The field-molecule coupling H_I can then be expressed as

$$H_I = -\mu_0 E(t) \cos \theta_1 \cos(\omega t) - \mu_0 E(t) \cos \theta_2 \cos(\omega t), \quad (5.13)$$

where θ_1 and θ_2 are the angles between dipole moments and laser field. In above equations, the time-dependent Schrödinger equation can be solved by expanding the wave function in terms of a series of eigenfunctions

$$\Psi_c = \sum_{l_1, m_1; l_2, m_2} c_{l_1, m_1; l_2, m_2}(t) \psi_{l_1, m_1}(\theta_1, \phi_1) \psi_{l_2, m_2}(\theta_2, \phi_2), \quad (5.14)$$

where (θ_1, ϕ_1) and (θ_2, ϕ_2) are the coordinates for two molecules. $c_{l_1, m_1; l_2, m_2}(t)$ are the time-dependent coefficients and can be determined by solving Schrödinger equations numerically. The initial state is set as $\psi_{0,0} \psi_{0,0}$ ($c_{0,0;0,0}(t=0) = 1$).

In addition to the orientation, one can also analyze the entanglement induced by the dipole interaction. Following the method in chapter 4, the wavefunction of the coupled molecules can be expressed as a pure bipartite system (a compact form of Eq. (5.14)): $|\Psi_c\rangle = \sum_{l_1, m_1; l_2, m_2} c_{l_1, m_1; l_2, m_2}(t) |\psi_{l_1, m_1}\rangle |\psi_{l_2, m_2}\rangle$. The reduced density operator for the first molecule is defined as

$$\rho_{\text{mol } 1} = \text{Tr}_{\text{mol } 2} |\Psi_c\rangle \langle \Psi_c|. \quad (5.15)$$

To obtain the entanglement of entropy, the bases of molecule 1 is transformed to make the reduced density matrix $\rho_{\text{mol } 1}$ to be diagonal. The entangled state can be represented by a biorthogonal expression with positive real coefficients $\lambda_{l,m}$. The degree of entanglement for the coupled molecules can be measured by von Neumann entropy [46, 47]

$$\text{Entropy} = - \sum_{l,m} \lambda_{l,m} \log_{\text{n}} \lambda_{l,m}. \quad (5.16)$$

Figure 5.4 shows the entropy and orientation evolves with time for fixed angle $\alpha = 120^\circ$ and inter-distance $R = 1.5 \times 10^{-8}$ m. Because of the presence of the laser pulse, contributions to the energy exchange between two molecules come from many excited states, resulting in an irregular-like behavior of the entropy shown in the Fig. 5.4(a). Further analysis of the dynamics gives the fact that the entropy grows monotonically from zero to certain finite value. This is because the laser pulse dominates at initial stage. The strength of laser pulse is much larger than that of dipole-dipole interaction. In addition, the duration is much shorter than the characteristic time of the dipole interaction. After the laser pulse, populations to the (rotational) excited states are formed (inset). The non-linear dipole interaction then initiates the exchange process between the states until certain "dynamical equilibrium" is reached. One can conclude that the nonlinear variations of populations confirm the feature shown in the inset. Moreover, the orientations of the coupled molecules are also displayed in Fig. 5.4(b). Comparing to the single molecule case, the irregular behavior is certainly from the non-linear dipole interaction.

Figure 5.5 shows the time-averaged entropy for different hindering angles. As the hindering angle increases, the time-averaged entropy increases monotonically. This is because for larger angles more excited states can be obtained under the same strength of the laser pulse, resulting in larger entropy. Notes that the magnitude of orientation is high as the hindering angle is set equal to 30° (inset of Fig.

5.5). This again verifies that narrow potential restricts the motion of the hindered rotor. In this case, the dipole interaction is suppressed, causing the regular-like behavior of the orientation. On the contrary, more excitations are populated such that the orientation oscillates with irregularity at $\alpha = 150^\circ$.

A few remarks about the experimental verifications of our model should be addressed here. According to the results in chapter 4 and 5, it is found that the orientations of the coupled rotors relate closely to the entropy. This indicates that the orientations of coupled rotors somehow reflect the entropy of the system. For the measurement of orientations, many experiments have been performed. For example, the Coulomb explosion of the molecules using intense femtosecond probe laser pulses and a time-of-flight mass spectrometer [49, 50, 51]. The degree of orientation is determined by the measurement of fragment ions. Under proper arrangements, the orientations of hindered rotors can also be measured by the similar technologies. This may provide some indication of the entanglement.

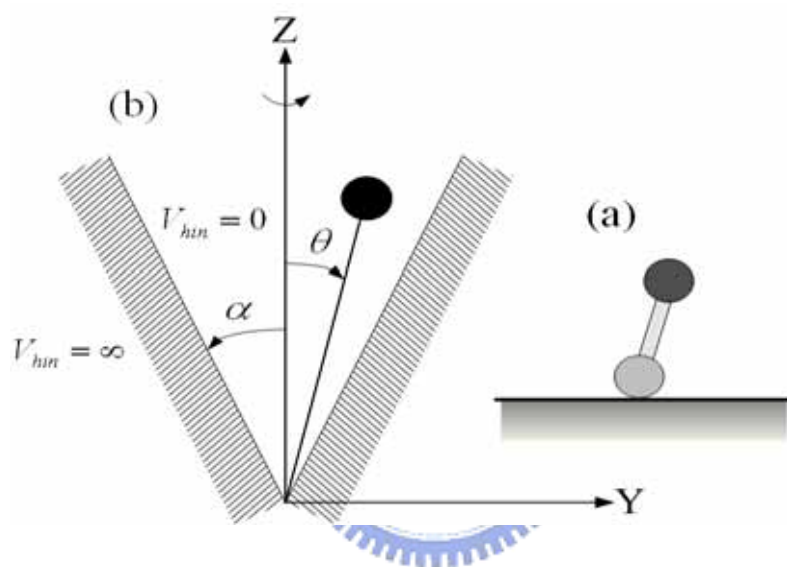


Figure 5.1: (a) Schematic view of single hindered rotor adsorbed on the surface.
 (b) The corresponding infinite-conical-well model.

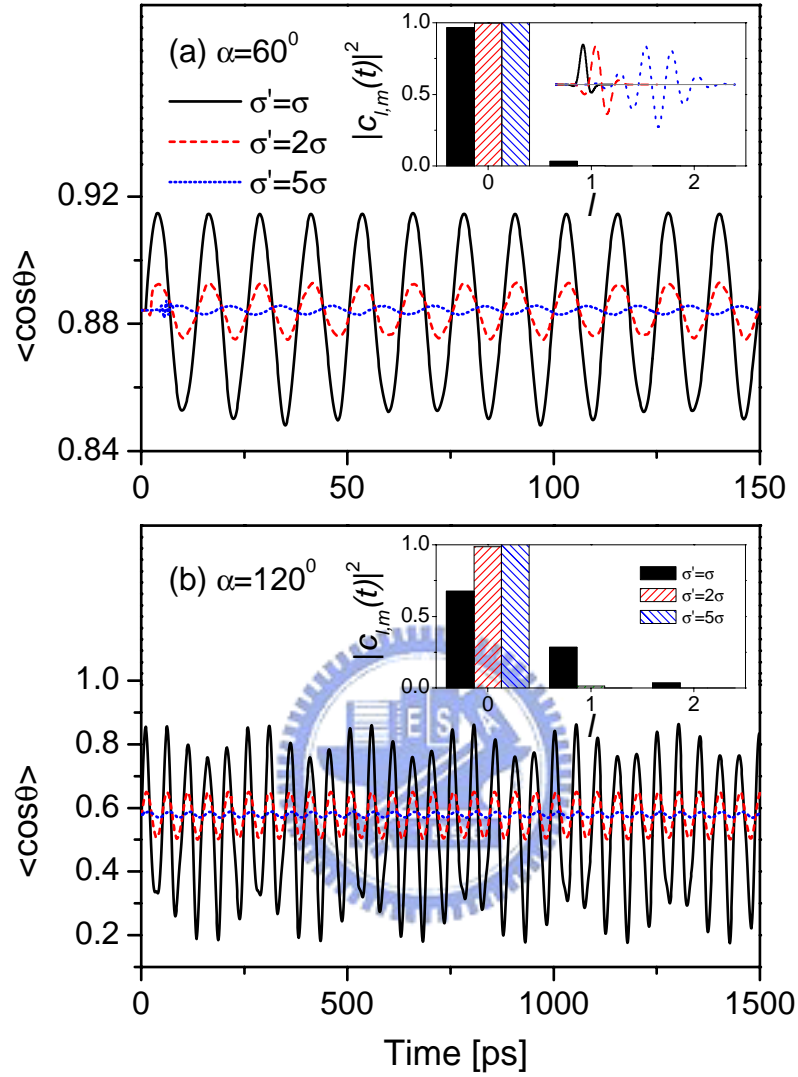


Figure 5.2: The orientation $\langle \cos\theta \rangle$ as a function of time for different hindering angle α and pulse duration σ' . The insets show the corresponding populations of the states $(l, m = 0)$ for (a) $\alpha = 60^\circ$ and (b) $\alpha = 120^\circ$ respectively. The corresponding laser fields are shown in the upper inset.

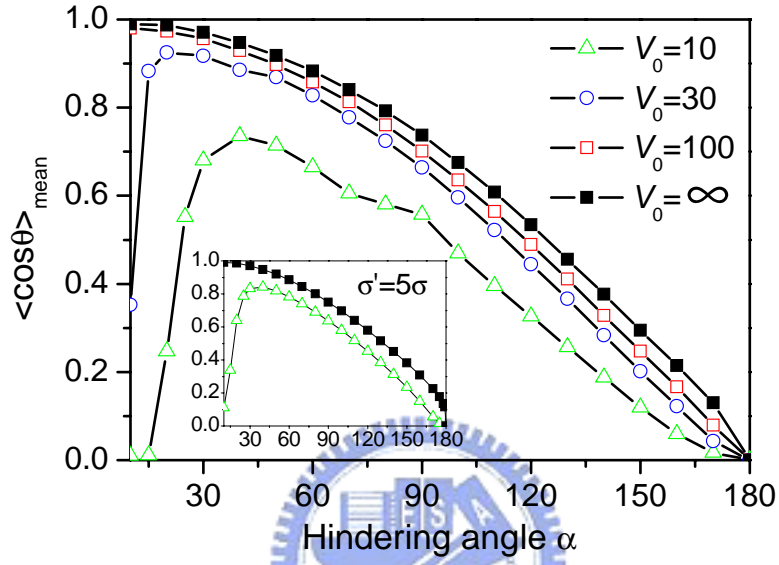


Figure 5.3: The mean orientation $\langle \cos \theta \rangle_{\text{mean}}$ as a function of hindering angle for fixed pulse duration ($\sigma' = \sigma$) and different conical-well potentials $V_0 = 10, 30, 100$. The inset shows the mean orientation $\langle \cos \theta \rangle_{\text{mean}}$ in the case of $V_0 = 10$ and ∞ by applying a pulse of $\sigma' = 5\sigma$. The potential V_0 is in units of the rotational constant B .

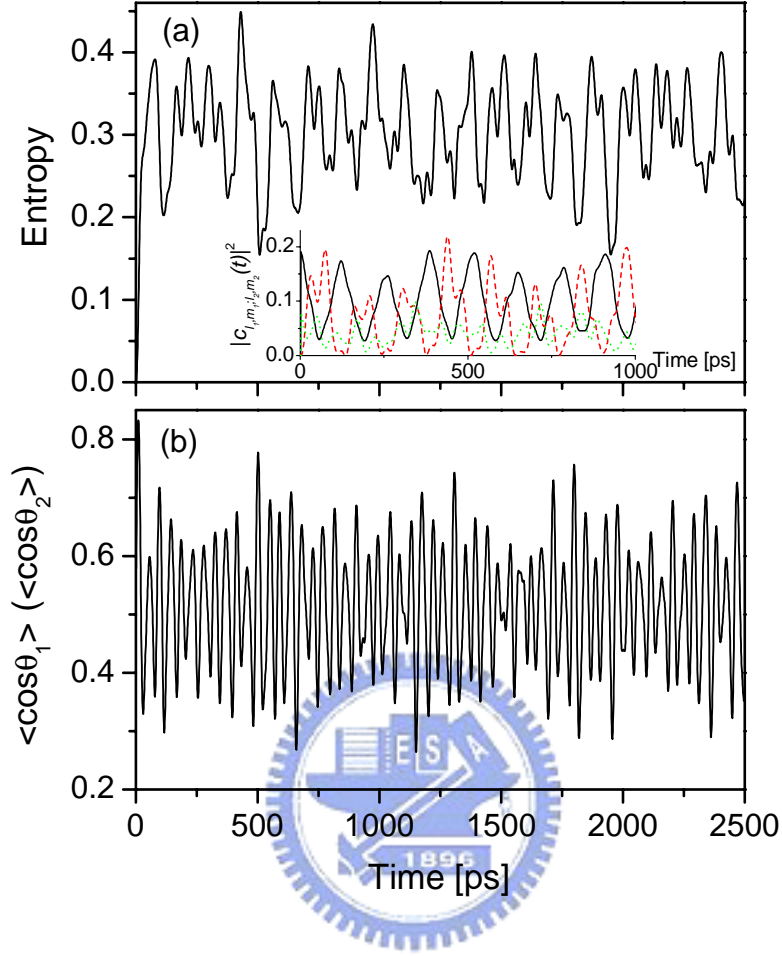


Figure 5.4: The entropy (a) and orientations $\langle \cos \theta_1 \rangle$ ($\langle \cos \theta_2 \rangle$) (b) in infinite conical-well for fixed angle $\alpha = 120^\circ$ and inter-distance $R = 1.5 \times 10^{-8}$ m. The inset shows the populations ($|c_{l_1, m_1; l_2, m_2}(t)|^2$) irregularly oscillate with time, corresponding to the quantum number $(l_1, m_1; l_2, m_2) = (1, 0; 0, 0)$ (black solid curve), $(1, 1; 0, 0)$ (red dashed curve), and $(1, 0; 1, 0)$ (green dotted curve) respectively. Although we only focus on several excited states here, the populations of most states similarly remain irregular behavior.

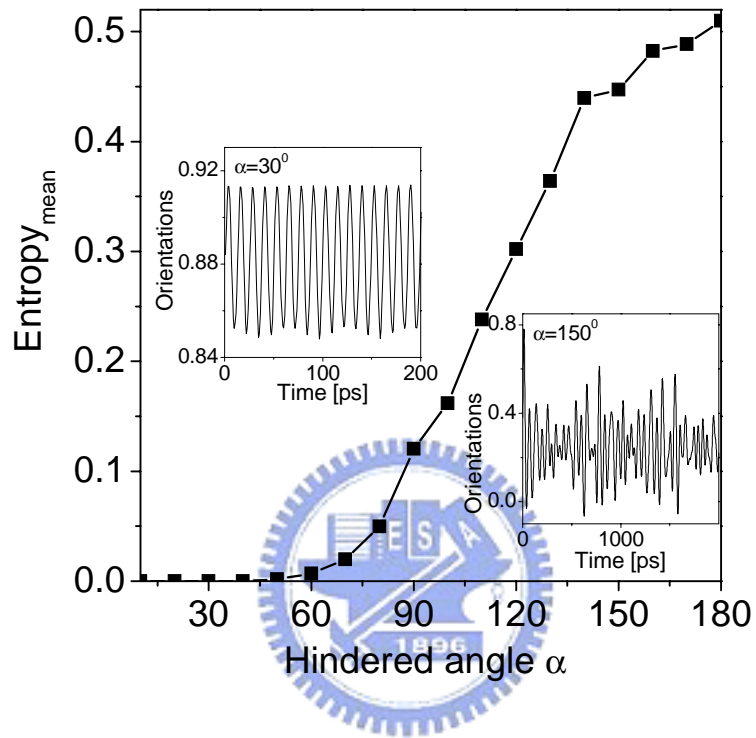


Figure 5.5: The time-averaged entropy as a function of the hindered angle in infinite conical-well. The insets show the orientations of two molecules for hindered angles $\alpha = 30^\circ$ and $\alpha = 150^\circ$ respectively. The inter-molecule separation is $R = 1.5 \times 10^{-8}$ m.

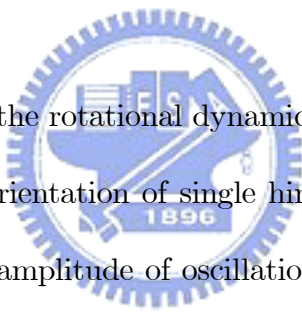
CHAPTER 6

SUMMARY AND FUTURE WORK

In this part of the thesis we have studied the rotational motion of a polar diatomic molecule, which is confined by a hindering conical-well. It is shown that an ultrashort laser pulse can induce alignment and orientation of a hindered molecule. The hindered angle of the hindered potential well plays a key role on the molecular alignment and orientation. Crossover from field-free rotation to a hindered one can be observed by varying the hindered angle of the potential well. At small hindered angle, both alignment and orientation show sinusoidal-like behavior because of the suppression of higher excited states. However, mean orientation decreases monotonically as the hindered angle is increased, while mean alignment displays a minimum point at certain hindered angle. The reason is attributed to the symmetry of wavefunction and can be explained well by analyzing the coefficients of eigenstates.

As for coupled free rotors system, we have studied the orientations and entanglement of two coupled polar molecules irradiated by strong laser pulses. The behavior of the orientations is different from that of a free one. By varying the period of a series of periodically applied laser pulse, transition from regular to chaotic-like behavior may occur. To characterize the degree of entanglement, the

von Neumann entropy is calculated. It is shown that the entanglement can be enhanced by increasing the strength of laser pulse or applying multi pulse. Further, periodic-like entropy is found as a symmetrical-ratio pulse is shined, while a highly asymmetrical pulse can induce highly irregular entropy. We also discussed the difference between the quantum and classical regime in this coupled-rotor system. By varying the Planck constant, crossover from quantum to classical limit can be seen from the von Neumann entropy. Prominent difference in entropy between quantum and classical regime is the time that approaches dynamical equilibrium. In particular, for classical limit, the system is expected to need infinite time for dynamical equilibrium.



We have further studied the rotational dynamics of the adsorbed polar molecules. It is found that the orientation of single hindered rotor shows a periodic behavior. In particular, the amplitude of oscillation is sensitive to the degree of alternation of the laser field. Crossover from field-free to hindered rotation is observed by varying the hindering angle for different heights of conical-wells. On the other hand, the orientations of coupled rotors show irregular behavior because of the dipole-dipole interaction. Entanglement induced by the dipolar interaction is also calculated for the coupled-rotor system, in which the time-averaged entropy increases monotonically as the hindering angle is increased. The competition between the confinement effect and dipole interaction is found to dominate the behavior of the coupled-rotor system.

Based on the results, some works can be continued in the future: the quantum control of the rotational states. With the advances of laser technologies [52], molecular dynamics can be controlled by applying the optimal control theory. The optimal control investigation of a laser driven system can be viewed as a problem of state-to-state control. The purpose is to calculate the shape of the laser pulse which induces the maximum transfer of probability from the given initial state to a chosen final state. Although the optimal control theory is extensively applied to the recent works such as chemical reaction, to our best knowledge, the study on adsorbed-molecule system still receives little attention. Therefore, steering a quantum system of molecules adsorbed on the surface is believed to be important in surface processes and reactions.



CHAPTER 7

INTRODUCTION TO PART II

In the last two decades, nano-technologies have made it possible to fabricate quantum dots with the dimensions at nanoscale. Quantum dot may be a good choice for quantum electronics due to its zero dimensionality, quantized energy levels, and long coherence times of spin states [53, 54]. Figure 7.1 (a) illustrates a lateral quantum dot with six metal gates patterned on the surface of a two-dimensional electron gas (2DEG) [55]. When a strong negative gate voltage is applied to the gates, a small island for electrons, the quantum dot, is isolated in the depleted region within the 2DEG. By operating and modifying the gate voltages, the electron tunneling and the number of electrons confined in the dot can be controlled. On the other hand, the structure of a vertical quantum dot is shown in Fig. 7.1 (b). A quantum dot is fabricated in the center of the pillar and sandwiched between two thin non-conducting barriers. To control the number of electrons, the effective diameter of the dot can be squeezed through a negative voltage applied to the side gate.

To well operate quantum electronics, keeping the spin state unchanged is an important issue. In general, the spin-orbit coupling, which is one of the main causes of spin relaxation is a relevant intrinsic interaction in nonmagnetic semi-

conductors. It is known that there are two different types of spin-orbit coupling as quantum dots are fabricated within semiconductors of a zincblende structure. The first one is the Dresselhaus interaction, which is due to the bulk inversion asymmetry of the lattice [56, 57, 58]. The polar bonds can cause electric fields between the atoms and lead to spin orbit coupling in zincblende materials. The second is the Rashba interaction caused by the structure inversion asymmetry [59, 60]. The spin-orbit couplings mix the spin states with different orientations in the Zeeman sublevels [61, 62, 63] and therefore make spin relaxation possible in the presence of the electron-phonon interaction [64, 65, 66, 67, 68].

Electron-phonon interaction in electron transport has long been an important topic [69, 70]. The emission of phonons was observed in transport experiments of double quantum dots embedded in bulk materials [69]. With the advance of nanotechnologies, free-standing structures can now be fabricated. Due to the interplay between the electrical and mechanical degrees of freedom, the electron transport through the quantum dots is influenced under the environment of nanomechanical vibrations. In contrast to the bulk material phonons, phonons of nanomechanical vibrations are no longer mere a source of dissipation. The phonon spectrum in the structures is split into discrete subbands, and the quantization effects contribute greatly to the thermal conductivity [71, 72, 73]. Because of the boundary conditions for the vibrational modes, the phonon-dispersion shows some singular properties, such as the van Hove singularities. A 2DEG quantum dot embedded

in a suspended phonon cavity has been fabricated in a recent experimental work [74, 75]. Single electron tunneling around zero bias showed a complete suppression in the transport spectrum which is believed to be due to the excitation of a localized phonon mode confined in the cavity leading to the formation of an energy gap. This opens possible avenues to investigate the ultimate limit of single electrons interacting with individual phonon modes.

In addition, it is known that the electronic and optical properties in quantum devices are sensitive to the features of the quantum dots, which can be controlled and operated through the flexible features [76, 77]. Recently, quantum dot systems in the presence of time-varying external fields manifest some interesting effects ranging from photon-assisted tunneling [78] to electron pumping [79]. In a recent experiment, the transport spectroscopy has been measured in coupled double quantum dots under microwave fields [78]. The photon-assisted resonances are found by a modulated gate voltage. The phenomenon involves the emission or absorption of a microwave photon. For electron pumping, an open quantum dot system without the voltage bias across it has been reported [79]. Because of the presence of time-varying parameters, the confining potential in the quantum dot can be influenced in the adiabatic regime. This results in an electric current flowing through the quantum dot.

In this part we present the studies on spin relaxation and electron transport in quantum dot systems. As a quantum dot is embedded inside a free-standing

structure, a significant spin relaxation rate is found due to the confined phonons. To study electron transport through a nano-system, a double-dot device embedded in a single phonon environment is further discussed. The effects of Coulomb and phonon fields can reflect the behavior of the transport. Furthermore, it is also shown that the transport of the quantum device is influenced by the irradiation of the external field.

This part is organized as follows. We investigate the phonon-induced spin relaxation in a quantum dot embedded inside a semiconductor slab in chapter 8. The behavior of the scattering rates is examined under various conditions. In chapter 9, electron transport through a double-dot device embedded in a single phonon environment is studied. The effects of Coulomb and phonon fields on the conductance are also discussed. Besides, we also consider the electron tunneling through a three-level system in an asymmetric double-dot device in chapter 10. Irradiating by an external field, a significant behavior in the current spectrum is discussed. Finally, we conclude our results and present future works in chapter 11.

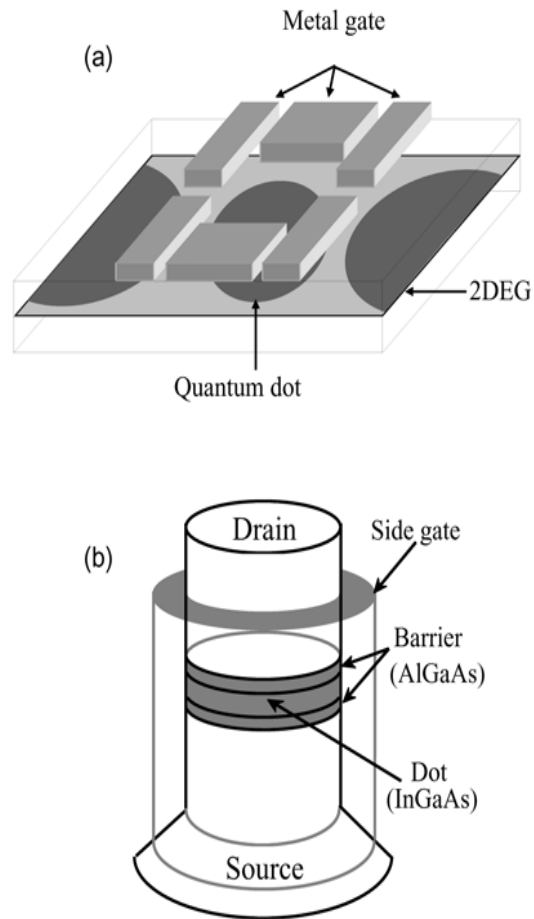


Figure 7.1: Schematic views of a lateral (a) and vertical (b) quantum dots. From Ref. [55].

CHAPTER 8

SPIN RELAXATION IN A GAAS QUANTUM DOT EMBEDDED INSIDE A SUSPENDED PHONON CAVITY

The quantum dot may be a good choice for quantum electronics due to its zero dimensionality, quantized energy levels, and long coherence times of spin states [53, 54]. For example, the spin of an electron confined to a quantum dot can form a qubit [80, 81]. However, some scattering processes will cause the change of the spin states. One important process is related to the phonon-induced spin-flip resulting from the spin-orbit interaction. This affects the time of spin purity in the quantum dot. In order to keep the information unchanged, a long relaxation time is required.

In general, the spin-orbit coupling, which is one of the main causes of spin relaxation, is a relevant intrinsic interaction in nonmagnetic semiconductors. It is known that there are two different types of spin-orbit coupling as quantum dots are fabricated within semiconductors of a zincblende structure. The first one is the Dresselhaus interaction, which is due to the bulk inversion asymmetry of the lattice [56, 57, 58]. The second is the Rashba interaction caused by the structure

inversion asymmetry [59, 60]. The spin-orbit couplings mix the spin states with different orientations in the Zeeman sublevels [61, 62, 63] and therefore make spin relaxation possible in the presence of the electron-phonon interaction.

Relaxation times of electron spins in a quantum dot have been measured by electrical pump-probe experiments [82]. The triplet-to-singlet transition with emission of phonons was found with corresponding spin relaxation times of about 200 μs . Recently, the spin relaxation time in a one-electron GaAs quantum dot was measured by a similar electrical pump-probe technique [83, 84]. As the magnetic field was applied parallel to the two-dimensional electron gas, the Zeeman splitting of quantum dot was observed in dc transport spectroscopy. By monitoring the relaxation of the spin, the relaxation time was found to have a lower bound of 50 μs at an in-plane field of 7.5 T [83].

On the theoretical side, spin relaxation between two spin-orbital mixed states in semiconductor quantum dots has been studied recently. However, to the best of our knowledge, all previous studies of spin relaxation concentrated on quantum dots embedded in the bulk material, [64, 65, 66, 67, 68] whereas studies of spin relaxation induced by confined phonons are still lacking. We therefore consider a single quantum dot embedded inside a free-standing structure (semiconductor slab), where the relevant characteristic is the two-dimensional phonon wavevector for the acoustic-phonon spectrum as shown in Fig. 8.1 [74, 75, 85, 86, 87]. Since the reduced dimension will enhance the deformation potential, we will mainly

focus on the spin relaxation rate induced by the deformation potential [86, 87]. In this chapter we consider the parabolic quantum dot model with spin-orbit interaction. Energy spectra of the quantum dot can be solved by using an exact diagonalization method. We then apply the Fermi golden rule to calculate spin relaxation rates for typical parameters. We discuss the dependence of the spin relaxation rates on the size of the quantum dot, the phonon bath temperature, and the width of the slab.

8.1 Model

8.1.1 Single particle in a quantum dot

We consider an isotropic quantum dot with an in-plane parabolic lateral confinement potential. An external magnetic field B is applied perpendicularly to the surface of the quantum dot as shown in Fig. 8.1(a). The electronic Hamiltonian of this system can be written as

$$H_e = H_0 + H_{so}. \quad (8.1)$$

The first term describes the electron Hamiltonian without the spin-orbit coupling,

$$H_0 = \frac{\mathbf{P}^2}{2m^*} + \frac{1}{2}m^*\omega_0^2r^2 + \frac{1}{2}g^*\mu_B B\sigma_z, \quad (8.2)$$

where $\mathbf{P} = -i\hbar\nabla + (e/c)\mathbf{A}$ is the kinetic momentum with vector potential $\mathbf{A} = (B/2)(-y, x, 0)$ confined to the 2D plane. Here m^* is the effective electron mass, e is the electron charge, c is the velocity of light, ω_0 is the characteristic confined

frequency, g^* is the bulk g -factor, μ_B is the Bohr magneton, and σ_z is a Pauli matrix.

The Rashba and Dresselhaus interactions ($H_{so} = H_R + H_D$) are given by

$$H_R = \frac{\lambda_R}{\hbar}(\sigma_x P_y - \sigma_y P_x), \quad (8.3)$$

$$H_D = \frac{\lambda_D}{\hbar}(-\sigma_x P_x + \sigma_y P_y). \quad (8.4)$$

The coupling constants λ_R and λ_D determine the spin-orbit strengths, which depend on the band-structure parameters of the material. Besides, the Rashba and Dresselhaus terms are also associated to the perpendicular confinement field and the confinement width in the z -direction, respectively.

For the electron Hamiltonian H_0 , the well-known Fock-Darwin states can be easily obtained from

$$\Psi_{n,l,\sigma} = \frac{\sqrt{2}}{r_0} \left[\frac{n!}{(n+|l|)!} \right]^{\frac{1}{2}} \exp\left(-\frac{r^2}{2r_0^2}\right) \left(\frac{r^2}{r_0^2}\right)^{\frac{|l|}{2}} L_n^{|l|}\left(\frac{r^2}{r_0^2}\right) \frac{e^{il\theta}}{\sqrt{2\pi}} \chi_\sigma, \quad (8.5)$$

with $r_0 = (\hbar/m\Omega)^{\frac{1}{2}}$. χ_σ represents the eigenfunction of σ_z and $L_n^{|l|}$ is the generalized Laguerre polynomial given by the formula

$$L_n^{|l|}(z) = \sum_{m=0}^n \frac{(-1)^m}{m!} \binom{n+|l|}{n-m} z^m. \quad (8.6)$$

The electron energy levels are

$$E_{n,l,\sigma} = \hbar\Omega(2n + |l| + 1) + \hbar\omega_B l/2 + \sigma E_B, \quad (8.7)$$

where n ($= 0, 1, 2, \dots$) and l ($= 0, \pm 1, \pm 2, \dots$) are the quantum numbers. The renormalized frequency is $\Omega = \sqrt{\omega_0^2 + \omega_B^2/4}$, with the cyclotron frequency $\omega_B = eB/m^*$

and the characteristic confinement frequency ω_0 limited by the effective quantum dot lateral length $l_0 = \sqrt{\hbar/m^*\omega_0}$. Here, $E_B = g\mu_B B/2$ is the Zeeman splitting energy, and $\sigma = \pm 1$ refers to the electron-spin polarization along the z axis. To solve the Schrödinger equation with ($H_e = H_0 + H_{so}$), the (spin mixing) wave function is expressed in terms of a series of eigenfunctions: $\Psi_\ell(r, \theta) = \sum c_{n,l,\sigma} \Psi_{n,l,\sigma}$ for each state ℓ . After exactly diagonalizing the electron Hamiltonian, the corresponding eigenvalues E_ℓ and the coefficient $c_{n,l,\sigma}$ can be obtained numerically.

8.1.2 Confined phonon in a semiconductor slab

Before calculating the spin relaxation rate, the confined phonon in the free-standing structure must be introduced here. Following Refs. [85, 86], we consider an infinite film with width a (Fig. 8.1). For the effect of the contact with the semiconductor substrate, we neglect the distortion of the acoustic vibrations. Under this consideration, one can ensure that the in-plane wavelength can be shorter than the characteristic in-plane size of the solid slab. For simplicity, the elastic properties of the slab are isotropic. Small elastic vibrations of a solid slab can then be defined by a vector of relative displacement $\mathbf{u}(\mathbf{r}, t)$. Under the isotropic elastic continuum approximation, the displacement field \mathbf{u} obeys the equation

$$\frac{\partial^2 \mathbf{u}}{\partial t^2} = c_t^2 \nabla^2 \mathbf{u} + (c_l^2 - c_t^2) \nabla (\nabla \cdot \mathbf{u}), \quad (8.8)$$

where c_l and c_t are the velocities of longitudinal and transverse bulk acoustic waves. To define a system of confined modes, Eq. (8.8) should be complemented

by the boundary conditions at the slab surface $z = \pm a/2$. Because of the confinement, phonons will be quantized in subbands. For each in-plane component q_{\parallel} of the in-plane wave vector there are infinitely many subbands. Since two types of velocities of sound exist in the elastic medium, there are also two transversal wavevectors q_l and q_t . In the following, we consider the deformation potential only. This means there are two confined acoustic modes: dilatational waves and flexural waves contribute, but shear waves are neglected because of their vanishing interaction with the electrons for spin relaxation.

For dilatational waves, the parameters $q_{l,n}$ and $q_{t,n}$ can be determined from the Rayleigh-Lamb equation

$$\frac{\tan(q_{t,n}a/2)}{\tan(q_{l,n}a/2)} = \frac{4q_{\parallel}q_{l,n}q_{t,n}}{(q_{\parallel}^2 - q_{t,n}^2)^2}, \quad (8.9)$$

with the dispersion relation

$$\omega_{n,q_{\parallel}} = c_l^2 \sqrt{q_{\parallel}^2 + q_{l,n}^2} = c_t^2 \sqrt{q_{\parallel}^2 + q_{t,n}^2}, \quad (8.10)$$

where $\omega_{n,q_{\parallel}}$ is the frequency of the dilatational wave in mode (n, q_{\parallel}) . For the antisymmetric flexural waves, the solutions $q_{l,n}$ and $q_{t,n}$ also can be determined by solving the equation

$$\frac{\tan(q_{l,n}a/2)}{\tan(q_{t,n}a/2)} = -\frac{4q_{\parallel}q_{l,n}q_{t,n}}{(q_{\parallel}^2 - q_{t,n}^2)^2}, \quad (8.11)$$

together with the dispersion relation, Eq. (8.10).

8.1.3 Electron-phonon coupling and scattering rate

The electron-phonon interaction through the deformation is given by $H_{ep} = E_a \text{div} \mathbf{u}$, where E_a is the deformation-potential coupling constant. The Hamiltonian can be written as

$$H_{ep} = \sum_{\substack{\mathbf{q}_{\parallel}, n \\ \lambda=d, f}} M_{\lambda}(\mathbf{q}_{\parallel}, n, z)(a_{\mathbf{q}_{\parallel}}^{\dagger} + a_{\mathbf{q}_{\parallel}}) \exp(i\mathbf{q}_{\parallel} \cdot \mathbf{r}_{\parallel}), \quad (8.12)$$

where \mathbf{r}_{\parallel} is the coordinate vector in the x - y plane and the functions M_d and M_f describe the intensity of the electron interactions with the dilatational and flexural waves, and are given by

$$M_d(q_{\parallel}, n, z) = F_{d,n} \sqrt{\frac{\hbar E_a^2}{2A\rho\omega_{n,q_{\parallel}}}} (q_{l,n}^2 - q_{\parallel}^2)(q_{l,n}^2 + q_{\parallel}^2) \sin\left(\frac{aq_{l,n}}{2}\right) \cos(q_{l,n}z), \quad (8.13)$$

$$M_f(q_{\parallel}, n, z) = F_{f,n} \sqrt{\frac{\hbar E_a^2}{2A\rho\omega_{n,q_{\parallel}}}} (q_{l,n}^2 - q_{\parallel}^2)(q_{l,n}^2 + q_{\parallel}^2) \cos\left(\frac{aq_{l,n}}{2}\right) \sin(q_{l,n}z), \quad (8.14)$$

where A is the area of the slab, ρ is the mass density, and $F_{d,n}$ ($F_{f,n}$) is the the normalization constants of the n -th eigenmode for the dilatational (flexural) waves. Although the fluctuation of the dot (due to strain etc.) may affect the spin-orbit and electron-phonon coupling, we, for simplicity, neglect the effect on the scattering rate in this work.

We calculate the spin relaxation rates between the two lowest (spin mixing) states from the Fermi golden rule [88]

$$\Gamma = \frac{2\pi}{\hbar} \sum_{\substack{\mathbf{q}_{\parallel}, n \\ \lambda=d, f}} |M_{\lambda}|^2 |\langle f | e^{i\mathbf{q}_{\parallel} \cdot \mathbf{r}_{\parallel}} | i \rangle|^2 (N_{q_{\parallel}} + 1) \delta(\Delta E - \hbar\omega_{n,q_{\parallel}}), \quad (8.15)$$

where the energy $\Delta E (= E_i - E_f)$ is the energy difference between the first excited $|i\rangle$ and ground $|f\rangle$ states. The energy spectrum for the case of the lateral length $l_0 = 30$ nm is also shown in Fig. 8.2. $N_{q_{\parallel}}$ represents the Bose distribution of the phonon at temperature T . For the sake of simplicity, we consider the quantum dot to be located at $z = 0$ so that the function M_f for flexural waves plays no role.

8.2 Results and discussion

Let us first focus on the dependence of the relaxation rates on the magnetic field B for lateral length $l_0 = 30$ nm. Unlike the situation in bulk system, an enhanced spin relaxation rate occurs as shown in Fig. 8.3(a) (arrow 1 in the upper inset). This phenomenon originates from the van Hove singularity that corresponds to a minimum in the dispersion relation $\omega_{n,q_{\parallel}}$ for finite q_{\parallel} . We further plot the phonon group velocity ($\partial\omega_{n,q_{\parallel}}/\partial q_{\parallel}$) as a function of q_{\parallel} around the van Hove singularity as shown in Fig. 8.3(b). There are three modes contributing to the relaxation rate. In particular, a crossover from positive to negative group velocity is observed for one mode. Because of the zero phonon group velocity, the rate behaves sharply at that magnetic field. However in a real system the van Hove singularity would be cut off or broadened because of the finite phonon lifetime. Contrary to the enhanced rate, we find a suppression of the spin relaxation rate (arrow 2) at small magnetic field (also seen in the lower inset). This comes from a

vanishing divergence of the displacement field \mathbf{u} . As can be seen from Eq. (8.13) in detail, the deformation potential disappears at the condition of $q_{\parallel} = q_t$ (Fig. 8.3(c)), which causes a zero spin relaxation rate. Note that our results for the van Hove singularity and the disappearance of the deformation potential are consistent with what was found in Ref. [87]. Although the phonon model in our work is the same, the dot part is different.

The relaxation rate for larger quantum dots exhibits a qualitatively different behavior. As shown in Fig. 8.4, two van Hove singularities appear when varying the magnetic field. Besides, one also finds two suppressions of the relaxation rate (arrow) near the singularities. We have analyzed the energy spacing between the two lowest states in the inset of Fig. 8.4. For small lateral size, the gap increases monotonically (dashed line). On the contrary, energy spacing for larger quantum dots shows a quite different feature. The value initially increases as B increases. However, after it reaches a maximum point, the energy spacing decreases with the increasing of the magnetic field B : although the Zeeman splitting increases with increasing magnetic field, the spin-orbit interaction, on the contrary, tends to reduce the energy spacing between the two lowest levels. When the magnetic field is large enough, the spin-orbit effect overwhelms the Zeeman term and results in a decreasing tendency. Therefore, if the magnetic field is increased high enough, the dashed line (small quantum dot) also shows similar behavior. This agrees well with the findings in Ref. [63]. From the inset, one recognizes that if the

energy spacing exactly matches the specific phonon energy (dotted line), the van Hove singularity will appear. For the case of a large lateral length, there are two van Hove singularities and two suppressions of the relaxation rate (dashed-dotted line).

In addition to the size of the dot that affects the spin relaxation rate, the dependence of the relaxation rates on the magnetic field B for different temperatures is shown in Fig. 8.5. For higher temperature, the rate is larger than that for lower temperature. This is because as the temperature increases, the phonon distribution $N_{q_{\parallel}}$ becomes larger. This enhances the electron-phonon scattering and leads to a larger transition probability between the two levels.

Figure 8.6 shows the specific energy spacings where rates are enhanced and suppressed as a function of the width. For the case of small widths, the enhanced rates (black mark) and suppressed rates (red mark) can be clearly distinguished, and their corresponding energy spacings are relative large. With the increasing of the width, the energy spacing between the enhanced and suppressed rates decrease monotonically. One can expect that if the width increases further, the system will approach the bulk system. This means that the van Hove singularity and the suppressed rate will be inhibited and eventually disappear.

If one varies the vertical position of the dot, the rate will change due to different contributions from the dilatational and flexural waves. Accordingly, the van Hove singularities resulting from flexural waves will also be altered. For

example, the ratio of dilatational to flexural wave's contribution is about 2.8:1 under the condition of $B = 1$ T and vertical position $z = 25$ nm. However, if ΔE also changes, the contributions from two waves will also change. This is because the parameters $(q_{\parallel}, q_{l,n}, q_{t,n})$ of dilatational and flexural waves independently satisfy the dispersion relations. On the other hand, comparing the bulk phonons with the confined ones, the phonon-induced rates are roughly similar when varying the magnetic field. However, there are two peculiar characteristics for the confined phonons. One feature is the van Hove singularity which results from a zero group velocity such that an enhanced spin relaxation rate can occur. The second feature is a vanishing divergence of the displacement field. This will cause a suppression of spin relaxation rate, which is an advantage if considering the quantum dot spin as a possible quantum bit candidate.



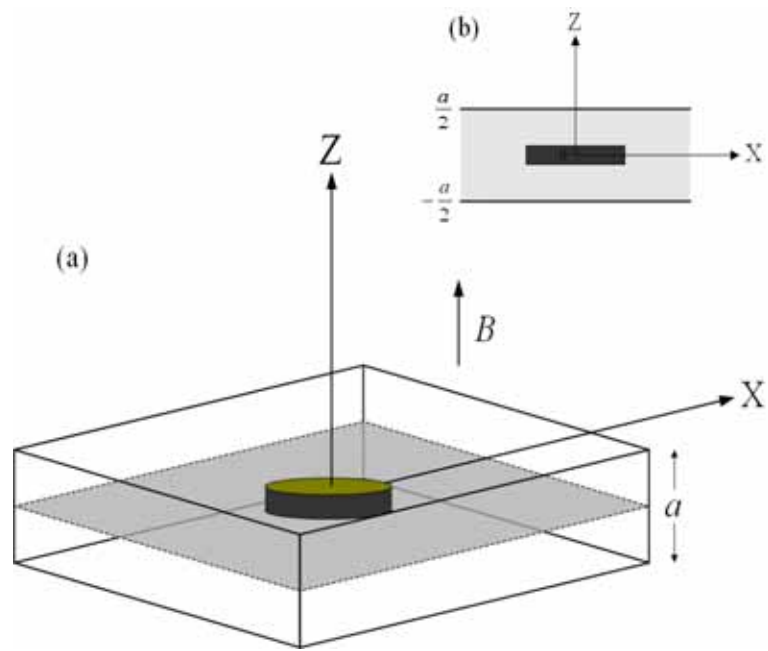


Figure 8.1: (a) Schematic view of single quantum dot embedded in the semiconductor slab with a width of a . (b) The side view shows a quantum dot is located at $z = 0$.

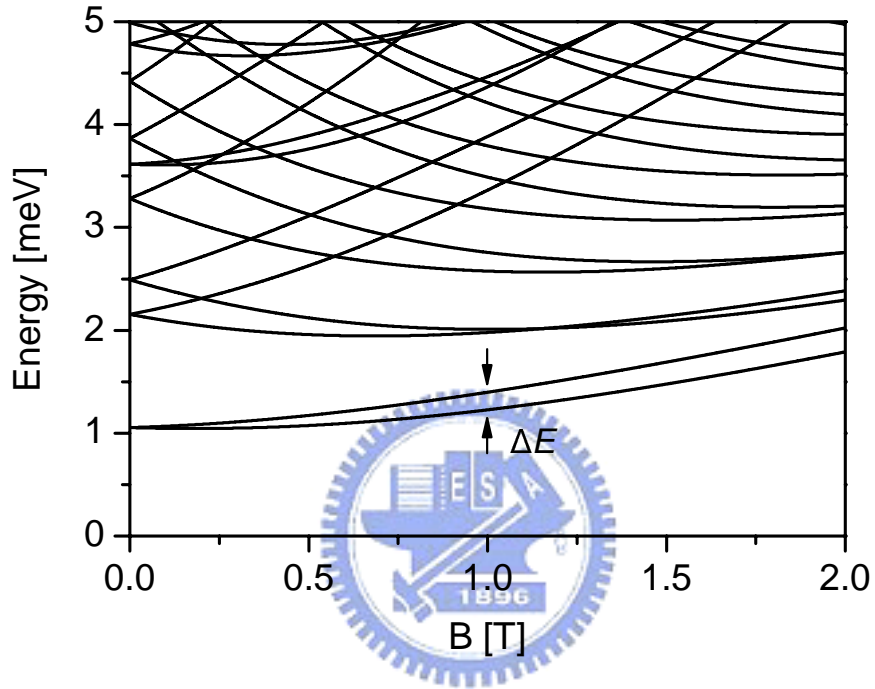


Figure 8.2: Energy spectrum for GaAs quantum dot versus the applied magnetic field for the lateral length $l_0 = 30$ nm. The spin-orbit couplings λ_R and λ_D are set equal to 5×10^{-13} and 16×10^{-12} eV m, respectively.

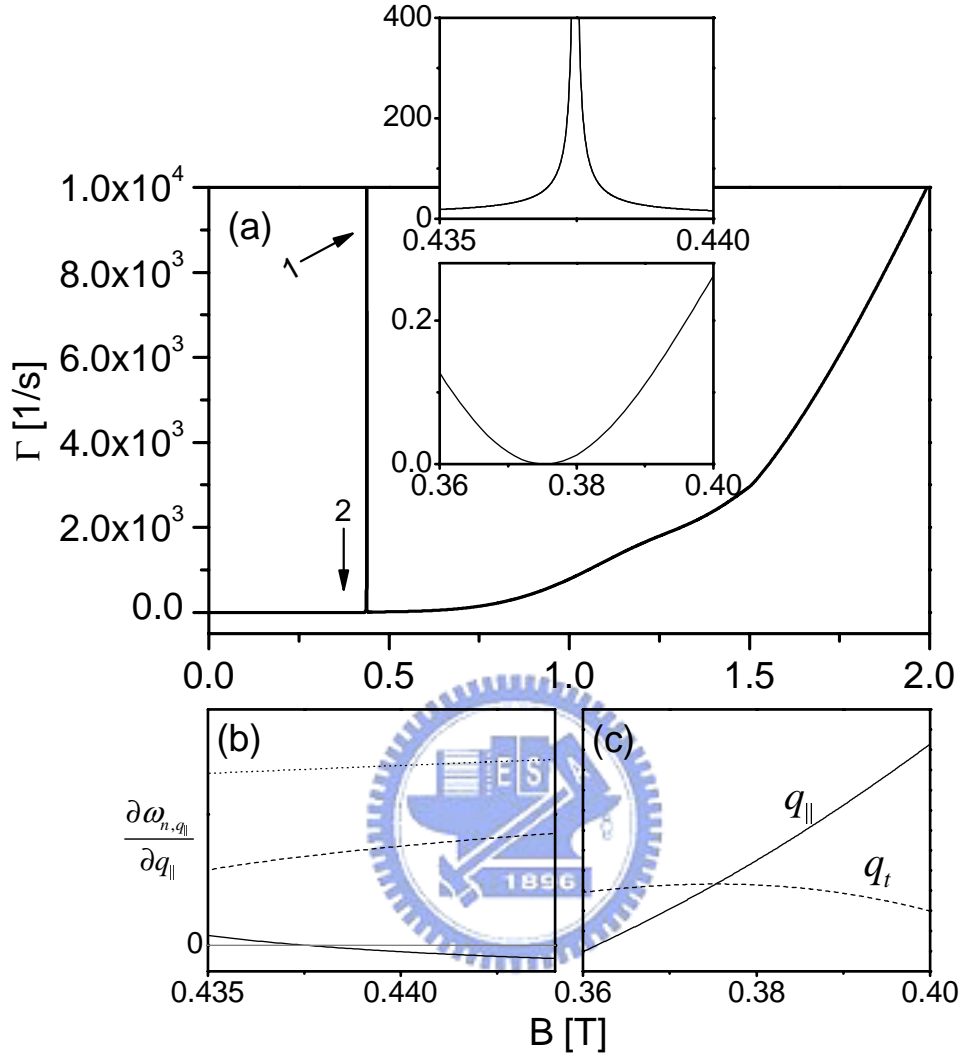


Figure 8.3: (a) Spin relaxation rate as a function of magnetic field for the lateral length $l_0 = 30$ nm, the width $a = 130$ nm, and temperature $T=100$ mK. The spin-orbit couplings λ_R and λ_D are set equal to 5×10^{-13} and 16×10^{-12} eV m, respectively. The insets further show the enlarged regions of arrow 1 (upper inset) and arrow 2 (lower inset). (b) Three phonon group velocities vs the magnetic field. (c) The values $q_{||}$ and q_t vs the magnetic field.

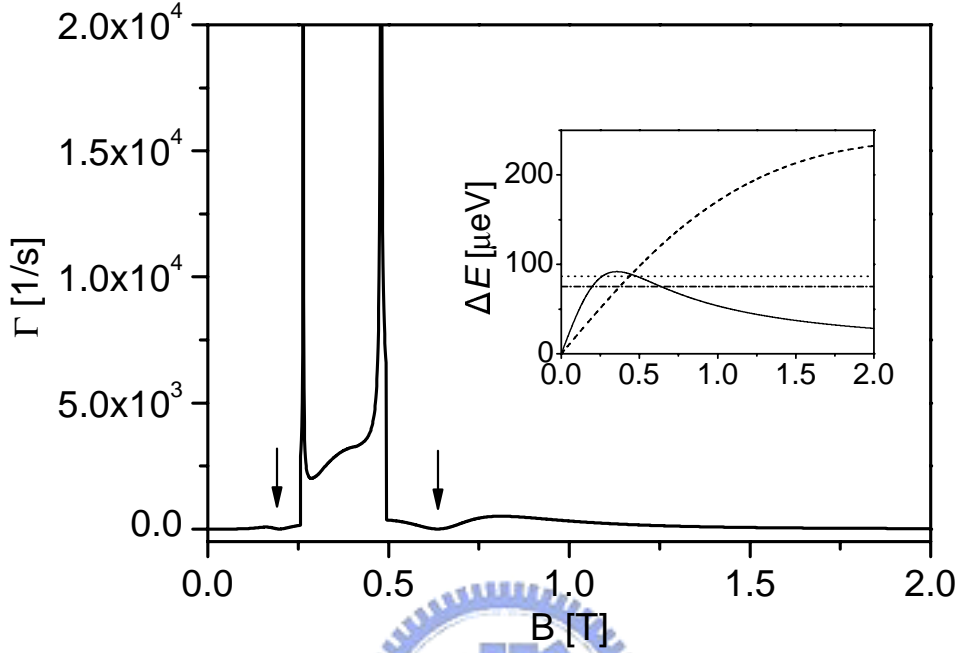


Figure 8.4: Spin relaxation rate for the lateral length $l_0 = 60$ nm, width $a = 130$ nm, and temperature $T=100$ mK. The spin-orbit couplings λ_R and λ_D are set equal to 5×10^{-13} and 16×10^{-12} eV m, respectively. Two enhanced and suppressed rates (arrow) occur. The inset shows the energy spacing ΔE vs the magnetic field B for different lateral lengths: $l_0 = 30$ nm (dashed line) and $l_0 = 60$ nm (solid line). Two horizontal lines in the inset indicate the corresponding energies for the van Hove singularity (dotted line) and the suppression of the rate (dashed-dotted line).

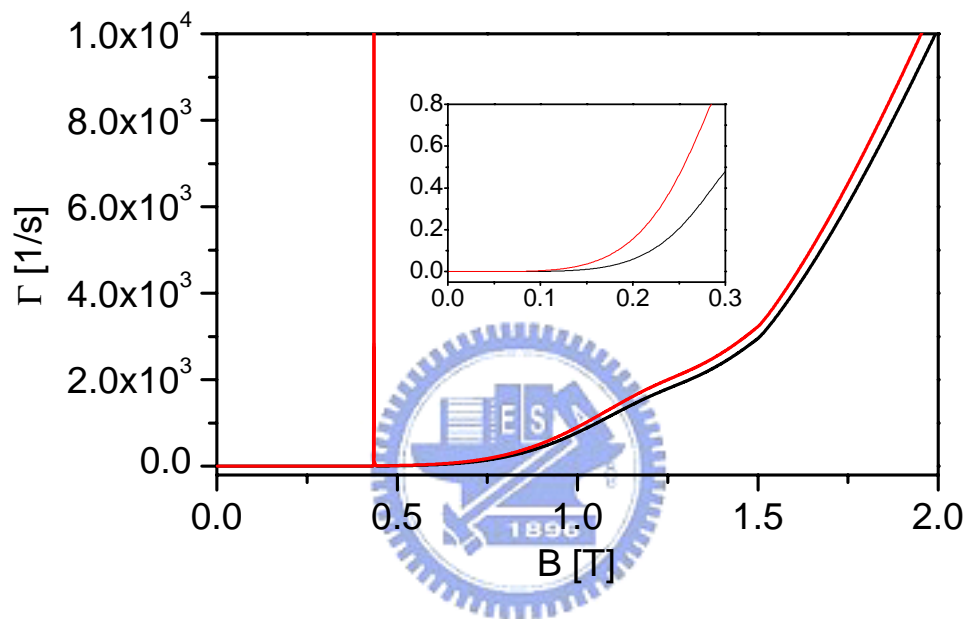


Figure 8.5: Spin relaxation rates for different temperatures: $T=10$ mK (black line) and $T=1$ K (red line). The inset shows the rates in the low field regime.

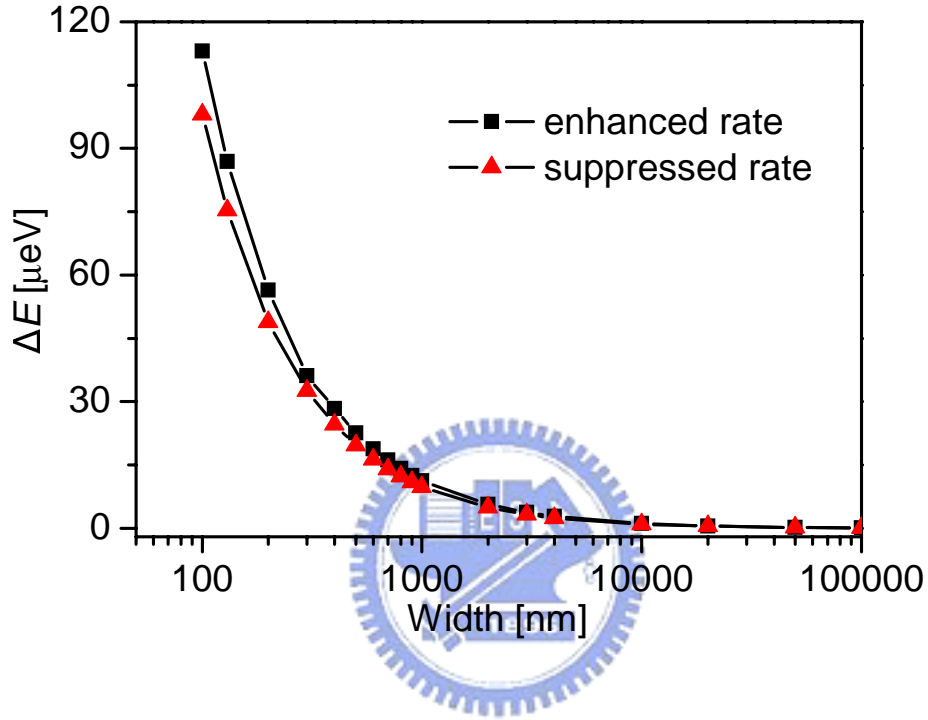


Figure 8.6: Dependence of the specific energy spacings ΔE for the enhanced (black mark) and suppressed (red mark) rates on the width a . The lateral length of the quantum dot is 30 nm. The Rashba constant is $\lambda_R = 5 \times 10^{-12}$ eVm and the Dresselhaus constant is $\lambda_D = 16 \times 10^{-12}$ eVm.

CHAPTER 9

ELECTRON TRANSPORT THROUGH A DOUBLED QUANTUM DOT SYSTEM WITH SINGLE PHONON

MODE

Recently, the transport properties of quantum dots show a range of interesting and important phenomena including the Coulomb blockade, Kondo resonance and interference effect [89, 90, 91, 92, 93, 94]. Conventionally, laterally defined double quantum dots are fabricated from a two-dimensional electron gas (2DEG) in a GaAs/AlGaAs heterostructure. By using gate technology, a quantum dot can be defined in a small region. A basic quantum device, such as a single-electron transistor, is composed of two leads and one or more quantum dots. The material of the device can be a normal metal, superconductor, ferromagnetic material, or semiconductor. The behavior of the transport is sensitive to the properties of the quantum dots.

Many works have been devoted to understanding the processes that may cause the nonlinear transport of quantum dot. One of the processes is related to the phonon-assisted inelastic tunneling. The nonlinear electron transport, due to the coupling between the quantum dot and the phonon degrees of freedom, through

a double quantum dot device at low temperature was observed recently [69]. It is found that this phonon-assisted inelastic tunneling is related to the emission of phonon. Theoretical analysis shows that the interference effect of electron-phonon interaction governs the intradot electron tunneling process [70].

Due to the interplay between the electrical and mechanical degrees of freedom, the single-electron tunneling through the quantum dots is influenced under the environment of nanomechanical vibration. In contrast to the bulk material phonons which can dephase electronic quantum states, phonons of nanomechanical vibration are no longer a mere source of dissipation. With the help of nanotechnologies, controlling phonon properties becomes more possible such as free-standing structures. The phonon spectrum in the structures is split into discrete subbands, and quantization effects contribute greatly to the thermal conductivity [71, 72, 73]. Because of boundary conditions for vibration modes, the phonon-dispersion shows some singular properties such as the van Hove singularities, different from that in the bulk material. A 2DEG quantum dot embedded in a suspended phonon cavity has been exhibited in recent experimental works [74, 75]. The excitation of a localized phonon mode confined in the cavity completely suppresses the single electron tunneling in the transport spectrum. This has opened possible avenues to investigate the ultimate limit of single electrons interacting with individual phonon modes. Since the artificial mode spectrum of the phonon cavity is feasible, the phonon field will practicably control and operate the transport of quantum device.

In this chapter we perform the analysis for a double quantum dot embedded in a single-phonon environment. The electrons in the dots interact with single phonon mode. The transport behavior of one dot influenced through Coulomb or phonon field is studied as an excess electron stays in the other dot. Furthermore, a positive- or negative-shift in conductance is also discussed by varying the separation between two dots.

9.1 Model

We consider a double quantum dot couples with a single-phonon mode as shown in Fig. 9.1. Each dot is connected with two normal conducting leads. Two quantum dots are separated by d . With split gate technology, the tunnel coupling between two dots can be neglected. This means that the upper and lower half parts of the device form two independent circuits. The energy levels of Dot α are controlled by gate voltages, where $\alpha = 1, 2$ indicate the upper and lower quantum dots. Because two quantum dots are embedded into a single-phonon environment, the electrons in the double-dot will interact with single phonon mode corresponding to the coupling strength λ_α . To study the transport in the lower half part of this device, we consider the transport of Dot 1 by tuning the occupation of electron on the Dot 2. The system Hamiltonian under consideration is written as

$$H = H_{res} + H_{dot} + H_c + H_T + H_{ph} + H_{ep}. \quad (9.1)$$

The first term describes the electron reservoir contributions:

$$H_{res} = \sum_{k \in L, R} \epsilon_k c_k^\dagger c_k, \quad (9.2)$$

where $c_k(c_k^\dagger)$ is the annihilation(creation) operator with wavevector k in the left (L) and right (R) leads. The leads are independent and connected with Dot 1.

The second and third terms describe the dot contributions and the Coulomb interaction between the electrons located in different dots:

$$H_{dot} + H_c = \sum_{\alpha=1,2} \epsilon_\alpha d_\alpha^\dagger d_\alpha + U d_1^\dagger d_1 d_2^\dagger d_2, \quad (9.3)$$

where $d_\alpha(d_\alpha^\dagger)$ is the annihilation(creation) operator in Dot α ($= 1, 2$), respectively. For simplicity, we consider that each quantum dot has a single particle energy level ϵ_α in the Coulomb blockade regime. The strength U depends on the distance between the centers of the dots. Note that the intradot Coulomb interaction is assumed to be much larger than the source (drain) voltage and the interdot Coulomb interaction. This would make the contribution of excited state negligible within our range of parameters. We thus simply consider the transport properties of single level [95, 96]. The electron-leads coupling can be written as

$$H_T = \sum_{k \in L, R} (V_k c_k^\dagger d_1 + \text{H.c.}), \quad (9.4)$$

with the tunneling matrix elements V_k . The last two terms describe the phonon reservoir contribution and the electron-phonon coupling:

$$H_{ph} + H_{ep} = \omega_0 a^\dagger a + \sum_{\alpha=1,2} d_\alpha^\dagger d_\alpha (\lambda_\alpha a + \text{H.c.}), \quad (9.5)$$

where ω_0 is the phonon frequency, λ_α is the coupling strength and $a(a^\dagger)$ denotes the phonon annihilation(creation) operator.

In order to study the electric current, the dot electron Green's functions are calculated. To diagonalize the Hamiltonian, a unitary transformation $e^s H e^{-s}$ is performed, where

$$S = \exp \left[- \sum_{\alpha=1,2} \frac{d_\alpha^\dagger d_\alpha}{\omega_0} (\lambda_\alpha a - \text{h.c.}) \right]. \quad (9.6)$$

After the transformation, the new Hamiltonian becomes

$$\begin{aligned} \bar{H} = & \sum_{k \in L,R} \epsilon_{k,\eta} c_k^\dagger c_k + \sum_{\alpha=1,2} \epsilon'_\alpha d_\alpha^\dagger d_\alpha + \Delta d_1^\dagger d_1 d_2^\dagger d_2 \\ & + \sum_{k \in L,R} V_k c_k^\dagger d_1 + \text{h.c.} + \omega_0 a^\dagger a, \end{aligned} \quad (9.7)$$

where the states in the dots and the Coulomb energy are renormalized to $\epsilon'_\alpha = \epsilon_\alpha - |\lambda_\alpha|^2 / \omega_0$ and $\Delta = U - (\lambda_1 \lambda_2^\dagger + \lambda_1^\dagger \lambda_2) / \omega_0$, respectively. In the weak coupling limit, we neglect the effective phonon-mediated coupling between dots and leads.

Following the standard method [97], the retarded Green's function of Dot 1 can be decoupled as

$$G_{\text{Dot } 1}^r = \tilde{G}_{\text{Dot } 1}^r(t) \langle X(t) X^\dagger(0) \rangle_{ph}, \quad (9.8)$$

where $\tilde{G}_{\text{Dot } 1}^r(t)$ is the Green's function for the dressed electron in the Dot 1 and $\langle X(t) X^\dagger(0) \rangle_{ph}$ is the phonon correlation function due to the electron-phonon interaction. $\langle X(t) X^\dagger(0) \rangle_{ph}$ can be written as $e^{-\Phi(t)}$, where $\Phi(t) = (|\lambda_1|^2 / \omega_0^2) [N_{ph}(1 - e^{i\omega_0 t}) + (N_{ph} + 1)(1 - e^{-i\omega_0 t})]$ with the Bose distribution of phonon N_{ph} . With the help of the equation-of-motion approach, we neglect the contribution of the

higher-order Green functions and subsequently the retarded Green's function for the dressed electron under the Fourier transform can be evaluated as

$$\tilde{G}_{\text{Dot 1}}^r(\omega) = \frac{1 - \langle n_2 \rangle}{\omega - \epsilon'_1 - \Sigma^r} + \frac{\langle n_2 \rangle}{\omega - \epsilon'_1 - \Delta - \Sigma^r}, \quad (9.9)$$

where $\langle n_2 \rangle$ is the number of the electrons in the Dot 2 and Σ^r is the retarded self-energy given by $\sum_{k \in L, R} V_k^* V_k / (\omega - \epsilon_k + i\eta)$ with $\eta = 0^+$. In this work we interest in the Coulomb blockade regime. The lowest order truncation is used for the approach. Under this approximation, no Kondo problem is considered here. For simplicity, we assume that the temperature is at zero temperature because the temperature of the system is low compared to the phonon frequency. The Green's function can be written as

$$G_{\text{Dot 1}}^r(\omega) = e^{-\frac{|\lambda_1|^2}{\omega_0^2}} \sum_l \frac{|\lambda_1|^{2l}}{\omega_0^{2l}} \frac{l!}{l!} \left[\frac{1 - \langle n_2 \rangle}{\omega - \epsilon'_1 - l\omega_0 - \Sigma^r} + \frac{\langle n_2 \rangle}{\omega - \epsilon'_1 - \Delta - l\omega_0 - \Sigma^r} \right], \quad (9.10)$$

Now let us analyze the relationship between the two couplings λ_1 and λ_2 for a phonon mode with wave vector \mathbf{q} . For simplicity, it is assumed that the electron densities in the dots have the same profiles and distribute sharply around the dot centers. Based on this assumption of identical profile, but spatially shifted electron densities in the two dots, one can establish the relation between the two couplings as, $\lambda_2 = \lambda_1 \exp[i\mathbf{q}\mathbf{d}]$, where \mathbf{d} is the vector connecting the centers of Dot 1 and Dot 2 [70, 98]. In the following, the corresponding parameters $\epsilon'_1 = \epsilon_1 - |\lambda_1|^2 / \omega_0$, $\epsilon'_2 = \epsilon_2 - |\lambda_1|^2 / \omega_0$, and $\Delta = U - 2|\lambda_1|^2 \cos \mathbf{q}\mathbf{d} / \omega_0$ are considered.

By employing Keldysh's Green function method [99, 100], the electron current flowing through Dot 1 can be calculated in term of the Green's functions of Dot 1 as:

$$J_{\text{Dot 1}} = -\frac{2e}{h} \int d\omega [f_L(\omega - \mu_L) - f_R(\omega - \mu_R)] \times \frac{\Gamma_L(\omega)\Gamma_R(\omega)}{\Gamma_L(\omega) + \Gamma_R(\omega)} \text{Im}[G_{\text{Dot 1}}^r(\omega)] \quad (9.11)$$

where $f_L(\omega - \mu_L)$ and $f_R(\omega - \mu_R)$ are the Fermi distribution function for the left lead 1 and right lead 1, respectively. Because a bias (V) is applied on two leads, the chemical potential difference can be determined by $\mu_L - \mu_R = eV$. Where Γ_L (Γ_R) denotes the transition rate from Dot 1 to the left lead (right lead), and $\Gamma_L(\Gamma_R) = 2\pi \sum_{k \in L(R)} V_k^* V_k \delta(\omega - \epsilon_k)$. In this work, we neglect the energy dependence of the transition rate in the wide-band limit and the symmetrical case is considered, i.e. $\Gamma_L = \Gamma_R = 0.1 \omega_0$. From a recent experiment with a free-standing phonon cavity, the typical phonon cavity energy is $100 \mu eV$ [75, 98]. We use the phonon frequency as an energy scale in the following. On the other hand, based on recent experimental observations about single-electron tunneling [54, 101, 102], the variation in electron numbers of a quantum dot (Dot 2) can easily be controlled and achieved by the associated technologies. For the sake of simplicity we would choose the condition ($\epsilon_1 = 0$) and focus on two situations: $\langle n_2 \rangle = 0$ (an empty Dot 2) and $\langle n_2 \rangle = 1$ (a singly occupied Dot 2).

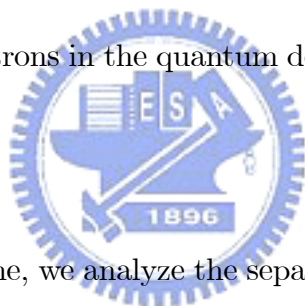
9.2 Results and discussion

Now let us consider two quantum dots which are separated in a short distance. This implies that the Coulomb interaction is larger than $-2|\lambda_1|^2 \cos \mathbf{qd}/\omega_0$. Therefore, the phonon effect is negligible in this situation. The dotted curve in Fig. 9.2 shows the conductance of Dot 1 if no electron tunnels into Dot 2 ($\langle n_2 \rangle = 0$). The main peak is due to resonant tunneling, while the weaker peaks show the phonon sidebands. The solid curve in Fig. 9.2 shows the conductance of Dot 1 if an excess electron stays in the Dot 2 ($\langle n_2 \rangle = 1$). The conductance of Dot 1 shows a positive shift U . Comparing the behavior of the shifts, we can expect that the energy level of Dot 1 is raised by the Coulomb interaction as shown in the inset.

If two quantum dots are separated in a long distance, the contribution of the Coulomb field will become very small. In such case, phonon field plays a bridge for the two quantum dots. Here we set $\cos \mathbf{qd}$ to 1, for example. As can be seen in Fig. 9.3, the conductance of Dot 1 shows a negative shift of $-2|\lambda_1|^2/\omega_0$. This indicates that the effect of electron-phonon interaction lowers the level of Dot 1 (inset).

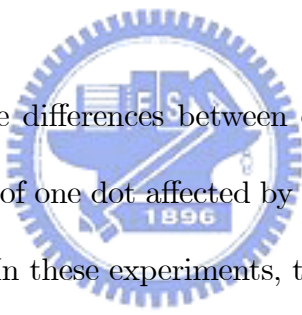
Next we discuss the mechanisms of the shifts in this device. Two single-electron transistors form two independent circuits. As an excess electron stays in one dot, the other circuit will be drastically affected. If one electron tunnels in the other dot, it will feel that there are two fields to influence the transport. One is the Coulomb field, which is due to electron-electron interaction. The parameters of

material and separation between two dots determine the strength. Because of the Coulomb repulsion, the energy level of Dot 1 can be raised like the effect of the Coulomb blockade. This direct interaction causes a positive-shift conductance. Another is the phonon field which causes electron-phonon interaction. As two electrons are coupled together to a single phonon, one can expect that one electron does not directly interact with the other electron, but it will affect indirectly the other electron by phonon field. This indirect interaction causes an equivalent attractive interaction between the two electrons, and corresponds to the reduction of the energy level of Dot 1 (in the condition of $\cos \varphi_d = 1$). It is also clear that the effective Coulomb strength Δ is negative in this case. This negative Coulomb interaction for electrons in the quantum dots leads to a negative-shift in conductance.



For long separation regime, we analyze the separation dependence on conductance. For simplicity, we assume that the phase factor φ_d is set to $2n\pi$ for initial separation of two dots, where n is a fixed integer. If the separation increases, the corresponding phase factor is equal to a real number $(2n\pi + \chi)$. Figure 9.4 illustrates Fermi energy at the resonant peak varies with the phase factor χ for different electron occupations of Dot 2. As the separation increases, the conductance displays a periodic behavior. We divide two regions by the value of Fermi energy at resonant peak without an excess electron in the Dot 2 (dotted line). For upper half part, the conductance shows different degrees of positive shifts, similar to the

case of short separation regime. This results from the phase factor φ_d so that the effective Coulomb potential is positive. In particular, if the phase factor occurs at $(2m + 1)\pi$ with integer m , the conductances show the maximum positive shifts. Oppositely, for lower half part, the conductances show different degrees of negative shifts. As previously mentioned, two electrons in the quantum dots attract each other by phonon field. Of course, the minimum points will appear at the positions as $\varphi_d = 2m\pi$. One can note that there are some intersections of solid and dotted curves. At these points, the conductance (solid curve) behaves like that of $\langle n_2 \rangle = 0$. This indicates that the occupation of an excess electron in the Dot 2 plays no role as the phase factor is equal to $(2m + 1)\pi/2$.



A few remarks about the differences between our model and recent experiments [101] on the transport of one dot affected by the operation of the other dot should be emphasized here. In these experiments, the double quantum dots have no interdot tunneling, but are coupled by a floating interdot capacitor. Because the capacitor plate enhances the Coulomb interaction, a single excess electron in one dot can influence the transport of the other dot. However, in our model, double quantum dots are coupled by two fields: Coulomb field and phonon field. Second, a particular relationship between two fields is constructed in our work. In short separation regime, the Coulomb repulsion dominates. Oppositely, the phonon field determines the sign of the effective Coulomb strength, which reflects the positive or negative shift in conductance. This is different from the above

situation. Furthermore, the significant behavior manifested in the transport properties under the competition between two fields might be useful in the study of the transport behavior of the multi-dot system. The degree of influence on transport depends on the electron numbers and separations of the dots. For example, in long separation regime, the transport of one dot is able to be affected by the electron numbers of the other dots. By increasing the electron numbers of the other dots, the conductance of one dot can show a shift behavior such that the transport through this dot is suppressed. Of course, if the levels of the other dots are no longer occupied, this circuit will be no change. In fact, we can simultaneously control the transports of different dots through proper operations of the electron numbers of the other dots. Therefore, these findings may be useful in the research field of logic circuits by using the Coulomb or phonon field.



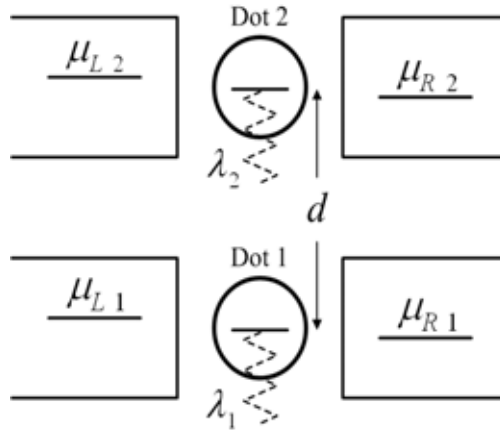


Figure 9.1: Schematic view of double quantum dot embedded in a single phonon environment. Two dots are connected with the leads respectively. The separation between two quantum dots is d and the interdot tunneling is forbidden with split gate technology.

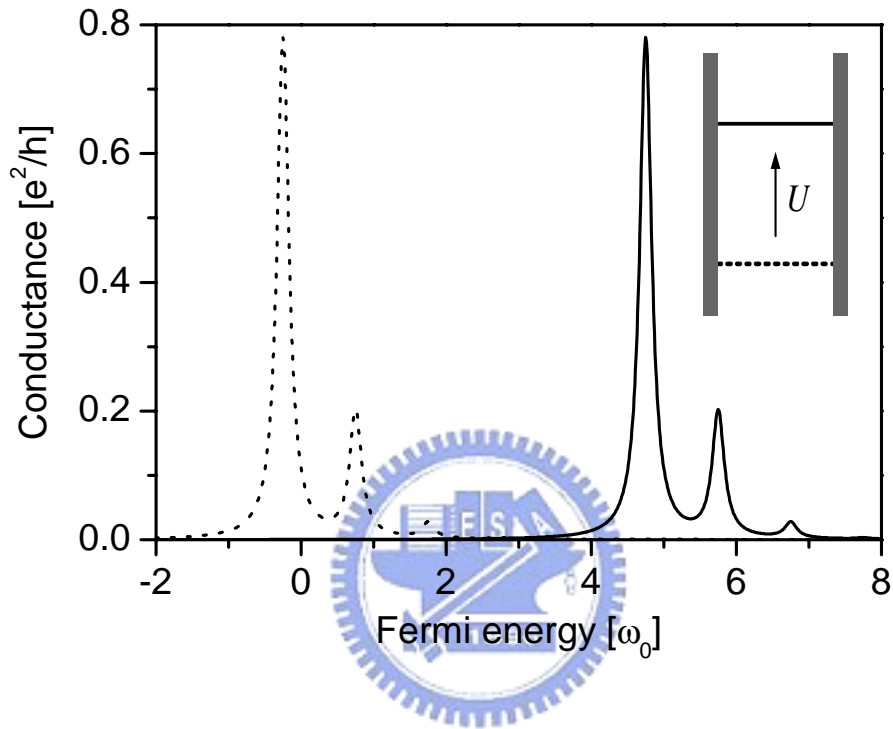


Figure 9.2: Short separation regime ($\Delta \approx U$): Linear conductance of Dot 1 (plotted in units of e^2/h) as a function of Fermi energy. The solid (dotted) curve shows the conductance if an (no) excess electron stays in the Dot 2, corresponding to the enhancement of resonant level (inset). The strength U is set to $5 \omega_0$.

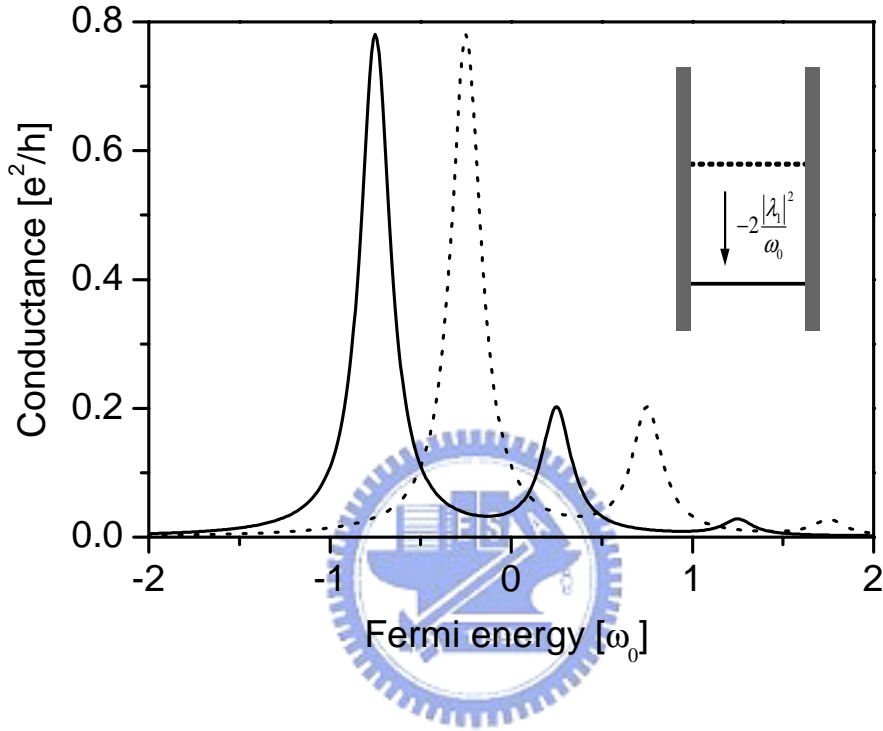


Figure 9.3: Long separation regime ($\Delta \approx -2|\lambda_1|^2/\omega_0$): Linear conductance of dot 1 (plotted in units of e^2/h) as a function of Fermi energy. The solid (dotted) curve shows the conductance if an (no) excess electron stays in the Dot 2, corresponding to the reduction of resonant level (inset). The coupling λ_1 is set to $0.5 \omega_0$.

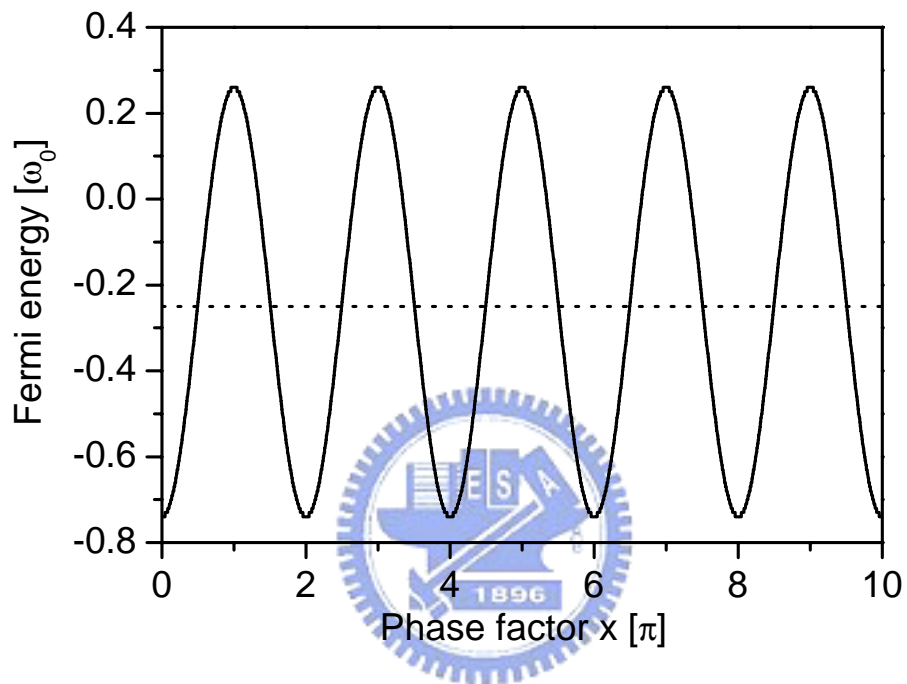


Figure 9.4: Fermi energy at the resonant peak as a function of phase factor for long separation regime. The solid (dotted) curve shows the conductance if an (no) excess electron stays in the Dot 2.

CHAPTER 10

ELECTRON TRANSPORT THROUGH A DRIVEN THREE-LEVEL DOUBLE DOT

Due to the zero dimensionality and quantized energy levels, transport properties of the electrons in quantum dots have been studied extensively [54, 53]. With the advances of nanotechnologies, quantum dots can be laterally fabricated from a two-dimensional electron gas in a heterostructure. With the combination of the controlling gates, the leads and quantum dots can form a quantum device. The electronic and optical properties are sensitive to the characteristics of the quantum dots. Since the flexible characteristics are controllable, the study of external influences on quantum dots has become an important issue. [76, 77].

Recently, quantum-dot systems in the presence of time-varying external fields manifest some interesting effects ranging from photon-assisted tunneling [78] to electron pumping [79]. In a recent experiment, the transport spectroscopy has been measured in coupled double quantum dots under microwave fields [78]. The photon-assisted resonances are found due to a modulated gate voltage. The phenomenon involves the emission or absorption of a microwave photon.

On the theoretical side, electron tunneling through quantum dots under driving

fields has been intensively addressed [100, 103, 104, 105, 106]. Many studies focus on two-level system in single or double quantum dot. The transport property is basically related to the energy difference between two levels. In the present work we study the electron tunneling through a three-level system using the master equation method. By applying an external field on the device, a significant behavior is found in the current spectrum. Different from two-level system, the transport depends on the relation among three levels and external field. We discuss the behavior of the current by varying some related parameters.

10.1 Model

We consider that a three-level system is defined in a double quantum dot device as shown in Fig. 10.1. Because the magnitude of energy levels in the quantum dots can be modulated with the help of nanotechnologies, the excited states of the left dot are designed to be much larger than the first excited state of the right dot, i.e., the size of the left dot is smaller. A continuous, near-resonant field irradiates on the device and gives rise to the contribution of the first excited state in the right dot. We reasonably concentrate on the transition between two states in the right dot and neglect the excitation in the left dot. For the tunneling between two dots, the electron is allowed to tunnel between two ground states, but no tunneling between two excited states is allowed. This means that we consider only the ground state in the left dot, the ground state and first excited state in

the right dot in our model. Furthermore, we restrict that only one additional electron is allowed on either the left or right dot in the Coulomb blockade regime [107, 108]. Under consideration, the effective Hilbert space of the electronic system can be defined by four states: empty, left, right, and excited states, corresponding to $|0\rangle = |N_L, N_R, N_E\rangle$, $|L\rangle = |N_L + 1, N_R, N_E\rangle$, $|R\rangle = |N_L, N_R + 1, N_E\rangle$, and $|E\rangle = |N_L, N_R, N_E + 1\rangle$, respectively. The total Hamiltonian of the system is

$$H = H_{res} + H_{dot} + H_V + H_T + H_{ep}. \quad (10.1)$$

The first term describes the electron reservoir contributions:

$$H_{res} = \sum_{k \in L} \varepsilon_k^L c_k^\dagger c_k + \sum_{k \in R} \varepsilon_k^R d_k^\dagger d_k, \quad (10.2)$$

where $c_k(c_k^\dagger)$ is the annihilation (creation) operator in the left lead (L) with wave vector k and $d_k(d_k^\dagger)$ is the annihilation (creation) operator for the right lead (R).

The term H_{dot} describes the contributions of three states in the double dot:

$$H_{dot} = \varepsilon_L \hat{n}_L + \varepsilon_R \hat{n}_R + \varepsilon_E \hat{n}_E, \quad (10.3)$$

where the energy levels $\varepsilon_L, \varepsilon_R$, and ε_E are corresponding to the ground state in the left dot, the ground state and first excited state in the right dot, respectively.

The operators of three states are given by $\hat{n}_L = |L\rangle \langle L|$, $\hat{n}_R = |R\rangle \langle R|$, and $\hat{n}_E = |E\rangle \langle E|$. The dot-lead coupling can be written as

$$H_V = \sum_k (V_k^L c_k^\dagger \hat{s}_L + V_k^R d_k^\dagger \hat{s}_R + V_k^E d_k^\dagger \hat{s}_E + \text{H.c.}), \quad (10.4)$$

with the operators $\hat{s}_L = |0\rangle\langle L|$, $\hat{s}_R = |0\rangle\langle R|$, and $\hat{s}_E = |0\rangle\langle E|$, and the tunneling matrix elements V_k^α for $\alpha (= L, R, \text{ and } E)$. The term H_T describes the tunneling between the left dot and the right dot,

$$H_T = T_c(\hat{P} + \hat{P}^\dagger), \quad (10.5)$$

where the operator \hat{P} (\hat{P}^\dagger) is defined by $|L\rangle\langle R|$ ($|R\rangle\langle L|$) and the tunnel matrix element T_c determines the strength of the tunneling process. In the dipole and rotating-wave approximations, the last term H_{ep} which describes the interaction between electron and external field in the right dot can be expressed as,

$$H_{ep} = -\frac{\gamma}{2}(\hat{Q}e^{-i\omega t} + \hat{Q}^\dagger e^{i\omega t}), \quad (10.6)$$

where γ is the Rabi frequency, ω is the field frequency, and the operator \hat{Q} (\hat{Q}^\dagger) denotes $|E\rangle\langle R|$ ($|R\rangle\langle E|$). The Rabi frequency relates to the field strength and the electric dipole moment for the transition $|R\rangle \leftrightarrow |E\rangle$ [109, 110].

An analytical expression for the stationary current can be solved from the master equation [106]. One can obtain an equation of motion for the time-dependent expectation values of the operators \hat{n}_L , \hat{n}_R , \hat{n}_E , \hat{P} , \hat{Q} , and \hat{S} where \hat{S} denotes $|E\rangle\langle L|$. After the Laplace transformation (e.g., $n_L(z) = \int_0^\infty dt e^{-zt} \langle \hat{n}_L \rangle_t$), these corresponding equations can be written as

$$\begin{aligned} n_L(z) = & -i\frac{T_c}{z}\{P(z) - P^\dagger(z)\} + \frac{\Gamma_L}{z}\{1/z - n_L(z) \\ & - n_R(z) - n_E(z)\}, \end{aligned}$$

$$\begin{aligned}
n_R(z) &= i\frac{T_c}{z}\{P(z) - P^\dagger(z)\} + i\frac{\gamma}{2z}\{Q(z + i\omega) \\
&\quad - Q^\dagger(z - i\omega)\} - \frac{\Gamma_R}{z}n_R(z), \\
n_E(z) &= -i\frac{\gamma}{2z}\{Q(z + i\omega) - Q^\dagger(z - i\omega)\} - \frac{\Gamma_R}{z}n_E(z), \\
P(z) &= -i\frac{\gamma}{2(z - i\Delta\varepsilon)}\{n_L(z) - n_R(z)\} - \frac{\Gamma_R}{2(z - i\Delta\varepsilon)}P(z) \\
&\quad - i\frac{\gamma}{2(z - i\Delta\varepsilon)}S^\dagger(z), \\
Q(z) &= -i\frac{\gamma}{2(z - i\Delta R)}\{n_E(z - i\omega) - n_R(z - i\omega)\} \\
&\quad - i\frac{T_c}{z - i\Delta R}S(z) - \frac{\Gamma_R}{z - i\Delta R}Q(z), \\
S(z) &= -i\frac{T_c}{z - i\Delta L}Q(z) + i\frac{\gamma}{2(z - i\Delta L)}P^\dagger(z - i\omega) \\
&\quad - \frac{\Gamma_R}{2(z - i\Delta L)}S(z), \tag{10.7}
\end{aligned}$$

where the parameters are $\Delta\varepsilon = \varepsilon_L - \varepsilon_R$, $\Delta L = \varepsilon_E - \varepsilon_L$, and $\Delta R = \varepsilon_E - \varepsilon_R$, respectively. The tunneling rates between the reservoirs and dots are assumed to be independent of energy, $\Gamma_\alpha = 2\pi \sum_k |V_k^\alpha|^2 \delta(\varepsilon_\alpha - \varepsilon_k^{L/R})$, with α ($= L, R$, and E). We can solve the equation (10.7) algebraically and subsequently obtain the stationary current (in units of e) from the tunneling between two dots

$$I = iT_c \left\{ P - P^\dagger \right\}_{t \rightarrow \infty}. \tag{10.8}$$

To simplify the parameters of the system, the tunneling rates are assumed to be identical ($\Gamma_L = \Gamma_R = \Gamma_E$). In this work the tunneling rate (Γ) and the charging energy ($\varepsilon_E - \varepsilon_R$) in the right dot are set to be $8 \mu eV$ and $1 meV$ respectively.

10.2 Results and discussion

We first consider the field frequency is in resonance ($\Delta\omega = \omega - \Delta R = 0$). The current can be written as

$$I = \frac{4T_c^2\Gamma}{12T_c^2 + 4(\Delta\varepsilon)^2 + \Gamma^2 + f(\gamma, \Delta\varepsilon, \Delta L)}, \quad (10.9)$$

where $f(\gamma, \Delta\varepsilon, \Delta L)$ is related to the three levels and external field. This function f is directly dependent of the Rabi frequency. For a two-level system ($\gamma = 0$), the current is

$$I = \frac{4T_c^2\Gamma}{12T_c^2 + 4(\Delta\varepsilon)^2 + \Gamma^2} \quad (10.10)$$

and shows a maximum response at $\Delta\varepsilon = 0$ (see Fig. 10.2) [104]. However, as a resonant field is applied to the device ($\gamma = 5\Gamma$), two symmetric peaks obviously separate and occur in the current spectrum. Compared with the case of $\gamma = 0$, the maximum current do not locate at the point ($\Delta\varepsilon = 0$). Further, we analyze the components of the current in this device. For the right dot, the ground and first excited states can contribute the transport as shown in Fig. 10.1. In the stationary case, Eq. (10.8) is equivalent to the contributions of two states in the right dot. The current can be re-written as

$$I = I_R + I_E, \quad (10.11)$$

$$I_R = \Gamma \cdot n_R, \quad (10.12)$$

$$I_E = \Gamma \cdot n_E, \quad (10.13)$$

where n_R and n_E is the populations in the right dot. From the inset, we find that electron tunneling through two channels behaves similarly and equally contributes the current.

In order to study the influence of the external field on the transport, in Fig. 10.3 we illustrate the curve of the Rabi-frequency-dependent current. For simplicity, the conditions are chosen to be $\Delta\varepsilon = 0$ and $\Delta\omega = 0$. The current can be written as

$$I = \frac{4T_c^2\Gamma}{12T_c^2 + \Gamma^2 + f(\gamma)}, \quad (10.14)$$

$$f(\gamma) = \gamma^2 \frac{\gamma^2 - 6T_c^2 + \Gamma^2}{\gamma^2 + 2T_c^2 + \Gamma^2}. \quad (10.15)$$

If the Rabi frequency γ is zero, the current is $4T_c^2\Gamma/(12T_c^2 + \Gamma^2)$ (red dotted line). As the frequency γ increases, a crossover from enhanced behavior to suppressed behavior in the transport spectrum is found. In addition, the current broadens with increasing the tunneling coupling (lower inset). This is due to the competition among the Rabi frequency γ , tunneling coupling T_c , and tunneling rate Γ (see Eq. (10.15)). For small Rabi frequency regime, a negative function ($f < 0$) causes an enhancement of the current. Two channels effectively contribute to the transport (upper inset). On the contrary, a large Rabi frequency inhibits the electron tunneling out of the right dot, thus, leading to a suppressed current.

In above results, a symmetric behavior manifests in the case of resonant field. We also find an interesting behavior by detuning the field frequency. In Fig. 10.4, the current shows two asymmetric peaks. This is similar to the result of Ref.

[111]. If the detuning is increased, the main (larger) peak will be close to the value $\Delta\varepsilon = 0$ while another one is far away from the main peak and deeply suppressed. This reflects the crossover from a three-level system to a two-level one. As can be seen in Fig. 10.4, two components I_R (red dashed curve) and I_E (blue dotted curve) contribute to the current, but the degrees of the contributions on the peaks are different. The main and smaller peaks result from the large contributions of the currents I_R and I_E respectively. One can expect that the external field establishes a particular relationship among the states. The distributions of populations are sensitive to the related parameters in the double dot system. Under the condition $\Delta\omega \neq 0$, compared to the symmetric current (Fig. 10.2), the electron transfer among these states shows an unbalanced behavior such that two channels in the right dot unequally contribute the peaks.

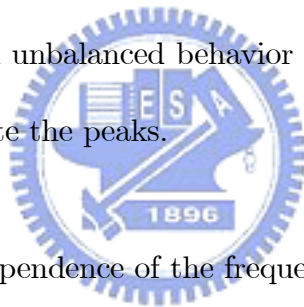


Figure 10.5 shows the dependence of the frequency on current for $\Delta\varepsilon = 0$. A symmetric and anti-resonant behavior appears in the transport spectrum. When the Rabi frequency increases, the current is greatly suppressed and a maximum response locates at the resonant frequency ($\Delta\omega = 0$). For the situation that the frequency of external field is far away from the resonant one, the current approaches to the situation without the Rabi frequency (red dotted line), i.e. the maximum value of the current in the two-level system. We further plot the populations for small and large Rabi frequencies (inset). It is clearly shown that the populations decrease with increasing the (Rabi) frequency. According to the phe-

nomenon, the destructive electron transfer results in a suppressed current under the special condition $\Delta\varepsilon = 0$.

However, if we detune the energy difference between two ground states in two dots, the current behaves differently. Figure 10.6 shows an asymmetric and enhanced current occurs. The location of maximum current is no longer fixed due to the unbalanced interplay between these states and driving field. As can be seen in the inset of Fig. 10.6, the populations are enhanced with increasing the Rabi frequency. Comparing with the result as shown in Fig. 10.5, this appearance corresponds to the result of constructive electron transfer.



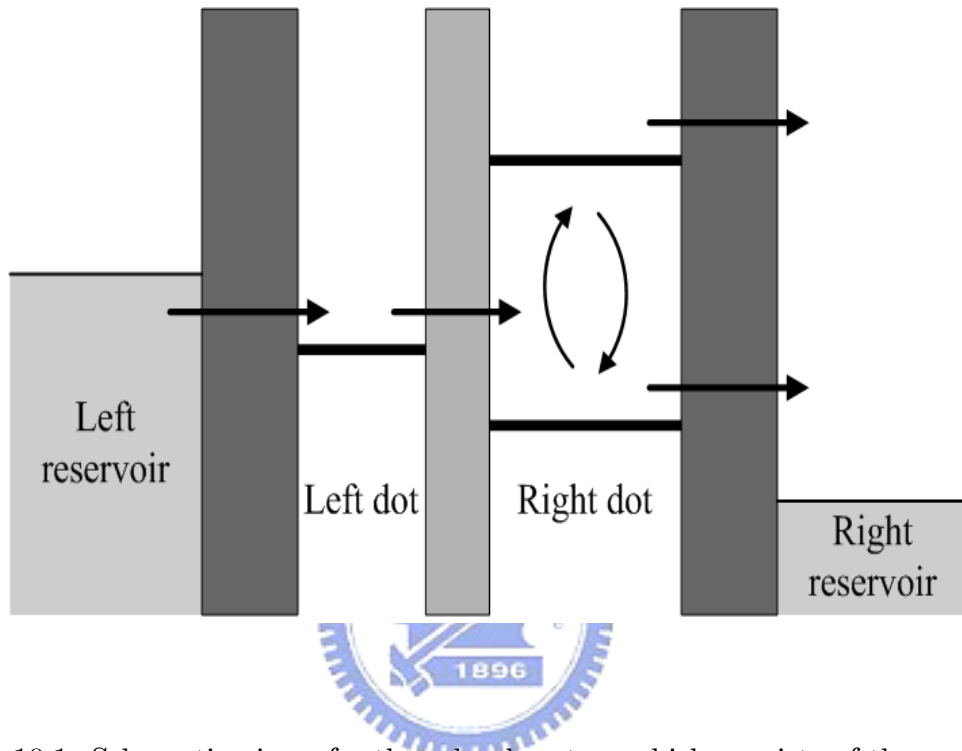


Figure 10.1: Schematic view of a three-level system which consists of the ground state in the left dot, the ground state and first excited state in the right dot in a double quantum dot device. An external field irradiates on the device and leads to the transition between two states in the right dot.

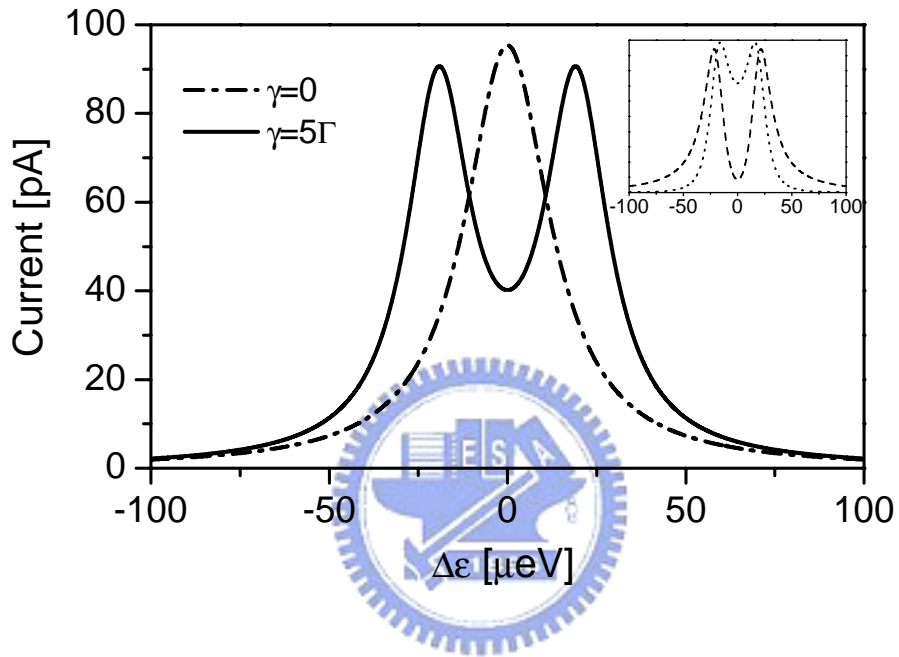


Figure 10.2: Current as a function of energy difference $\Delta\varepsilon$ between two ground states for different Rabi frequencies. The inset shows the currents I_R (dashed curve) and I_E (dotted curve) for $\gamma = 5\Gamma$.

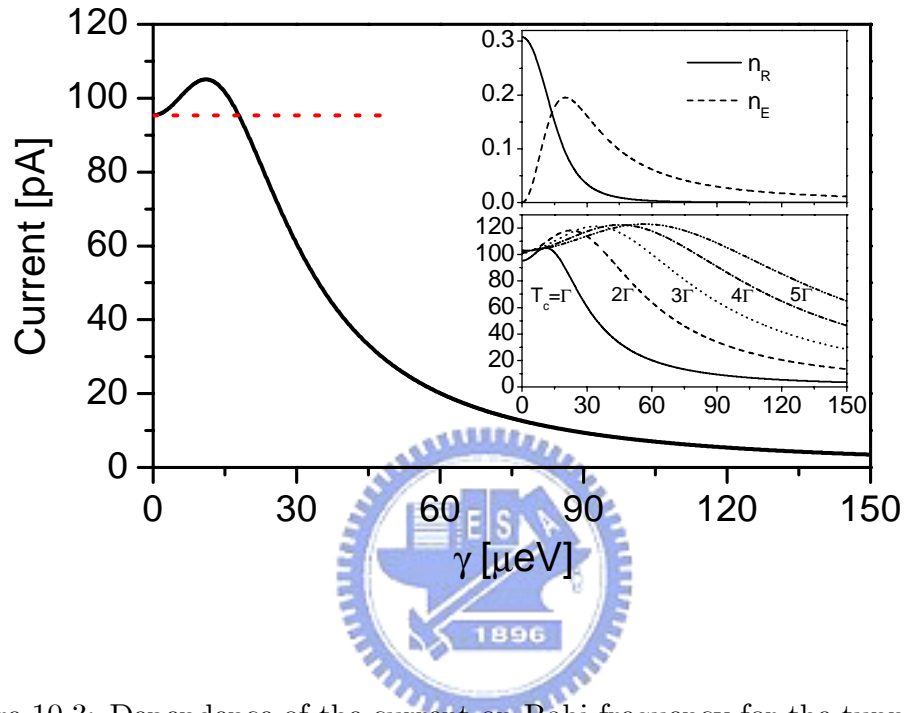


Figure 10.3: Dependence of the current on Rabi frequency for the tunneling coupling $T_c = \Gamma$, corresponding to the populations n_R and n_E (upper inset). The red dotted line marks the maximum current for two-level system. The lower inset shows the currents for different tunneling couplings. The conditions are fixed to be $\Delta\varepsilon = 0$ and $\Delta\omega = 0$.

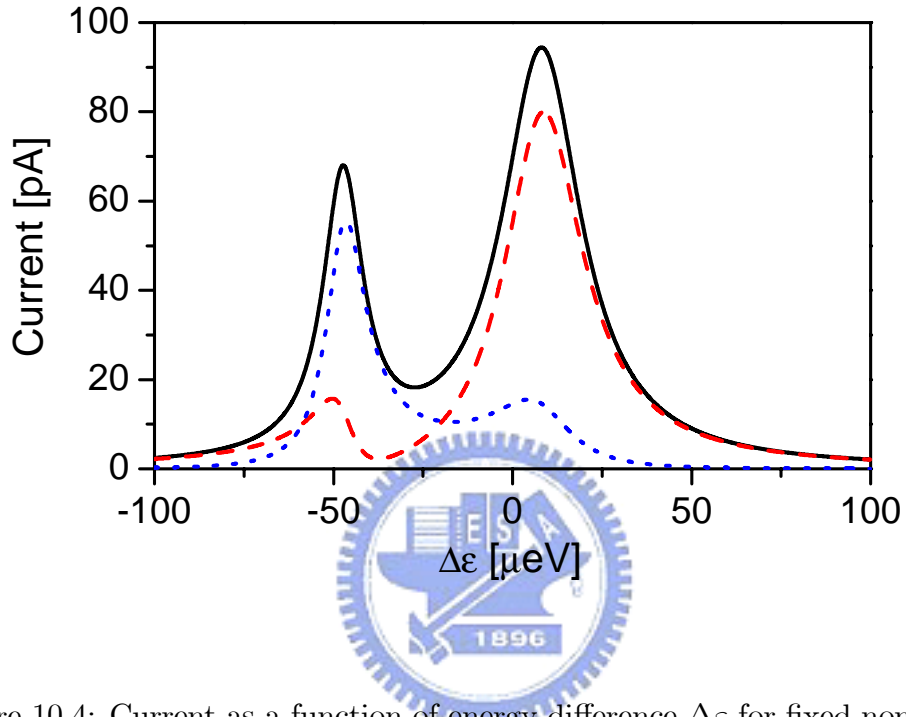


Figure 10.4: Current as a function of energy difference $\Delta\varepsilon$ for fixed non-resonant field ($\Delta\omega = 5 \Gamma$) and Rabi frequency ($\gamma = 5 \Gamma$). The total current I (black curve) is composed of two channels in the right dot: the electron tunneling out through the ground level I_R (red dashed curve) and first excited level I_E (blue dotted curve).

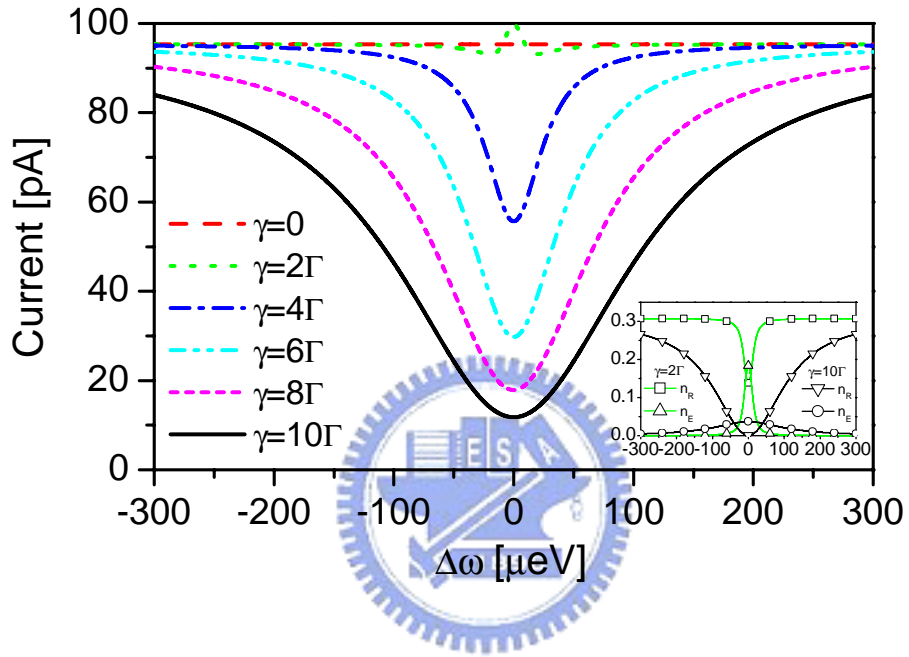


Figure 10.5: Current as a function of frequency difference $\Delta\omega$ ($= \omega - \Delta R$) for different Rabi frequencies and for fixed $\Delta\varepsilon = 0$. The inset shows the populations n_R and n_E for Rabi frequencies $\gamma = 2\Gamma$ and $\gamma = 10\Gamma$.

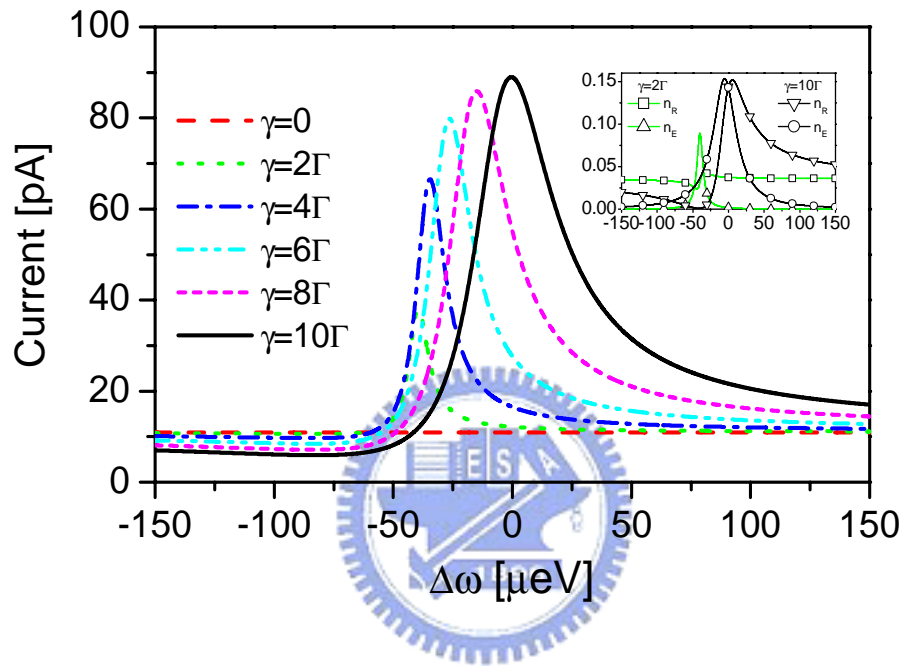


Figure 10.6: Current as a function of frequency difference $\Delta\omega$ ($= \omega - \Delta R$) for different Rabi frequencies and for fixed $\Delta\varepsilon = 5\Gamma$. The inset shows the populations n_R and n_E for Rabi frequencies $\gamma = 2\Gamma$ and $\gamma = 10\Gamma$.

CHAPTER 11

SUMMARY AND FUTURE WORK

In this part we have studied the phonon-induced spin relaxation in a two-dimensional quantum dot embedded inside a semiconductor slab. An enhanced relaxation rate is found due to the phonon van Hove singularities. Oppositely, it is found that at certain magnetic fields one enters a regime with quite the opposite characteristics, where a vanishing divergence of the displacement causes a suppression of spin relaxation rates. For larger dots there are multiple singularities and suppressions in the electron-phonon rates due to the interplay between spin-orbit coupling and Zeeman interaction. Furthermore, a crossover from confined to bulk-like systems is obtained by varying the width of the slab.

In the study on quantum transport, we have studied the electron transport through a quantum dot in double quantum dots embedded in a single phonon environment. By controlling the electron number in a quantum dot, the transport behavior of the other quantum dot is affected through Coulomb or phonon field. In long separation regime, the conductance shows a positive shift because the Coulomb interaction dominates in this case. On the other hand, the transport behavior drastically depends on the separation between two dots in long separation regime. In particular, crossover from positive to negative shift in conductance is

observed due to the phase factor.

In addition, we have studied the electron tunneling through a three-level system in an asymmetric double quantum dot device irradiated by an external field. The external field plays an important bridge between the two-level and the three-level systems. When a resonant field irradiates on the device, the current shows two symmetric peaks. In contrast, two asymmetric peaks display for the case of non-resonant field. By analyzing the contributions of the states in the right dot, we further find that the degrees of the contributions on the peaks are different. On the other hand, we also study the frequency-dependent current by modulating the energy difference between the ground states. It is clearly shown that a suppressed (enhanced) behavior occurs due to the destructive (constructive) electron transfer among the states. This allows us to control the transport of the device by tuning some related parameters.



Based on the results, some works can be proceeded continuously in the future: spin relaxation in different structures. In chapter 5, we examine the spin relaxation rate in single quantum dot. In general, a quantum device can be composed of one or more quantum dots. According to the recent studies, different arrangements show some different physical properties. It is thus interesting to study the spin relaxation in multi-dot systems. On the other hand, geometrical confinement strongly alters the properties of the phonon system. Apart from the semiconductor slab, we can consider single or more quantum dots embedded in

different structures. For example, a quantum wire with quantum dots has been achieved in the recent works [112]. Thus the effect of different quantum structures on the spin relaxation is worth studying.



BIBLIOGRAPHY

- [1] The Collected Works of Irving Langmuir, edited by C. G. Suits (Pergamon, New York, 1961).
- [2] U. Landman, G.G. Kleiman, C.L. Cleveland, E. Kuster, R.N. Barnett, and J.W. Gadzuk, Phys. Rev. B 29, 4313 (1984).
- [3] J. W. Gadzuk, U. Landman, E. J. Kuster, C. L. Cleveland, and R. N. Barnett, Phys. Rev. Lett. 49, 426 (1982).
- [4] Y. T. Shih, D. S. Chuu, and W. N. Mei, Phys. Rev. B 51, 14626 (1995).
- [5] Y. T. Shih, D. S. Chuu, and W. N. Mei, Phys. Rev. B 54, 10938 (1996).
- [6] Y. T. Shih, D. S. Chuu, and W. N. Mei, Solid State Commun. 99, 819 (1996).
- [7] Y. T. Shih, Y. Y. Liao, and D. S. Chuu, Phys. Rev. B 68, 075402 (2003).
- [8] J. Xu, A. Barnes, R. Albridge, C. Ewig, N. Tolk, and L. D. Hulett, Jr., Phys. Rev. B 48, 8222 (1993).
- [9] I. Beauport, K. Al-Shamery, and H.-J. Freund, Chem. Phys. Lett. 256, 641 (1996).

- [10] S. Thiel, M. Pykavy, T. Klüner, H.-J. Freund, R. Kosloff, and V. Staemmler, *Phys. Rev. Lett.* **87**, 077601 (2001).
- [11] S. Thiel, M. Pykavy, T. Klüner, H.-J. Freund, R. Kosloff, and V. Staemmler, *J. Chem. Phys.* **116**, 762 (2002).
- [12] H. Stapelfeldt and T. Seideman, *Rev. Mod. Phys.* **75**, 543 (2003).
- [13] B. Friedrich and D. Herschbach, *Phys. Rev. Lett.* **74**, 4623 (1995).
- [14] B. Friedrich and D. Herschbach, *J. Chem. Phys.* **111**, 6157 (1999).
- [15] B. Friedrich and D. Herschbach, *J. Phys. Chem. A*, **103**, 10280 (1999).
- [16] L. Cai, J. Marango, and B. Friedrich, *Phys. Rev. Lett.* **86**, 775 (2001).
- [17] J. Ortigoso, M. Rodriguez, M. Gupta, and B. Friedrich, *J. Chem. Phys.* **110**, 3870 (1999).
- [18] M. Machholm, *J. Chem. Phys.* **115**, 10724 (2001).
- [19] N. E. Henriksen, *Chem. Phys. Lett.* **312**, 196 (1999).
- [20] M. Machholm and N. E. Henriksen, *Phys. Rev. Lett.* **87**, 193001 (2001).
- [21] C. M. Dion, A. Keller, and O. Atabek, *Eur. Phys. J. D* **14**, 249 (2001).
- [22] A. Ben Haj-Yedder, A. Auger, C. M. Dion, E. Cancès, A. Keller, C. Le Bris, and O. Atabek, *Phys. Rev. A* **66**, 063401 (2002).

- [23] C. M. Dion, A. Ben Haj-Yedder, E. Cancès, C. Le Bris, A. Keller, and O. Atabek, *Phys. Rev. A* **65**, 063408 (2002).
- [24] O. Rogalsky, P. Vorderwisch, A. Huller, and S. Hautecler, *J. Chem. Phys.* **116**, 1063 (2002).
- [25] A. Würger, *Phys. Rev. Lett.* **88**, 063002 (2002).
- [26] D. DeMille, *Phys. Rev. Lett.* **88**, 067901 (2002).
- [27] H. Shima and T. Nakayama, *Phys. Rev. B* **69**, 035202 (2004).
- [28] H. Shima and T. Nakayama, *Phys. Rev. A* **70**, 013401 (2004).
- [29] W. Ho, *J. Chem. Phys.* **117**, 11033 (2002).
- [30] C. Hettich, C. Schmitt, J. Zitzmann, S. Kuhn, I. Gerhardt, and V. Sandoghdar, *Science* **298**, 385 (2002).
- [31] S. Yasutomi, T. Morita, Y. Imanishi, and S. Kimura, *Science* **304**, 1944 (2004).
- [32] R. P. Pan, R. D. Eppers, K. Kobashi, and V. Chandrasekharan, *J. Chem. Phys.* **77**, 1035 (1982).
- [33] J. W. Riehl and C. J. Fisher, *J. Chem. Phys.* **59**, 4336 (1973).
- [34] V. M. Allen and P. D. Pacey, *Surf. Sci.* **177**, 36 (1986).
- [35] *Handbook of Mathematical Functions*, edited by M. Abramowitz and I. A. Stegun (Dover, New York, 1970).

- [36] D. C. Jacobs, K. W. Kolasinski, R. J. Madix, and R. N. Zare, *J. Chem. Phys.* **87**, 5038 (1987).
- [37] H. Hou, S. J. Gulding, C. T. Rettner, A. M. Wodtke, and D. J. Auerbach, *Science* **277**, 80 (1997).
- [38] D. Wetzig, R. Dopheide, M. Rutkowski, R. David, and H. Zacharias, *Phys. Rev. Lett.* **76**, 463 (1996).
- [39] M. Rutkowski, D. Wetzig, and H. Zacharias, *Phys. Rev. Lett.* **87**, 246101 (2001).
- [40] C. H. Greene and R. N. Zare, *J. Chem. Phys.* **78**, 6741 (1983).
- [41] A. D. Buckingham, *Adv. Chem. Phys.* **12**, 107 (1967).
- [42] C. M. Dion, A. Keller, O. Atabek, and A. D. Bandrauk, *Phys. Rev. A* **59**, 1382 (1999).
- [43] P. A. Miller and S. Sarkar, *Phys. Rev. E* **60**, 1542 (1999).
- [44] H. Fujisaki, T. Miyadera, and A. Tanaka, *Phys. Rev. E* **67**, 066201 (2003).
- [45] D. You, R. R. Jones, P. H. Bucksbaum, and D. R. Dykaar, *Opt. Lett.* **18**, 290 (1993).
- [46] C. H. Bennett, H. J. Bernstein, S. Popescu, and B. Schumacher, *Phys. Rev. A* **53**, 2046 (1996).
- [47] S. Parker, S. Bose, and M. B. Plenio, *Phys. Rev. A* **61**, 032305 (2000).

- [48] See, for instance, Handbook of Chemistry and Physics, edited by D. R. Lide, 84th ed. (The Chemical Rubber Company, Boca Raton, (2003).
- [49] H. Sakai, S. Minemoto, H. Nanjo, H. Tanji, and T. Suzuki, Phys. Rev. Lett. **90**, 083001 (2003).
- [50] S. Minemoto, H. Nanjo, H. Tanji, T. Suzuki, and H. Sakai, J. Chem. Phys. **118**, 4052 (2003).
- [51] H. Sakai, S. Minemoto, H. Nanjo, H. Tanji, and T. Suzuki, Eur. Phys. J. D **26**, 33 (2003).
- [52] A. Weiner, Rev. Sci. Instrum. **71**, 1929 (2000).
- [53] S. M. Reimann and M. Manninen, Rev. Mod. Phys. **74**, 1283 (2002).
- [54] W. G. van der Wiel, S. De Franceschi, J. M. Elzerman, T. Fujisawa, S. Tarucha, and L. P. Kouwenhoven, Rev. Mod. Phys. **75**, 1 (2003).
- [55] H. Tamura, K. Shiraishi, and H. Takayanagi, in Quantum Dots and Nanowires, edited by S. Bandyopadhyay and H. S. Nalwa (American Scientific, 2003), p. 67.
- [56] G. Dresselhaus, Phys. Rev. **100**, 580 (1955).
- [57] M. I. D'yakonov and V. I. Perel', Zh. Éksp. Teor. Fiz. **60**, 1954 (1971) [Sov. Phys. JETP **38**, 1053 (1971)].
- [58] M. I. D'yakonov and V. Yu. Kachorovskii, Fiz. Tekh. Poluprovodn. **20**, 178 (1986) [Sov. Phys. Semicond. **20**, 110 (1986)].
- [59] Yu. L. Bychkov and E. I. Rashba, JETP Lett. **39**, 78 (1984).

- [60] Yu. L. Bychkov and E. I. Rashba, *J. Phys. C* **17**, 6039 (1984).
- [61] O. Voskoboynikov, C. P. Lee, and O. Tretyak, *Phys. Rev. B* **63**, 165306 (2001).
- [62] C. F. Destefani, S. E. Ulloa, and G. E. Marques, *Phys. Rev. B* **70**, 205315 (2004).
- [63] C. F. Destefani and S. E. Ulloa, *Phys. Rev. B* **71**, 161303(R) (2005).
- [64] A. V. Khaetskii and Y. V. Nazarov, *Phys. Rev. B* **61**, 12639 (2000).
- [65] A. V. Khaetskii and Y. V. Nazarov, *Phys. Rev. B* **64**, 125316 (2001).
- [66] L. M. Woods, T. L. Reinecke, and Y. Lyanda-Geller, *Phys. Rev. B* **66**, 161318(R) (2002).
- [67] R. de Sousa and S. Das Sarma, *Phys. Rev. B* **68**, 155330 (2003).
- [68] D. V. Bulaev and D. Loss, *Phys. Rev. B* **71**, 205324 (2005).
- [69] T. Fujisawa, T. H. Oosterkamp, W. G. van der Wiel, B. W. Broer, R. Aguado, S. Tarucha, and L. P. Kouwenhoven, *Science* **282**, 932 (1998).
- [70] T. Brandes and B. Kramer, *Phys. Rev. Lett.* **83**, 3021 (1999).
- [71] J. Seyler and M. N. Wybourne, *Phys. Rev. Lett.* **69**, 1427 (1992).
- [72] A. Greiner, L. Reggiani, T. Kuhn, and L. Varani, *Phys. Rev. Lett.* **78**, 1114 (1997).

- [73] L. G. C. Rego and G. Kirczenow, *Phys. Rev. Lett.* **81**, 232 (1998).
- [74] E. M. Höhberger, T. Krämer, W. Wegscheider, and R. H. Blick, *Appl. Phys. Lett.* **82**, 4160 (2003).
- [75] E. M. Weig, R. H. Blick, T. Brandes, J. Kirschbaum, W. Wegscheider, M. Bichler, and J. P. Kotthaus, *Phys. Rev. Lett.* **92**, 046804 (2004).
- [76] M. Grifoni and P. Hanggi, *Phys. Rep.* **304**, 229 (1998).
- [77] G. Platero and R. Aguado, *Phys. Rep.* **395**, 1 (2004).
- [78] T. H. Oosterkamp, T. Fujisawa, W. G. van der Wiel, K. Ishibashi, R. V. Hijman, S. Tarucha, and L. P. Kouwenhoven, *Nature (London)* **395**, 873 (1998).
- [79] M. Switkes, C. M. Marcus, K. Campman, and A. C. Gossard, *Science* **283**, 1905 (1999).
- [80] X. Hu and S. Das Sarma, *Phys. Rev. A* **61**, 062301 (2000).
- [81] M. Friesen, P. Rugheimer, D. E. Savage, M. G. Lagally, D. W. van der Weide, R. Joynt, and M. A. Eriksson, *Phys. Rev. B* **67**, 121301(R) (2003).
- [82] T. Fujisawa, D. G. Austing, Y. Tokura, Y. Hirayama, and S. Tarucha, *Nature (London)* **419**, 278 (2002).
- [83] R. Hanson, B. Witkamp, L. M. K. Vandersypen, L. H. Willems van Beveren, J. M. Elzerman, and L. P. Kouwenhoven, *Phys. Rev. Lett.* **91**, 196802 (2003).
- [84] J. M. Elzerman, R. Hanson, L. H. Willems van Beveren, B. Witkamp, L.

- M. K. Vandersypen, and L. P. Kouwenhoven, *Nature (London)* **430**, 431 (2004).
- [85] N. Bannov, V. Mitin and M. A. Strosio, *Phys. Status Solidi B* **183**, 131 (1994).
- [86] N. Bannov, V. Aristov, V. Mitin, and M. A. Strosio, *Phys. Rev. B* **51**, 9930 (1995).
- [87] S. Debal, T. Brandes, and B. Kramer, *Phys. Rev. B* **66**, 041301(R) (2002).
- [88] The parameters for the GaAs quantum dot: $m = 0.067 m_0$, $g^* = -0.44$, $E_a = 6.7$ eV, $\rho = 5.3 \times 10^3$ Kg/m³, $c_t = 3.35 \times 10^3$ m/s, $c_l = 5.7 \times 10^3$ m/s.
- [89] U. Meirav, M. A. Kastner, and S. J. Wind, *Phys. Rev. Lett.* **65**, 771 (1990).
- [90] For a review, see *Single Charge Tunneling*, edited by H. Grabert and M. Devoret (Plenum, New York, 1992).
- [91] R. Schuster, E. Buks, M. Heiblum, D. Mahalu, V. Umansky, Hadas Shtrikman, *Nature (London)* **385**, 417 (1997).
- [92] S. M. Cronenwett, T. H. Oosterkamp, and L. P. Kouwenhoven, *Science* **281**, 540 (1998).
- [93] D. Goldhaber-Gordon, Hadas Shtrikman, D. Mahalu, David Abusch-Magder, U. Meirav, M. A. Kastner, *Nature (London)* **391**, 156 (1998).
- [94] S. Tarucha, D. G. Austing, Y. Tokura, W. G. van der Wiel, and L. P. Kouwenhoven, *Phys. Rev. Lett.* **84**, 2485 (2000).

- [95] A. Y. Smirnov, N. J. M. Horing, and L. G. Mourokh, *Appl. Phys. Lett.* **77**, 2578 (2000).
- [96] L. G. Mourokh, N. J. M. Horing, and A. Y. Smirnov, *Phys. Rev. B* **66**, 085332 (2002).
- [97] G. D. Mahan, *Many Particle Physics*, 3rd ed. (Plenum, New York, 2000).
- [98] T. Brandes and N. Lambert, *Phys. Rev. B* **67**, 125323 (2003).
- [99] Y. Meir and N. S. Wingreen, *Phys. Rev. Lett.* **68**, 2512 (1992).
- [100] A.-P. Jauho, N. S. Wingreen, and Y. Meir, *Phys. Rev. B* **50**, 5528 (1994).
- [101] I. H. Chan, R. M. Westervelt, K. D. Maranowski and A. C. Gossard, *Appl. Phys. Lett.* **80**, 1818 (2002).
- [102] T. Fujisawa, T. Hayashi, Y. Hirayama, H. D. Cheong, and Y. H. Jeong, *Appl. Phys. Lett.* **84**, 2343 (2004).
- [103] C. A. Stafford and N. S. Wingreen, *Phys. Rev. Lett.* **76**, 1916 (1996).
- [104] T. H. Stoof and Yu. V. Nazarov, *Phys. Rev. B* **53**, 1050 (1996).
- [105] Ph. Brune, C. Bruder, and H. Schoeller, *Phys. Rev. B* **56**, 4730 (1997).
- [106] T. Brandes, R. Aguado, and G. Platero, *Phys. Rev. B* **69**, 205326 (2004).
- [107] M. Ciorga, A. S. Sachrajda, P. Hawrylak, C. Gould, P. Zawadzki, S. Jullian, Y. Feng, and Z. Wasilewski, *Phys. Rev. B* **61**, R16315 (2000).

- [108] T. Hayashi, T. Fujisawa, H. D. Cheong, Y. H. Jeong, and Y. Hirayama, *Phys. Rev. Lett.* **91**, 226804 (2003).
- [109] T. Brandes, F. Renzoni, and R. H. Blick, *Phys. Rev. B* **64**, 035319 (2001).
- [110] E. Paspalakis, Z. Kis, E. Voutsinas, and A. F. Terzis, *Phys. Rev. B* **69**, 155316 (2004).
- [111] J. M. Villas-Bôas, A. O. Govorov, and S. E. Ulloa, *Phys. Rev. B* **69**, 125342 (2004).
- [112] M. T. Björk, B. J. Ohlsson, T. Sass, A. I. Persson, C. Thelander, M. H. Magnusson, K. Deppert, L. R. Wallenberg, and L. Samuelson, *Nano Lett.* **2**, 87 (2002).

